5-2019

Covering Shock Wave Induced Interfacial Mixing: Numerical Study and a Control Primer

Erik S. Proaño

CONVERGING SHOCK WAVE INDUCED INTERFACIAL MIXING: NUMERICAL STUDY AND A CONTROL PRIMER

A Thesis

Submitted to the Faculty

of

Embry-Riddle Aeronautical University

by

Erik S. Proaño

In Partial Fulfillment of the

Requirements for the Degree

of

Master of Science in Aerospace Engineering

May 2019

Embry-Riddle Aeronautical University

Daytona Beach, Florida

CONVERGING SHOCK WAVE INDUCED INTERFACIAL MIXING:
NUMERICAL STUDY AND A CONTROL PRIMER

by

Erik S. Proaño

A Thesis prepared under the direction of the candidate's committee chairman, Dr. Bertrand Rollin, Department of Aerospace Engineering, and has been approved by the members of the thesis committee. It was submitted to the School of Graduate Studies and Research and was accepted in partial fulfillment of the requirements for the degree of Master of Science in Aerospace Engineering.

THESIS COMMITTEE

Chairman, Dr. Bertrand Rollin

Member, Dr. Dongeun Seo

Member, Dr. Harihar Khanal

Graduate Program Coordinator, Dr. Magdy Attia — Date: 4-30-2019

Dean of College of Engineering, Dr. Maj Mirmirani — Date: 4/30/2019

Senior Vice President for Academic Affairs and Provost, Dr. Lon Moeller — Date: 4/30/19

ACKNOWLEDGMENTS

My initial gratitude is with my advisor Dr. Rollin for his support and advisory during this endeavor not only in the academic field but also in other matters that made possible the realization of this work. My gratitude goes also to my co-advisor Dr. Seo for his support during the completion of this works. Infinite thankfulness goes to my parents Diego & Janneth whose support and effort made the development of this work worthy. Furthermore, I am thankful with my brother Diego II and my sisters Nicole and Ana for their companion and support even in the long distance. My immense gratitude goes also to Cristina whose support, advises and love rendered this work more tolerable during stressful times. Two more relatives are also artifices of support for this work, my grandfather Fidel and my grandmother Teresa; their instruction during the former years of writing this work has been of immense help during this time.

My debt is also with my friends that supported me during this voyage specially to Andres, Sergio and Carlos for their unconditional support either with advises or with a subjective/constructive opinions during the development of this work. From this pool of great people protrudes one person whose support and companion have signified a unique and remarkable experience. I am deeply thankful to have Silvana at my side all these years supporting me and guiding me during the elaboration of this work. Her companion and tenderness have signified a great push towards the completion of this thesis. I am also grateful with Cristale for her support and advises.

Lastly, an honorable mention to those great groups of people that converted stressful days and nights into a joyful adventure of thinking and music: Black Sabbath, Deep Purple, Pink Floyd & Led Zeppelin. Indirectly they have been artifacts for a better development of this work.

The software used in this work was in part developed by the DOE NNSA-ASC OASCR Flash Center at the University of Chicago. The yt Pyhton API has also been useful for the completion of this work.

In loving Memory of Fidel Cepeda

TABLE OF CONTENTS

LIST OF FIGURES

Figure Page

Figure Page

SYMBOLS

a	Interface amplitude
a_0	Initial interface perturbation amplitude
A	Amplitude of perturbation wave
A_t	Atwood number
A_t^+	Post-shock Atwood number
c	Speed of sound
f	Favre-averaged quantity
h	Mixing layer width
h_0	Initial mixing layer width
h_0^+	Post-shock initial mixing layer width
k	Wave-number
Ma	Mach number
m	mass
n	mode number
P	Pressure
$\mathbf{q}$	State vector
r	Interface radius
r^*	Non-dimensional radius with respect to the interface radius
$\mathbf{R}$	Correlation Tensor
R_0	Initial Interface mean radius
T	Temperature
u	x velocity component
v	y velocity component
w	z velocity component
Y_i	Mass fraction of ith specie
γ	Ratio of specific heats
ϕ	Perturbation phase angle
ρ	Specie density
Θ	Molecular mixing fraction
θ	Perturbation Polar angular location

λ	Perturbation wavelength
ϕ	Perturbation Azimuthal angular location
ϕ	Eigenfunctions or POD modes
η	Amplitude of sinusoidal perturbation
ω	Vorticity
η	Perturbation amplitude

ABBREVIATIONS

DoE	Department of Energy
HI	Hydrodynamic Instabilities
ICF	Inertial Confinement Fusion
ILES	Implicit Large-Eddy Simulations
KHI	Kelvin-Helmholtz Instability
MCF	Magnetic Confinement Fusion
MHD	Magneto-Hydrodynamics
MIF	Magneto-Inertial Fusion
MOR	Model-Order Reduction
POD	Proper Orthogonal Decomposition
RMI	Richtmyer-Meshkov Instability
RTI	Rayleigh-Taylor Instability
TMZ	Turbulent Mixing Zone
VS	Vortex Stretching

NOMENCLATURE

SF_6	Sulfur Hexafluoride
DT	Deterium-Tritium
D_2	Deuterium-Deuterium

ABSTRACT

Proaño, Erik S. MSAE, Embry-Riddle Aeronautical University, May 2019. Converging Shock Wave Induced Interfacial Mixing: Numerical Study and a Control Primer.

This document is aiming toward deepening the understanding of the phenomena of mixing and the effect of the initial conditions in the cylindrical & spherical Richtmyer-Meshkov and Rayleigh-Taylor Instabilities. This work is focused on identifying the most energetic structures of the flow in order to define a reduced-order model intended for modeling the evolution of the mixing layer after reshocking the density interface. Initially, Simulations are implemented for the two-dimensional case of a cylindrical shock wave convergently approaching an initially wave-like perturbed density discontinuity formed by a target of Sulfur Hexafluoride immersed into unshocked air with Atwood number of 0.67. The perturbation is varied by setting different values for the wave amplitude and wave-number; the amplitude and wave-number effects on late-time mixing are studied separately and then such perturbation features are coupled together in the analysis of single- and multi-mode well-defined cylindrical perturbations. The simulation data is then utilized as a mechanism for obtaining a model equation intended to predict the mixing layer evolution using a Proper Orthogonal Decomposition. The ultimate goal of the POD is to model the evolution after reshock which has been the main issue to be tackled since available models fail to predict the extent of the mixing layer after reshocking the interface. Considering three-dimensional effects as in spherical shock-interface interaction gives a better depiction of the small-scale interactions but spherical cases are only quickly addressed. The main effect is the vortex stretching affectation on the vorticity evolution. Furthermore, mixing layers in 3D spherical simulations are found to be wider than its 2D simplified framework. Nonetheless, useful insight is gained by reducing the problen under study to a cylindrical two-dimensional symmetrical system.

1. Introduction

Toward new pathways for cleaner energy generation processes, nuclear fusion (Infeld, 2000) seems to have a tremendous potential. The idea of generating copious amounts of heat by fusion means and transforming it into a utilizable form of energy attracts bright minds to uncover the physics behind such approaches. One promising method for nuclear power generation is to ignite the fusion reaction by a strong shock wave in a process known as Inertial Confinement Fusion (ICF) (Pfalzner, 2006; Atzeni & Meyer-Ter-Vehn, 2009; National Research Council, 2013; Zohuri, 2017) or Magneto-Inertial Fusion (MIF) (Wurden et al., 2016) if the use of an external magnetic field assists the initial compression of the fuel target.

In a detailed point of view, in direct-drive ICF, a driver, typically an array of lasers, heats a spherical or cylindrical shell containing hydrogen-based fuel (target). Due to the heat deposited at the target, its surface ablates and as a reaction of the ablation, a strong imploding shock wave is generated converging towards the center of the fuel target. The interaction of this shock with the density interface between the ablator's shell and the fuel target is at the origin of the induced turbulent mixing zone (TMZ). Such TMZ limits the final compression and temperature of the target and may result in an unsuccessful ignition process for the fuel caused by the imperfect conversion from kinetic energy (implosion) into internal energy. In indirect-drive ICF, the driver irradiates into a high-Z hollow or holhraum chamber which produces energetic X-rays which drive the implosion. In MIF, an externally-generated strong magnetic field is used for initial compression, process known as Magnetic Confinement Fusion

(MCF) (Braams & Stott, 2002), and then the ICF process takes place. Specifically, the nuclei of deuterium and tritium fuse into a heavier element (helium) with the help of the shock wave, releasing in the process incredible amounts of energy which can be transformed. The heat achieved at the hot spot (location where fusion occurs) will heat the surroundings of the fuel transferring enough temperature in order to fully engage the fuel into fusion conditions.

The main advantage of ICF among other fusion approaches is the final energy output expected for such energy-generation methodology. ICF and MCF have been fusion approaches actively seeking to achieve the final goal of ignition. The largest facility currently known for ICF and MCF experimentation is the National Ignition Facility (NIF) belonging to Lawrence Livermore National Laboratory (LLNL). At NIF ignition is the main goal but it is yet to be achieved as currently input energy outweighs the energy output giving poor efficiency.

It is now well accepted that hydrodynamic instabilities present during the interaction of the shock wave with the density interface are the leading cause of the formation of the turbulent mixing layer (Brouillette, 2002), which is not desired in the ICF concept. The Rayleigh-Taylor (Rayleigh, 1882; Taylor, 1950) instability caused by the radial stratification of the fluids and the acceleration of the target is the main driver of the TMZ and it becomes harmful because of its exponential growth. In addition, the Richtmyer-Meshkov instability (Richtmyer, 1960; Meshkov, 1969) affects the density interface initially because of the baroclinic vorticity deposited at the interface due to the misalignment of the pressure and density gradients. Additionally, the TMZ is also driven by the Bell-Plesset effects (Bell, 1951; Plesset, 1954) because of the geometry of the prob-

lem. Initially, because of the shock/interface interaction, the RMI dominates a quasi-linear stage in combination with Bell-Plesset effects. After reshock, i.e. Shock wave auto-focus at the center of the domain and hits back the interface, the exponential growth of the RTI dominates with some secondary instabilities such as the Kelvin-Helmholtz instability.

Well-known models, experimental (Vetter & Sturtevant, 1995; Jacobs & Sheeley, 1996; Poggi, Thorembey, & Rodriguez, 1998; Niederhaus & Jacobs, 2004; Shi, Zhang, Du, & Jia, 2009; Balasubramanian, Orlicz, Prestridge, & Balakumar, 2012; Balasubramanian, Orlicz, & Prestridge, 2013), numerical (Y. Liu, 2008; Schilling & Latini, 2010; Thornber, Drikakis, Youngs, & Williams, 2010; Grinstein, Gowardhan, & Wachtor, 2011; Olson & Greenough, 2014) and theoretical (Vandenboomgaerde, Gauthier, & Mgler, 2002; Dimotakis, 2005; Ukai, Balakrishnan, & Menon, 2011) studies have been widely documented for the case of planar geometry i.e shock tube; however, little work has been performed in cylindrical and spherical geometries. Complications arise in such convergent geometries at late times because of the unavoidable phenomena of reshock. Such physical process triggers highly-nonlinear effects which renders a mathematical description of the phenomena complicated. Models for the interface width and growth rate exist for spherical and cylindrical geometries but they currently do not describe highly-nonlinear features of the phenomena of interest.

It is of interest to develop mechanisms intended reduce the baroclinic vorticity deposited at the density interface by the interaction of the shock wave with the density interface due to the misalignment of the pressure and density gradients. One possible form of gain control of the late-time mixing is to take

advantage of external fields such as electric or magnetic fields. Previous work has demonstrated the capabilities of a magnetic field interacting with shocked stratified fluids in planar cases where the magnetic field mitigates the baroclinic vorticity and inhibits the RMI (Samtaney, 2003).

In taking into account non-linearities of a system, complicated math arises contrary to linearization which goal is to localize a problem to make it fit prescribed needs but it becomes unsuitable for examining variety of different cases governed by the same laws mathematically speaking. Nonetheless, the chaos theory predicts exponential grow of perturbations (Drazin, 1992) rendering non-linearities to be more significant. In such cases, linearization does not describe the physics accordingly. In adding non-linear physics to a problem, mathematical complexity is added significantly and for most problems a general answer seems improbable by means of current knowledge. Numerical techniques then possess the qualities to aid in the approximation towards the right path of seeking for a coherent answer. Direct Numerical Simulation (DNS) seems as the natural way-to-go for analyzing a system when experimentation is not feasible but it is still very expensive computationally even with the current technologies in hardware and software. Large-Eddy Simulation (LES) is styling a new methodology for accurate representations of fluids bulk motion and even being more tractable than DNS. LES is still expensive for some problems and not yet suited for most industrial flows. RANS on the other hand is well consolidated for industrial applications but such approach is not suited for flows in which fluctuations and small scales are of the interest of the researcher or engineer.

Under these discrepancies between simulations methodologies in fluid dynamics, the field of reduced-order modeling has raised as a cheap but perilous mathematical device for modeling a quantity of interest and its evolution by using the modes of the system. The most consolidated of these tools is the Proper-Orthogonal Decomposition (POD) also known as Karthm-Luen Decomposition or Principal Component Analysis (PCA). The POD extracts all the energetic modes of the system from its eigenvalues and projects just the most significant modes onto a new space by using a Galerkin projection. By doing so, an infinite-dimensional system such as the Navier-Stokes Equation can be retrieved as a finite-dimensional system. The concept of infinite-dimensional however is referred to as a system with hundreds of dimensional such as in fluid dynamics. The first known application of POD in the context of analysis of turbulence and fluid dynamics was performed by (Lumley, 1967). The POD renders such a system to for instance 10 dimensions by considering the ten most-dominant eigenmodes namely eigenfunctions. Such modes are extracted from a correlation matrix comprehending state variables. In the case of incompressible flows, the velocity vector is the state vector and no thermodynamic quantities are correlated. Hence, for incompressible flows, the correlation matrix is the matrix computed by the inner product of the velocity vector by its transpose. In contrast, when compressibility is to affect the system considerably as in supersonic flows for instance, thermodynamic quantities are correlated and the correlation matrix comprehends a more wide portray of the system but for obvious reasons it embodies more dimensions.

The present document is organized as follows: the next section gives account of the Hydrodynamic instabilities of interest, namely: Rayleigh-Taylor, Richtmyer-Meshkov instabilities and Bell-Plesset effects; then the initialization of the initially convergent shock wave by considering a Chisnell-type shock is discussed, followed by an explanation and theoretically presentation of the Proper-Orthogonal Decomposition and its variation for compressible flows. Later, the FLASH code utilized for generating the simulations is briefly reviewed and discussed as well as the numerical scheme and flux reconstruction method considered. Afterwards, the results of several simulations involving different initial conditions is presented as well as the POD reconstructed density field for different modes. Finally, concluding remarks are presented.

2. Hydrodynamic Instabilities

Turbulence is triggered from an initially laminar system by flow instabilities caused by several factors such as external influences and geometry. Corrugated density discontinuities (interfaces) between two fluids if excited by an external acceleration whether continuous or impulsive may display different kind of hydrodynamic instabilities.

2.1 Rayleigh-Taylor Instability

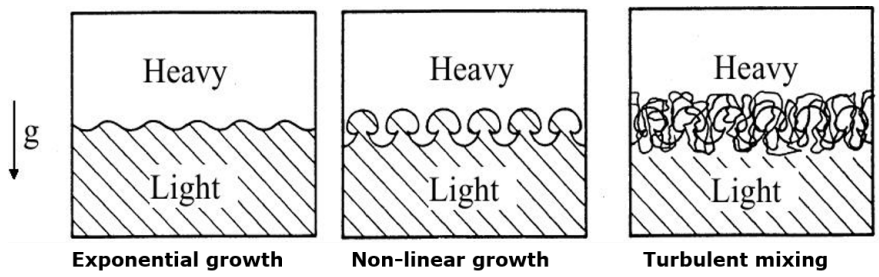

Figure 2.1: Rayleigh-Taylor instability illustration corresponding to a sinusoidal interface perturbation mixing layer evolution in time. Image spurce: M.J. Andrews

The first hydrodynamic instability (HI) of interest concerns the influence of a continuous acceleration acting on a density interface created by two different fluids. If such interface presents spatial perturbation, mixing between species is triggered if the fluids system is stratified in the fashion of the heavier lays fluid on top of the lighter fluid as allustrated in figure 2.1. Lord Rayleigh was the first individual to characteerize such intability by predicting an exponential growth rate of two stratified density-unalike fluids contacted by a rough interface under the action of a continuous acceleration e.g. gravity (Rayleigh, 1882). Taylor confirmed Rayleigh's discover afterwards (Taylor, 1950). The Rayleigh-Taylor Instability (RTI) is observed in several phenomena such as supernovae explosions, mixing enhancement and inertial confinement fusion. According to

Rayleigh' and Taylor's conclusions, a non-dimensional parameter arises in the governing equations. Such parameter is known as the Atwood number and it can be regarded as a non-dimensional density contrast between the two fluids.

$$A_t = \frac{\rho_2 - \rho_1}{\rho_2 + \rho_1} \tag{2.1}$$

In linear geometries encountered typically in stratified fluids, the mixing saturates after all the fluid entrainment process has taken place, meaning that the heavier fluid, initially on top, is at the bottom and the light fluid is at the top. Such configuration correspond to a stable fluid system and no more mixing is expected. The gravitational acceleration is the typical driver for triggering the RTI. In converging geometries nonetheless, a fluid radial movement is encountered by the nature of the geometry itself arriving as a geometric growth known as Bell-Plesset effect(Amendt, 2006) triggering RTI due to the movement of the contact discontinuity. Hence, in convergent geometries there is no need of adding an external acceleration field to observe RTI contrary to linear geometries.

RTI is inherently present in ICF-like implosions due to target's surface unevenness and it is clearly observed at late times after the impulsive accelerative effect of the shock wave has vanished. Nobel-laureate Chandrasekhar published a book concerning several HI of interest with its Magneto-hydrodynamic mathematical treatment (Chandrasekhar, 1981). He presented stability requirements for different cases of stratification, heat transfer and viscosity treatment with and without magnetic effects. Dimonte and Schneider found that RTI vary

strongly depending on the acceleration profile via experimental work and tested several mix models (Dimonte & Schneider, 1996). Livescu and Ristorcelli delivered a work in wich they focus on turbulence development for variable-density fluids (Livescu & Ristorcelli, 2007). They performed numerical simulations for different Atwood numbers and Schmidt numbers and suggested that the mass flux is the most important quantity to extract from lower-dimensional models due to its kinetical character. They also found the evolution of the pressure gradient is non-hydrostatic in the non-Boussinesq regime. Yu and Livescu performed a linear study of RTI accounting compressibility effects for comparison between 3D cylindrical and 2D axysimmetric unperturbed interfaces (Yu & Livescu, 2008). They performed numerical studies for converging and diverging gravitational accelerations and found that the 3D interface grows faster than a 2D interface. Seadawy and Rashidy carried out a non-linear analysis of the RTI for a cylindrical vapour-liquid interface experiencing mass and heat transfer (Seadawy & El-Rashidy, 2016). Their main finding is the stabilization effect consequence of the mass and heat transfer but observed a destabilization due to vapour fraction. Wang et. al published their work comprehending a weakly non-linear model for the RTI assuming incompressibility (Wang, Wu, Ye, Zhang, & He, 2013). Using a third-order solution in cylindrical geometries and a single-mode perturbation, they tested their model and deliver corrections for planar and cylindrical RTI growth.

RTI in the non-linear growth regime for spherical implosions was studied by Hecht et. al. They released 3D simulations of an ICF pellet and performed an analysis on the affectation of the initial conditions to the final stage of the RTI

growth in terms of its Atwood number and shape (Hecht et al., 1995). Chen et. al released their analytical work analyzing the radial movement of the RTI in a cylindrical strata and relate it with its planar counterpart foucsing on ICF conditions. De Groot and Toor developed an early work on RTI growth in cylindrical geometries. They carried out numerical and analytical work for a Z-pinch plasma implosion and found that a shock front originated ahead of the liner is capable of reducing the growth rate of the instability (De Groot, Toor, Golberg, & Liberman, 1997). Furthermore, they suggested that the growth can be further reduced with mass accumulation in comparison with linear in vacuum. Stone and Gardiner performed a MHD non-linear study of the RTI. It is proved numerically in their work that modes aligned with a magnetic field found a suppression of the growth while perpendicular modes remain unaffected (Stone & Gardiner, 2007).

Experimental realization for ICF-like conditions were performed successfully assisted by the NOVA laser(Remington et al., 1992). They found the mixing zone growth is about 60-70% of the growth corresponding the hydrodynamic case while the rest is attributed to an ablative stabilization. In addition, they predicted the growth in the non-linear regime by a third-order method. Hsing et. al measured growth of a cylindrical target's ablation front due to RTI for different target's material and x-ray backlighting (Hsing et al., 1997). Using the direct-drive approach for ICF, Tubbs et. al performed experiments in a cylindrical framework in order to demonstrate the advatanges of direct-drive ICF compared to indirect-drive ICF (Tubbs et al., 1999). They found a high disagreement between experimental and numerical results for the RT growth for

the shell's exterior edge. Sinars et. al performed a controlled experiment for RTI in MHD for Z-pinch plasmas. Based on sinusoidal spatial perturbations they found agreement with numerical work up to 50 μm wavelengths (Sinars et al., 2010). They further extended their work with more radiography images and a better target characterization for more accurate comparison with numerical and analytical work (Sinars et al., 2011).

2.2 Richtmyer-Meshkov Instability

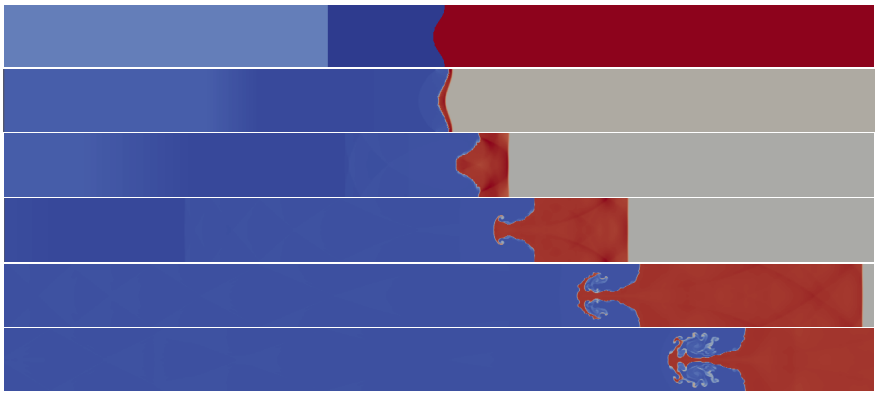

Figure 2.2: Richtmyer-Meshkov instability in a shock tube corresponding to a sinusoidal interface perturbation mixing layer evolution in time. The simulation was performed by the Flash code. The top frame shows the Shocked and Unshocked regions, light blue and blue regions, separated by the shock wave and the SF_6 interface in red

A limiting case of the RTI arises when the acceleration acting on the density interface is of impulsive nature i.e. a shock wave. When a shock wave hits a density discontinuity, a mixing process is initiated as a natural mechanical response to the passage of the acceleration peak. Mushroom-like structures are initially observed as a result of baroclinic vorticity deposition at the interface (see figure 2.2). The first researcher interested in this phenomena was Richtmyer whose main contribution was the prediction of an initial linear growth of the mixing layer (Richtmyer, 1960). Afterwards, experimental evidence of this behavior was delivered by the work of Meshkov (Meshkov, 1969). Hence, this type

of HI is well known as the Richtmyer-Meshkov Instability (RMI) and it is the first mechanism of instability studied in the present work. More formally, the RMI is caused by a misalignment of the pressure and density gradients induced by the interaction of the shock wave and the density interface. In contrast to RTI, RMI occurs regardless of the stratification of the fluids system.

$$\frac{d\omega}{dt} = \frac{1}{\rho}\left(\nabla p \times \nabla \rho\right) + \omega \cdot \nabla u - \omega\left(\nabla \cdot u\right) \tag{2.2}$$

Several models has been proposed in order to predict the growth of the mixing layer caused by the passage of a shock wave. A successful individual in portraying the growth rate mathematically due to RMI is Mikaelian (Mikaelian, 1990, 2005). His models agrees with experimental evidence as well as numerical works and serve as a baseline for validating computational efforts.

As previously stated, the first experimental measures were carried out by Meshkov; nevertheless, more early experiments were also performed, with the celebrated experiment of Vetter and Sturtevant being the setpoint for most numerical works in planar geometries (Vetter & Sturtevant, 1995). Poggi (Poggi et al., 1998) also performed a similar experiment.

Plenty of work has been performed in the case of RMI for planar cases but not much attention has been directed to the RMI in converging geometries. One of the first work regarding RMI in cylindrical geometries was performed more than 20 years ago (Q. Zhang & Graham, 1998). They studied the development of the 2-dimensional interface after shock and reshock for different Atwood numbers. Spherical axisymmetric RMI studies were also perfomed (Dutta, Glimm, Grove, Sharp, & Zhang, 2004). Dutta et. al were interested in strong incident

shocks $M \geq 10$ and using the front tracking method they found scaling invariant as a function of shock strength; their main finding was the realization that high wavenumber perturbation are justifiable studied as planar geometries if the effects of low wavenumbers are negligible (Cheng, Glimm, & Sharp, 2002). After that, Youngs and Williams presented an account on mixing in this type of flows with three-dimensionsional simulations (Youngs & Williams, 2008). Even though they accurately quantified a kinetic energy dissipation for low Mach numbers, the results were only useful for validating models. Joggerst et. al released a code comparison for cylindrical and spherical implosions (Joggerst et al., 2014). This group found several differences in cylindrical and spherical RMI depending on the code considered and the grid. They consolidated the FLASH code for this kind of flows as a reliable code and found that using a Cartesian grid is better than a curvilinear grid for the initial perturbation.

One of the main works for RMI in cylindrical and spherical geometries were performed by Lombardini and Pullin. First, they released a work with a simple model able to describe the evolution of the mixing zone in the linear regime (Lombardini & Pullin, 2009). After that, they released a three-dimensional wide analysis on RMI in cylindrical geometries (Lombardini & Pullin, 2009). It only covered the linear regime and no reshock process was studied. Their work was extended when they released a paper with a complete description of the RMI in spherical geometries, considering also reshock, for a small-amplitude perturbation with a high spectrum of wavenumbers generated by spherical harmonics (Lombardini, I. Pullin, & Meiron, 2014a). They also presented a statistical ac-

count for accurately quantify the mixing happening at the density interface at late times (Lombardini, I. Pullin, & Meiron, 2014b).

The interest in mitigating the RMI drove Mostert et. al to focus on studying such HI in ocnvregent geometries for the case of Magneto-Hydrodynamics (MHD) (Mostert, Wheatley, Samtaney, & Pullin, 2015). They studied axisymmetric targets with differently-aligned magnetic fields acting on the flow and found that RM and RT instabilities are inhibited by the magnetic fields. Bakhsh et. performed linear simulations of cylindrical RMI and found the mechanism of inhibition of the growth of the interface is the transport of vorticity away from the interface by Alfven fronts (Bakhsh, Gao, Samtaney, & Wheatley, 2016). Sano et. al on the other hand found an amplification of the magnetic field associated with RMI (Sano, Nishihara, Matsuoka, & Inoue, 2012). Their work presented 2D simulations of RMI with magnetic fields but has astrophysical applications rather than focusing in ICF.

Aglitsky et. al released a work in hydrodynamic instabilities focusing mainly in ICF-like conditions (Aglitskiy et al., 2010). Their work present a more physical account of the whole phenome as they analized the ablative RMI and the target shape and material itself. Marocchino et. al also delivered a paper on the ablative RMI at the ablation front for ICF targets (Marocchino, Atzeni, & Schiavi, 2010). They analized small amplitudes in the linear regime with respect to the laser intensity and found that ablative RMI originates the ablative RTI and modeled electron heat transport.

Experimental studies of RMI in convergent geometries are more scarce. The first known experimental study of RMI in cylindrical geometries was performed

by Hosseini and Takayama one year later (Hosseini & Takayama, 2005). They used a vertical annular diaphragmless shock tube to convert a planar shock wave into a cylindrically-convergent shock wave and captured the interface and shock history with Holographic interferometric flow visualization for various gasses. Several years later, Luo et. al performed an experimental study of RMI using a semi-annular shock tube similarly as Hosseini and Takayama but they were able to shape a bubble of SF_6 into a well-characterized wave perturbation by a special interface formation device (Luo, Ding, Wang, Zhai, & Si, 2015). They presented experimental schlieren images of the whole process even for reshock for a half-bubble of mostly SF_6 but no interface evolution or mixing were quantified. Their initial conditions were $a = 2mm$, $k = 6$ and $R_0 = 25mm$. Using a similar experimental equipment, Lei et. al showed experimental realizations of a complete bubble of SF_6 for different wavenumbers and amplitudes (Lei, Juchun, Si, Zhai, & Luo, 2017). They showed the mixing layer development in time for the different initial conditions analyzed and experimentally observed a stabilization effect cuased by the reshock. Similar studies were presented by this group (Ding, Si, Wang, & Luo, 2017; F. Zhang, Zhai, Si, & Luo, 2017). A variation of these experiments was released in which the RMI is induced at a cylindrical no-perturbed interface for an incident difracted shock wave (Liang, Ding, Zhai, Si, & Luo, 2017). They generated a diffracted shock wave by several cylinders accommodated before the interface in an azimuthal fashion. Their main finding was that a shock perturbation is not equivalent to an interface perturbation; hence, one cannot perturbed the shock to study interface perturbation. For a complete survey on both HI, namely RT and RM instabilities, the reader is re-

ferred to Zhou's work where he presents a variety of available analytical, numerical and experimental works on RT and RM instabilities for planar and convergent cases (Zhou, 2017a, 2017b).

2.3 Bell-Plesset Effects

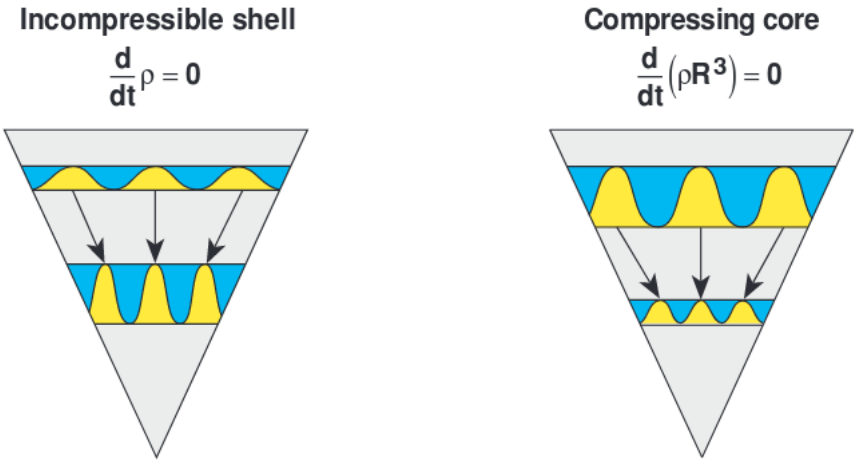

Figure 2.3: Illustration of the Bell-Plesset Effects in a spherical shell due to the radial movement of the interface. Image taken from Epstein, 2004.

In a cylindrical framework, the radial movement of a fluidic system is inherently caused by Bell-Plesset effects as depicted in figure 2.3. Bell initially surveyed the influence of spatial small perturbations in cylindrical and spherical surfaces and their effects on radial movement in fluid dynamics using potential flow theory (Bell, 1951). He obtained different ordinary differential equations (ODEs) depending on the dependency of the ripples and the independent variables i.e. (r, θ, z) in cylindrical and (r, θ, ϕ) in spherical coordinate systems. Bell's ODEs served as the primal born of several models that came up later for the prediction of the development of the mixing zone. Plesset tackled a spherical interface with a density jump(Plesset, 1954). The main difference between both works is in the treatment of the perturbation. Bell considered a mass amplitude for the perturbation equation of a free surface while Plesset used directly

a spatial amplitude (Epstein, 2004). Amendt et. al proposed a model accounting for compressibility effects in Bell-Plesset type flows for ignition of double-shell targets and suggested the possibility for igniting such targets (Amendt, Colvin, Ramshaw, Robey, & Landen, 2003). Analytical work tackling the RT and BP growth was released by Amendt for the case of contiguous density gradients in spherical interfaces (Amendt, 2006). A more complete analytical work of the BP growth in flows experiencing RTI due to convergent or divergent effects for ideal-incompressible radially-stratified fluids with finite-thickness interfaces was presented by Velikovich and Schmit (Velikovich & Schmit, 2015).

2.4 Interface Growth Models

The growth of a corrugated density interface formed by two different fluids present a challenging depiction of fluid dynamics with several difficulties in its characterization. Several attempts for predicting the mixing layer development have been made. The first successful model is the one derived by Richtmyer which prediction gave the linear characterization of the mixing layer at early times just after the shock-interface interaction. Mixing layer models for late times after reshock in the planar case exist and are currently implemented in numerical studies of shock tubes or as complementary computations to increase the validity of experiments; however, to the understanding of the author of this work, there is no model valid for predicting the development of the mixing layer induced by a convergent shock wave after reshocking the previously-perturbed density interface.

The difficulty in advancing a model for the non-linear stages of the RMI dwells in the non-deterministic nature of the density interface after the insta-

bility takes place. In other words, once the convergent shock has triggered the RMI, after the shock reaches the convergence center and reflects itself becoming an divergent shock wave, the interface has lost most of its deterministic properties due to the stochastic phenomena taking place after the linear prediction. Hence, the newly perturbed interface displays multimode features with a high interaction between modes. Reshocking the interface enhances the mixing, resulting in a more chaotic mode interaction. Thus, present models for the growth of the mixing layer in convergent geometries are able to describe the phenomena just before the reshock phase. It is one of the objectives of the present thesis to set the path for a model describing such late-time phase prediction of the development of the mixing layer based on reduced-order techniques.

$$\frac{d^2\eta}{dt^2} - kgA\eta\left(t\right) = 0 \tag{2.3}$$

$$\frac{dh}{dt} - \mu k \Delta u h_0^+ A_t^+ = 0 \tag{2.4}$$

The first prediction of the mixing layer evolution in time was developed by Richtmyer himself (Richtmyer, 1960). He derived a growth equation which predicts an initially linear growth rate based on the post-shock Atwood number A_t^+. Such equation is only valid for predicting the growth of the mixing layer at early times before the well-known mushroom-like structure has developed. From the equation 2.3 derived by Taylor (Taylor, 1950), Richtmyer obtained the growth impulsive linear model presented as equation 2.4. Equation 2.4 is valid when the reflected and transmitted waves are far from the perturbation compared with its amplitude, i.e. incompressibility holds at the density interface vicinity. Based on potential flow theory, the equations derived by Bell for cylindrical and spherical

shells movement (Bell, 1951) for small-amplitude ripples has been widely used for extracting interface growth models for early times.

$$\frac{d^2\eta}{dt^2} + 2\frac{\dot{R}}{R}\frac{d\eta}{dt} - (nA - 1)\frac{\ddot{R}}{R}\eta = 0 \tag{2.5}$$

$$\frac{d^2\eta}{dt^2} + 3\frac{\dot{R}}{R}\frac{d\eta}{dt} - nA(n)\frac{\ddot{R}}{R}\eta = 0 \tag{2.6}$$

Bell's equation presented in equation 2.5 for cylindrical motion and equation 2.6 for spherical motion are the starting base for the models developed by Mikaelian. The simple ODEs described by Bell are valid only for irrotational motion and thus they are not expected to perform well for non-linear stages of the evolution of the mixing layer where the HI are highly developed. Mikaelian first developed an integral model for spherically-stratified shells and extended the model for n shells (Mikaelian, 1990). 15 years later, Mikaelian performed a similar analysis for cylindrical shells arising to a similar conclusion and model with the only change on the exponent of R in the mixing layer width model equation (Mikaelian, 2005).

$$h(t) = h(0) + R_0^3\frac{dh_0}{dt}\int_0^t \frac{1}{R^3}dt + cA\int_0^t\left(\frac{1}{R^3}\int_0^t R^3\ddot{R}dt'\right)dt \tag{2.7}$$

$$h(t) = h(0) + R_0^2\frac{dh_0}{dt}\int_0^t \frac{1}{R^2}dt + cA\int_0^t\left(\frac{1}{R^2}\int_0^t R^2\ddot{R}dt'\right)dt \tag{2.8}$$

Both models for spherical and cylindrical shells are described by equations 2.7 and 2.8 respectively. Note the only difference in the exponent of R being 3 for spherical shells and 2 for cylindrical similarly as the Guderley indexes for spherical and cylindrical shocks. The models work well when $a_0/\lambda_0 \leq 0.1$ and some corrections are implemented when the amplitude-wavelength ratio is higher

(Rikanati, Oron, Sadot, & Shvarts, 2003; Jourdan & Houas, 2005; Juchun et al., 2017); nonetheless, the models are not able to describe the interface evolution after reshock and hence the need of a model to accurately predict the interface width and growth rate after reshock for the non-linear stage.

3. Proper Orthogonal Decomposition

The highly-nonlinear stochastic nature of turbulent fluid motion presents challenging computations even for state-of-the-art equipment when computing small-scale eddied interaction. If one is interested in obtaining a dynamical model of a fluid system as a plant for control purposes, then the NS equations might be used as the dynamics for fully describing the phenomena of interest; nonetheless, in controlling fluid flow a rapid response is desired and using the NS equations for estimating or predicting fluid behavior as a dynamical model becomes really expensive computationally and time-wise. From a control point of view, such expensiveness is not desired specially for real-time estimations. Reduced-order modeling (ROM) offers a simpified solution for estimating the behavior of a desired fluid system, minimizing the computing requirements at the cost of loss of accuracy. The Proper orthogonal decomposition (POD) is a ROM method that extracts the modal character of a flow from numerical or experimental realizations and describe the system from an orthogonal projection of its governing equations a.k.a. Galerkin projection. By taking advantage of the POD, the user desires to reduce the estimation time of the system for implementation. Ultimately, the POD shall deliver an ODE as a function of the POD modes which might accurately portray the whole fluid bulk dynamics.

The correlation matrix is just the first step towards obtaining a ROM using POD. The main interest of such matrix is to extract its eigenvectors and eigenvalues in order to project them into a new sub-space. There is no a rule-of-thumb of the number of modes to be considered as it is problem-dependent but one needs to ensure that the chosen modes are able to describe the sys-

tem almost in its totality. Such decision is left as the researcher discretion. As a baseline, plotting the eigenvalues against total energy might reveal the most energetic eigenvalues to which relate its respective eigenfunction.

Considering a state variable as a function of the velocity field

$$\mathbf{q} = f(\mathbf{u})$$

$$\mathbf{q} = \sum a_n(t)\,\boldsymbol{\phi}(\mathbf{x}) \tag{3.1}$$

The correlation tensor being computed as

$$\mathbf{R}(\mathbf{x}, \mathbf{x}') = \langle \mathbf{q}, \mathbf{q}' \rangle \tag{3.2}$$

The operation above $\langle \cdot, \cdot \rangle$ is defines as the inner product of the space in which we are transforming the primitive variable, e.g. a dot product in conventional space dimensions.

3.1 The Method of Snapshots

The POD is a consolidated tool available for a long time but it has several variants. It is important to remark the differences between the POD described by Lumley and the POD approach developed by Sirovich known as the method of snapshots (Sirovich, 1987a, 1987b). In contrast to the direct method in which the eigenvalue problem is solved directly, the method proposed by Sirovich is applied at each simulation snapshot; In the direct method, the solution of the eigenvalue problem comprehends a matrix of order $M \times M$, with M being the order of the state vector or the data size. On the other hand, the method of snapshots solves the optimization problem with a reduced matrix of order $M \times N$ where N is the number of snapshots and $N \ll M$. Consider a CFD simula-

tion with 100 velocity field outputs for a structured coarse Cartesian grid of 1024×1024. If the direct method is implemented to extract the POD modes then the order of the Correlation tensor if the state vector comprehends only the x- and y-velocity components u and v respectively, shall be $M = nVars \times nPoints_x \times nPoint_y$ which for the aforementioned instance becomes $M = 2 \times 1024 \times 1024 = 2'097,152$. Thus, the correlation tensor R is a second order tensor of dimensions $2,097,162 \times 2,097,162$.

Now consider the same parameters but using the method of snapshots for a 100 snapshots, the order of the correlation tensor R becomes $2,097,162 \times 100$. Observe the high contrast between both methods. The advantage of utilizing the method of snapshots is reflected in more efficient computational algorithms due to the reduced memory necessary for performing the computations based on the correlation tensor. Therefore, the method of snapshots is implemented in this thesis for the extraction of the POD modes. Finally, a Galerkin projection is required for fully modeling the development of the mixing layer based on the POD modes and time coefficients obtained from previously-generated data.

3.2 POD for Compressible Flows

As stated previously, more state variables are necessary for performing a POD to compressible flows; specifically, thermodynamic quantities are to be added to the state vector. When performing the inner product for computing the correlation tensor it is obtained for a state vector of the fluctuating quantities $q = [u', v', w', \rho', P']$

$$\langle \mathbf{q}_1, \mathbf{q}_2 \rangle = \int_\Omega (u'_1 u'_2 + v'_1 v'_2 + w'_1 w'_2 + \rho'_1 \rho'_2 + P'_1 P'_2)\, d\mathbf{x} \tag{3.3}$$

Note from equation 3.3 that it does not makes physical sense to add up velocities squared with densities and pressures squared as a consistency in units is completely lost. Hence, the proposed state vector is not well-suited as it does not make physical sense. Rowley et. Al proposed a state vector based on the speed of sound in order to deliver an energy-based physical meaning to the correlation tensor (Rowley, Colonius, & Murray, 2004). The state vector they used was $q = [u', v', w', c']$ based on the definition of total enthalpy; That vector gives

$$\langle \mathbf{q}_1, \mathbf{q}_2 \rangle = \int_\Omega \left(u_1' u_2' + v_1' v_2' + w_1' w_2' + \frac{2\alpha}{\gamma - 1} c_1' c_2' \right) d\mathbf{x} \tag{3.4}$$

Note from equation 3.4 that now the units have coherence and the inner product has a physical meaning in terms of energy. In addition, they demonstrated that the inner product from equation 3.4 preserves the stability of the equilibrium point at the origin after the Galerkin projection. Using this state vector and performing a Galerkin projection of the fluctuating quantities, Rowley et. Al were able to obtain a reduced model of the NS equations for compressible flows. The constraint of this inner product is that it is only valid for isentropic flows since it is based on the isentropic NS equations.

A different approach for eliminating the physical non sense due to the units is to non-dimensionalize the variables but then the physical sense might not be explicit. In that sense, the fluctuating quantities can be non-dimensionalized by dividing them to its Root mean square (RMS) value.

Consider the state vector of the fluctuations as $q = [\rho', u', v', w', T']$, then the inner product

$$\langle \mathbf{q}_1, \mathbf{q}_2 \rangle = \int_\Omega \left[\frac{\alpha}{2} \left(\frac{\rho_1' \rho_2'}{\overline{\rho'^2}} + \frac{u_1' u_2' + v_1' v_2' + w_1' w_2'}{\overline{\mathbf{v}'^2}} \right) + (1 - \alpha) \frac{T_1' T_2'}{\overline{T'^2}} \right] d\mathbf{x} \tag{3.5}$$

Considering the inner product presented above in equation 3.5 proposed by Yang and Fu (Yang & Fu, 2008) is suited for the type of flow analyzed in this work. This inner product consider two thermodynamic variables instead of the assumption of isentropic flow as in the ininer product proposed by Rowley et. Al (Rowley et al., 2004). These two thermodynamic variables are able to describe the system with the dynamic variables as well. From temperature and density, one can get reconstruct the pressure field and the speed of sound fields. Even though this inner product is not very sensitive, it is able to increase the scope of the POD in terms of energy capturing. For a complete description of each inner product discussed the reader is referred to the book by Gatski and Bonnet in which they present a comparison of different inner products proposed (Gatski & Bonnet, 2013) as an adaptation of the compilation of the comparisons made by Yang and Fu to show that their inner product is well suited for flows with compressibility effects (Yang & Fu, 2008).

Another important feature to consider in POD for compressible flows is the averaging process. The POD is applied to a state vector based on fluctuating quantities and the averaging process must be properly performed for variable-density flows. To do so, the Favre averaging procedure or density-weighted averages (Favre, 1965) in order to consider variable-density flows. In such framework, the flow is decomposed similarly as a Reynolds decomposition in mean flow and fluctuating flow as

$$f(\mathbf{x},t) = \tilde{f}(\mathbf{x},t) + f''(\mathbf{x},t) \tag{3.6}$$

In equation 3.6, the term $\cdot''$ are the fluctuations and $\tilde{\cdot}$ are the Favre averages computed as

$$f = \frac{\overline{\rho f}}{\overline{\rho}} \tag{3.7}$$

where ρ is the density field of the flow and f is the quantity to be averaged.

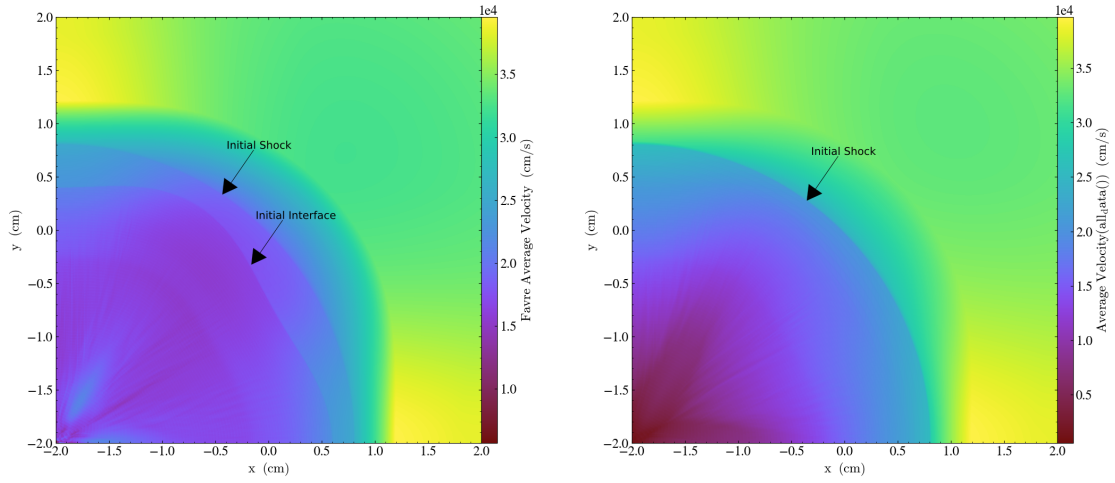

(a) (b)

Figure 3.1: Contrast between the averaging procedures (a) Favre average flow and (b) Reynolds averaging procedure

Notice from figure 3.1 that the Favre averaging procedure captures more features that are ignored by the conventional averaging method. The Favre averaging is able to capture the density interface as well as the initial shock diaphragm i.e. the region separating the shocked fluid with the unshocked fluid where the shock wave is initially triggered. In contrast, the regular averaging does not capture the initial density into the average flow and only captures the fluctuations at the turbulent mixing zone.

4. Numerical Treatment

In the present section, the numerical approach considered for solving the Riemann problem is discussed as well as some features implemented at the initialization stage of the initial conditions.

4.1 The FLASH code

The Flash code is a well-established and validated code written in FORTRAN 90 and developed by the Flash Center at the University of Chicago (Fryxell et al., 2000). The FLASH code is intended for Astrophysical flows and Magneto-HydroDynamics (MHD). This code possesses several discretization methodologies for different types of flows and governing physics. In the present treatise, a 5th order Weighted Non-Oscillatory Scheme (WENO) (X.-D. Liu, Osher, & Chan, 1994) is utilized from its implementation in the FLASH code. The 5th order WENO scheme is considered for the present work as it encompasses a high-order technique for smooth flows and the capability of a shock capturing schemes.

The time step is CFL-driven and the user is not allowed to set a constant time step but the controllability of output files is achieved by setting checkpoint files and maximum simulation time. Due to the use of nonlinear schemes, a slope limiter is also provided by the user in the input file as well as its limited slope which drives the transition from low-order to high-order methods for discontinuities and smooth parts of the flows repectively (Pletcher, Tannehill, & Anderson, 2012). The slope limiter considered is the vanLeer (van Leer, 1979) for the prevention of oscillatory solutions. Such method was also specially de-

signed for ICF-like numerical computations. Furthermore, the use of artificial viscosity (Godunov, 1959) is considered for obtaining more stable solutions.

The FLASH code implements a shock detection algorithm which switches the shock handling depending on the shock strength. In this study, the shock detection algorithm is enabled because as the shock wave converges towards the reflection center, the imploding shock wave becomes stronger and it is a strong shock at the vicinity of the convergence center (Guderley, 1942). For such reason, the FLASH-native shock detection is enabled which delivers a new output variable called 'shok' which is a useful field for tracking of strong shocks as it shows only the actual shock location. The shock detection algorithm implemented within the framework of FLASH captures a shock wave based on a comparison of the pressure jump in the direction of compression with a shock parameter defined as 1/3. For a detailed description of shock detection in FLASH the reader is refered to its manual ("Flash User's Guide version 4.5", 2018). The FLASH is capable of solving multispecies flows and hence it solves the Euler equations for multiple gasses presented in conservative form as

$$\frac{\partial U}{\partial t} + \frac{\partial F\left(U\right)}{\partial x} + \frac{\partial G\left(U\right)}{\partial y} + \frac{\partial H\left(U\right)}{\partial z} = 0 \tag{4.1}$$

with,

$$F = \begin{bmatrix} \rho u_x \\ \rho u_x^2 + p \\ \rho u_x u_y \\ \rho u_x u_z \\ u_x (e + p) \\ \rho X_l u_x \end{bmatrix}, \quad G = \begin{bmatrix} \rho u_y \\ \rho u_x u_y \\ \rho u_y^2 + p \\ \rho u_y u_z \\ u_y (e + p) \\ \rho X_l u_y \end{bmatrix}, \quad H = \begin{bmatrix} \rho u_z \\ \rho u_x u_z \\ \rho u_y u_z \\ \rho u_z^2 + p \\ u_z (e + p) \\ \rho X_l u_z \end{bmatrix}$$

In the present work, equation 4.1 is solved as a multi-gamma fluid system is invoked by the initial conditions. The three regions of the flow, namely, unshocked region, shocked region and target region, are divided as follows in terms of their specific heat ratios: unshocked and shocked regions contain the same specific heat ratios $\gamma = 1.4$ for air and the target region contain the second species ratio $\gamma = 1.09$ for the case of a pocket of SF_6.

The Riemann problem is then solved numerically by the code in a multi-core framework by using the Harten-Lax-van Leer-contact wave (HLLC) approximate solver developed by Toro et. al(Toro, Spruce, & Speares, 1994). All the combination of the aforementioned features of the Flash code are utilized to minimize the numerical noise that might be present due to the type of simulation as well as for stable solutions of the hyperbolic Riemann problem.

The Flash code produces hierarchical data files version 5 (HDF5) output at each desired checkpoint step. The HDF5 output structure contains the variables defined in the implementation of the code as well as user-enabled variables plus information on the grid. HDF5 files can be read in several ways but the author uses Python for reading all the data structures and generate the desired out-

puts. As a quick-visualization tool for instantly monitoring the output files, VisIt 2.10 was considered as it possess a plugin for reading Flash-output files in a quick manner.

The meshing order follows the path of a Morton or Z-order curve(Morton, 1966) in order to deliver one-dimensional data to the output file. The AMR in Flash localizes small cells in zones of strong gradients such as in discontinuities e.g. shock waves. This local cell size reduction is based on criteria choose by the user via input file. The criteria are the variables that Flash natively computes such as density, pressure, temperatures or velocity components. In the present work, an AMR mesh with 4 levels of refinement is generated via Paramesh 4 by the Flash code.

4.2 Chisnell-type Shock Wave

The conditions of the flow after the passage of a shock wave, whether planar or oblique, is a well-characterize phenomena; the average flow state behind of a shock wave (state 2) might be obtained by its conditions ahead of the wave (state 1) (Whitham, 1974). The conditions for a steady planar shock wave are

$$\rho_2 u_2 = \rho_1 u_1 \tag{4.2}$$

$$p_2 + \rho_2 u_2^2 = p_1 + \rho_1 u_1^2 \tag{4.3}$$

$$h_2 + \frac{1}{2}u_2^2 = h_1 + \frac{1}{2}u_1^2 \tag{4.4}$$

It is beyond the scope of this disquisition to discuss on the aspects of such waves; rather, it is of interest to establish the foundations on supersonic flows with the presence of cylindrical or spherical shock waves. For a detailed and

formal description of shock waves the reader is refered to more specific literature regarding its mathematical formalization (Shapiro, 1953, 1954; Courant & Friedrichs, 1999) and physical description (Anderson, 1982; Zel'dovich & Raizer, 2002; Ockendon & Ockendon, 2016). Similarities exist among the aforementioned shock waves in respect to their physical conduct such as the pressure and entropy change across a shock wave to mention a general overview. Nonetheless, well-established shock wave relations do not hold satisfactory within the cylindrical and spherical framework. The most intriguing effect probably being the acceleration of a curvilinear shock wave as it approaches to its convergence center. In such fashion, the most useful characterization for the flow properties in both states, shocked and unshocked, should be based on the radial distance of the shock wave from its convergence center.

Curiosity on the discussed matter awoke bright minds that first attempted to characterize the conditions of the flow under the influence of a cylindrical shock wave. The first researcher to deliver a coherent approximation to this issue was Guderley (Guderley, 1942). His work is based on the Rankine-Hugoniot conditions for the limit case of a strong wave. As such, Guderley's approach is only valid for a convergent shock wave at the vicinity of the convergence center as an imploding shock wave augments its strength as it approaches to the convergence center when the strength is singular.

Chisnell presented a first approximation for cylindrical and spherical shock waves by describing the shock motion through a channel and relating the area change with the shock strength (Chisnell, 1957). Chisnell primary works was based on the description of Chester (Chester, 1954). Whitham released his the-

ory of Geometrical Shock Dynamics (GSD) for shock wave evolution via boundary interactions (Whitham, 1958; Whitham, 1974). Whitham described the propagation of shock waves along non-uniform ducts by the shock relations and the following rule: "The rule is to apply the differential relation which must be satisfied by the flow quantities along a characteristic to the flow quantities just behind the shock wave" (Whitham, 1958). Chisnell's biggest influence in this field is highlighted by his pioneering published in 1998 (Chisnell, 1998). There, Chisnell found an approximate solution based on analysis on the singular points of the differential equation governing the shock motion in the present geometries. He described the shock relations as a function of the radius at each radial location for several specific heat ratios γ. The gain obtained by implementing such approximation as initial condition is the mitigation of spurious oscillations near the shock front. A comprehensive review and well-elaborated explanation on the Guderley problem and validation of such theory can be found in the work by Ramsey, Kamm and Bolstad (Ramsey, Kamm, & Bolstad, 2012).

To extract the ratios of the flow and thermodynamic properties ahead and behind a converging shock wave, Chisnell (Chisnell, 1998) first replaced the pressure by a speed of sound description as

$$c^2 = \frac{\gamma p}{\rho}$$

then non-dimensional variables are set as

$$G = \tfrac{\rho}{\rho_0}; \quad V = \tfrac{ut}{r}; \quad Z = \left(\tfrac{ct}{r}\right)^2 \tag{4.5}$$

and the position of the convergent shock wave, i.e. the shock radius, is described as

$$\xi = \frac{r}{R}$$

Based on the Rankine-Hugoniot conditions for a strong shock, the boundary conditions at the shock are computed as

$$\xi = 1; \quad G_s = \tfrac{\gamma+1}{\gamma-1}; \quad V_s = \tfrac{2\alpha}{\gamma+1}; \quad Z_s = \tfrac{2\gamma(\gamma-1)\alpha^2}{(\gamma+1)^2} \tag{4.6}$$

Chisnell performed a detailed analysis on the singularities of the following equation

$$\frac{1}{Z}\frac{dZ}{dV} = \frac{2\Delta\left(\alpha - V + \frac{1-\alpha}{\gamma}\right) + (\gamma-1)(\alpha-V)Q}{\Delta\left(sV - \frac{2(1-\alpha)}{\gamma}\right)(\alpha-V) + (\alpha-V)^2 Q} \tag{4.7}$$

by computing a trial function Z_T based on the singular points of equation 4.7, the similarity exponent α is approximated by different types of γ.

$$\frac{\rho}{\rho_s} = \left(\frac{\alpha - V}{\alpha - V_s}\right)^{\eta} \left(\frac{V+q}{V_s+q}\right)^{D} \tag{4.8}$$

$$\frac{u}{u_s} = \left(\frac{V}{V_s}\right)^{1-\alpha} \left(\frac{V+q}{V_s+q}\right)^{F} \tag{4.9}$$

$$\frac{p}{p_s} = \left(\frac{V}{V_s}\right)^{2(1-\alpha)} \left(\frac{V+q}{V_s+q}\right)^{B+D+2F} \tag{4.10}$$

$$\xi = \left(\frac{V_s}{V}\right)^{\alpha} \left(\frac{V+q}{V_s+q}\right)^{F} \tag{4.11}$$

$$E = \eta = \tfrac{\frac{2(1-\alpha)}{\gamma}}{s\alpha - \frac{2(1-\alpha)}{\gamma}}; \quad D = \tfrac{s-1}{1-s\lambda} - \eta; \quad F = \alpha - \tfrac{1-\lambda}{1-s\lambda} \tag{4.12}$$

$$V = \frac{2\alpha(1-\alpha)}{(s-1)\gamma V_0} \tag{4.13}$$

The ratios shown in equations 4.8 - 4.11 are utilized for computing the flow properties behind the wave. In other words, the flow downstream of the convergent shock wave is initialized by using the above conditions.

Figure 4.1 shows a validation of the author's implementation in the FLASH code of the Chisnell approximation for computing the flow behind an imploding cylindrical shock wave in air ($\gamma = 1.4$). A brief look at it depicts a reasonable agreement between the computed ratios and the data obtained from Chisnell's work (Chisnell, 1998). The data is displayed as in the original paper. The radial ratio of $\xi^{-1} = 1$ corresponds to the position of the shock wave and $\xi^{-1} < 1$ belongs to the shocked air range, i.e. as $\xi^{-1} \rightarrow 0$ the actual radial position if far from the imploding shock position. Figure 4.1 serves as a validation of the flow initialization behind the shock wave; thus, the confidence of such implementation in the code is high and it is used for all the upcoming simulations as initial conditions in the shocked flow. The advantage of using a Chisnell-type shock wave resides in the reduction of spurious waves appearing in regular discontinuities for conservation laws and leaves the shock thickness as the only intrinsic scale (Lombardini et al., 2014a).

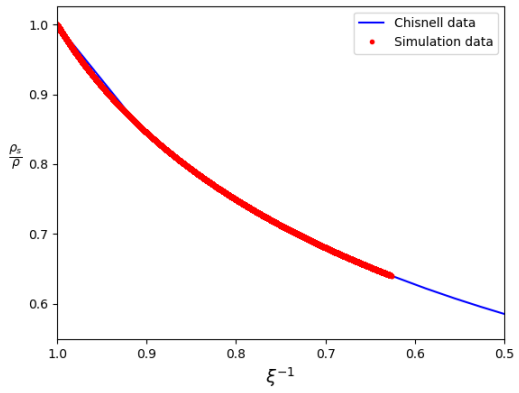

(a)

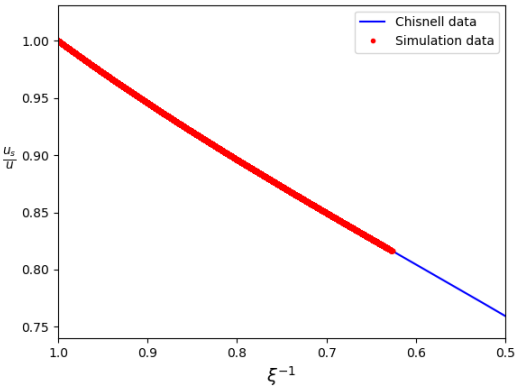

(b)

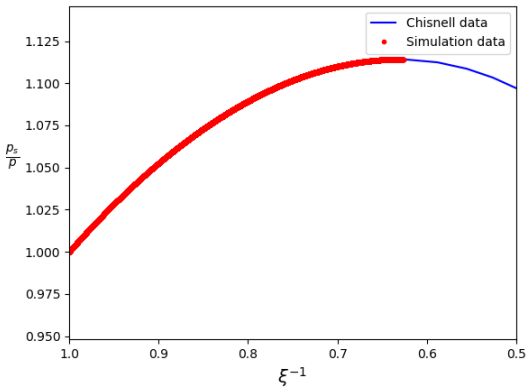

(c)

Figure 4.1: Computations of flow initialization using the Chisnell approximation. The ratios of density, velocity and pressure behind the converging shock wave are displayed with respect to the static conditions of the flow ahead of the shock.

4.3 Initial Conditions

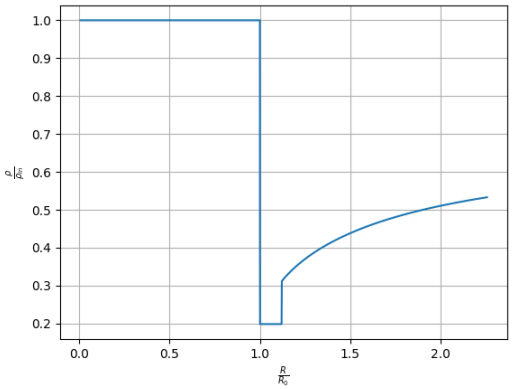

(a) Initial normalized density at the domain

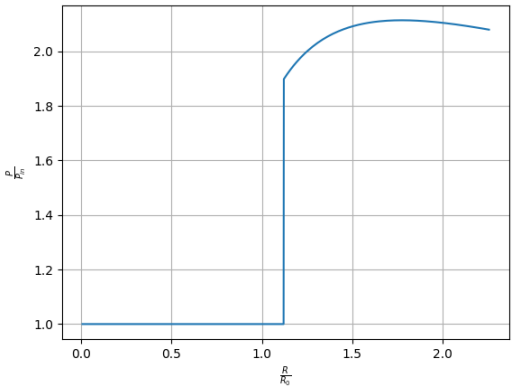

(b) Initial normalized pressure at the domain

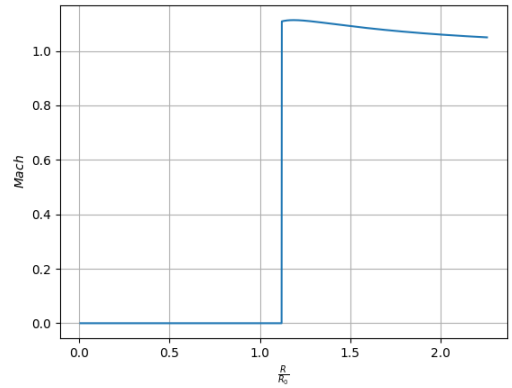

(c) Initial mach number at the domain

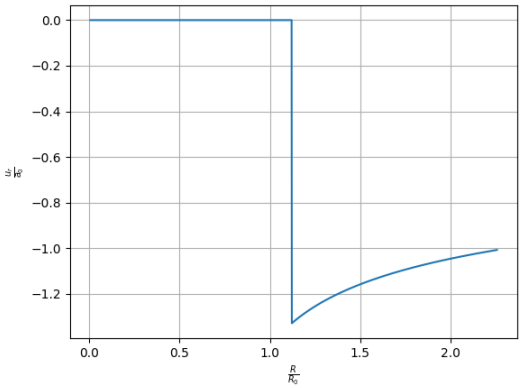

(d) Initial normalized velocity at the domain

Figure 4.2: Initial conditions of the surveyed fluid system.

The flow behind the convergent shock wave is initialized by the solution obtained by Chisnell to avoid spurious oscillations on the wave. In such terms, the flow properties behind the shock wave varies according to the radial distance from the convergence center. A zone of unshocked air is added in between the shocked zone and the target which is composed of Sulfur Hexafluoride (SF_6) in the present work. Finally, the SF_6 target is initialized with similar properties as the unshocked air but with its respective density of $\rho_{SF_6} = 6.17\frac{kg}{m^3}$. The flow initialization is shown in figures 4.3 and 4.3 for constant amplitude and constant wavenumber respectively.

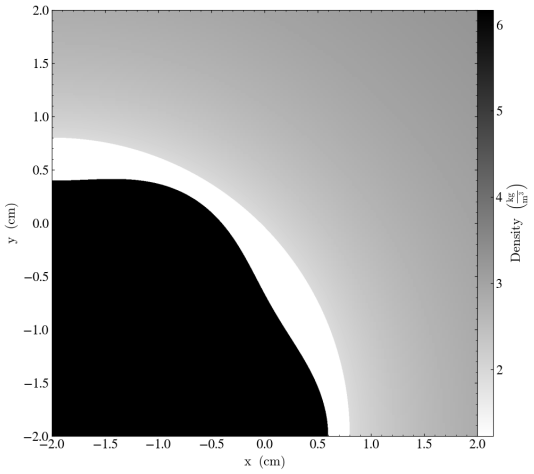

(a) $a = 1\text{mm}$ and $k = 6$

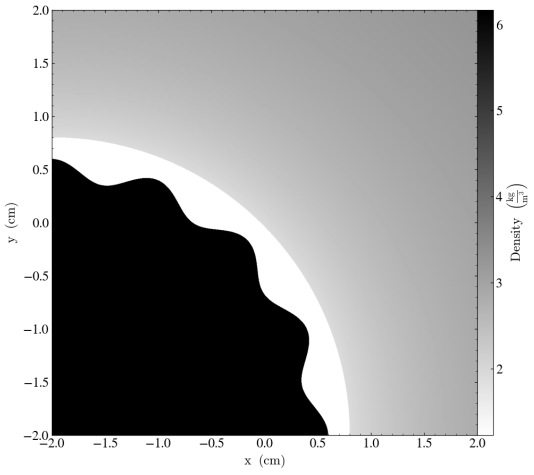

(b) $a = 1\text{mm}$ and $k = 16$

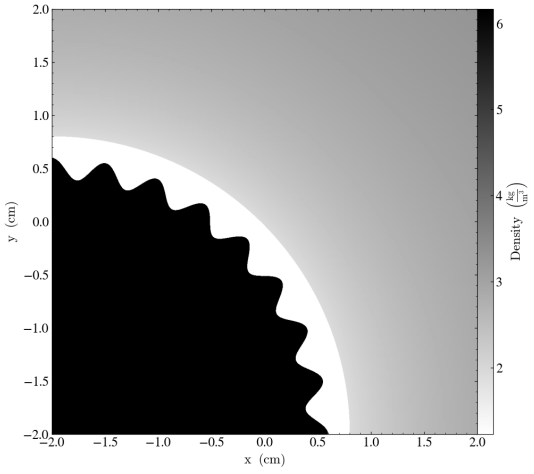

(c) $a = 1\text{mm}$ and $k = 32$

Figure 4.3: Density field at initialization for constant amplitude.

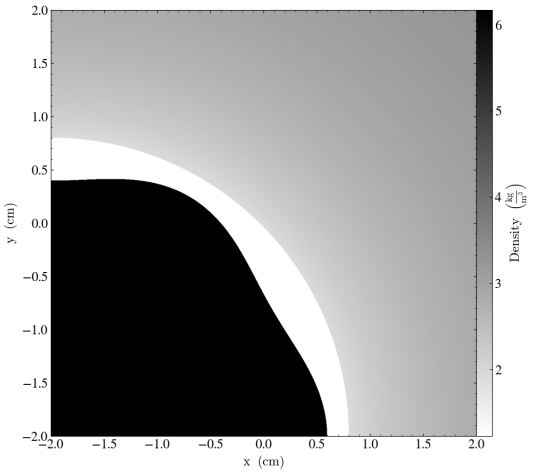

(a) $a = 1$mm and $k = 6$

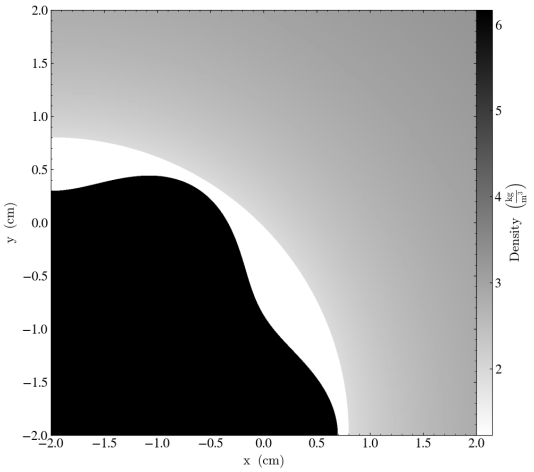

(b) $a = 2$mm and $k = 6$

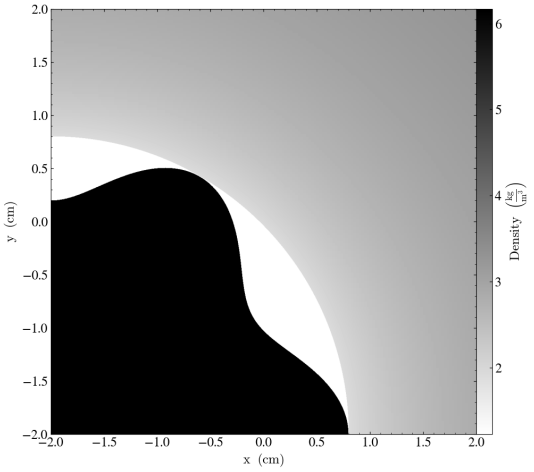

(c) $a = 3$mm and $k = 6$

Figure 4.4: Density field at initialization for constant wavenumber.

4.4 Grid Resolution Convergence Study

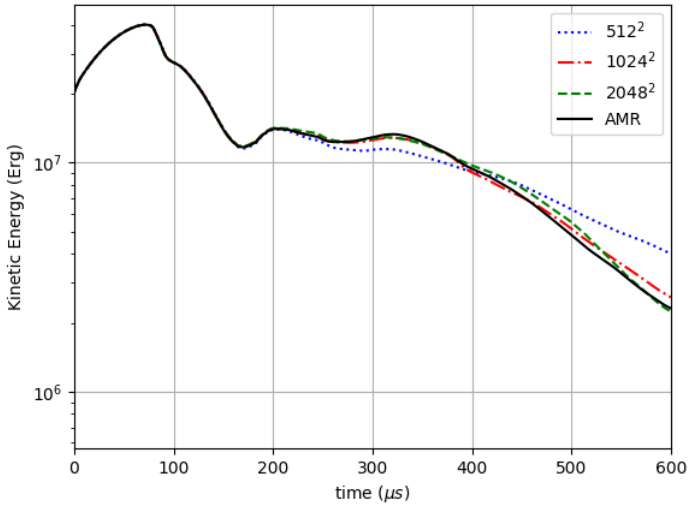

Figure 4.5: Kinetic energy for 4 different grid resolutions. The agreement in terms of energy for the high resolution cases is good with the AMR grid resolution with 4 levels of refinement. Thus, we consider the AMR grid as acceptable results for the present work.

The capabilities of the FLASH code allow the user to test several geometries when it comes to mesh generation. It is possible to use spherical/cylindrical or Cartesian meshes within the framework of the FLASH code. It has been argued that for a better shaping of the interface perturbations, a Cartesian mesh performs better in minimizing the grid-induced turbulence(Joggerst et al., 2014) due to its step-like structure which shapes in a smoothly fashion the wave-like density discontinuities. On the other hand, a spherical (or cylindrical in 2D) mesh shall provide an almost-perfect convergent shock wave while the Cartesian mesh obviously shapes poorly a imploding shock wave, inducing more instability to the interface when hitting the interface. Arguing that the interface shape is more critical than the shock wave itself in the present study, a Cartesian mesh is generated using the FLASH-built-in Paramesh API.

The structured-Cartesian grid resolutions considered for a convergence study are: 512^2, 1024^2, 2048^2 and an AMR mesh with 4 levels of refinement at pressure and density discontinuities. The AMR criteria elected assists to localize very small elements at the convergent shock wave (and subsequent reflected and refracted shock and expansion waves) and at the vicinity of density discontinuities such as contact discontinuities provoked by the shock waves themselves and the main density interface with its late mixing layer.

From figure 4.5 is observed that a coarse grid generated at the computational domain as a Cartesian mesh of resolution 512×512 in the vertical and horizontal axis respectively under-predicts the amount of energy in the flow. Doubling the grid resolution in both dimensions provides more small-scale eddy interaction than the previous grid. A fixed-size grid of resolution 2048^2 represents an almost equal amount of energy as shown in figure 4.5 with the drawback of spending more time computationally and solutions with high storage needs. An AMR grid provides an equivalent energy representation at late times as the finniest fixed-block-size grid analyzed; the advantage is the reduced storage space at the expense of a more complicated post-processing. The AMR grid is chosen as default for the simulations presented in this disquisition as the AMR grid interpretation is already implemented by the yt API in Python.

5. Results

Although a full turbulence analysis and quantification should be accomplished in a three-dimensional framework, much knowledge and analysis can be gathered in two-dimensional geometries. Based on the statement by Mikaelian in which he asserts that every event that takes place in spherical geometries for the problem in question also occurs in a two-dimensional coordinate system(Mikaelian, 2005). Accounting that assertion, most of the results in the present work are extracted from two-dimensional simulations but the three-dimensional effects are briefly addressed as well.

The main phenomena lacking presence in two dimensions is vortex stretching (VS). The VS in the present fluids radial stratified system and in general is caused by the lack of a velocity component in a third dimension. In other words, in two dimension the vorticity, defined as $\omega = \nabla \times u$, is located in a direction orthogonal, say z, to the plane in which the velocity field dwells, say the $x - y$ plane; VS corresponds to the second term of the right hand side of equation 2.2 which involves a dot product. Such projection denoted by the inner product shall be zero if considering a z-only vector dot a vector in the $x - y$ plane, i.e. $\omega \cdot \nabla u = 0$. Thus, VS is only possible if considering a velocity field dwelling within the three known spatial dimensions. The expected effect of VS in the problem of interest is a direct affectation in the development of the mixing layer. For a three-dimensional mixing layer it is expected to have a certain saturation (Prasad, Rasheed, Kumar, & Sturtevant, 2000) due VS therefore showing a smaller mixing layer extent than in polar coordinates.

The interest of this work lies in the affectation of the initial conditions of the perturbation at the density interface formed by two radially stratified fluids and hence VS effects can be neglected in order to facilitate the analysis; nonetheless, more insight can be gain from the analysis in three dimensions at the expense of high computational time and effort.

5.1 Physical Description

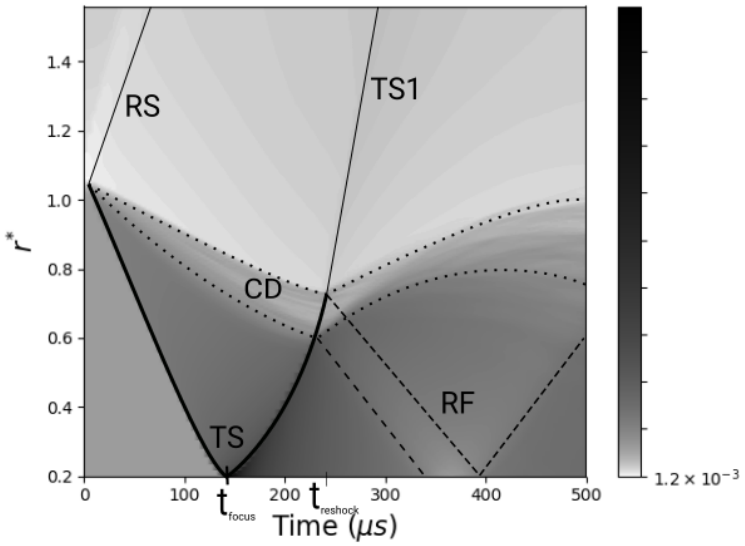

Figure 5.1: rt diagram representing the shock evolution during a simulation.

Although real perturbations in ICF pellets are a combination of different modes i.e. multi-mode, instinctively the analysis of single-mode perturbation becomes a starting point for fully characterize the influence of initial conditions on the interface evolution process. Hence, the amplitude and wavenumber are the variables of interest in this investigation.

$$R(\theta) = R_0 + A\cos\left(k\left(\theta + \phi\right)\right) \tag{5.1}$$

The Chisnell-type shock wave is placed just a few distance away (radially) from the density interface. At the non-dimensional radius of $r^* = 1$ (see fig-

ure 5.1) the shock wave hits the density discontinuity formed by the pocket of SF_6 inside air. An initial interface amplitude decrease is observed as a result of the initial interface compression caused by the first interaction of the convergent shock wave with the induced contact discontinuity (CD). This initial compression observed is a natural response for the light fluid to maintain mechanical equilibrium at the interface and thus a compression-expansion process caused by the imploding shock wave baroclinic vorticity deposition is the first feature observed in this kind of flows. Then, the shock wave bifurcates into a reflected and transmitted or refracted shock waves (RS and TS respectively) as shown in figure 5.1. The change of medium causes RS to leave the domain quickly contrary to TS which propagates slowly (compared to RS) towards the convergence center. RS leaves the computational domain because of the outflow condition imposed. On the other hand, TS travels inside the new SF_6 target slower than in air due to shock refraction caused by the change of medium. As TS moves inward, the amplitude of the mixing layer increases as the bubbles of CD moves inwards as well. The Bell-Plesset effects are a consequence of the geometry in question and they are not observed in planar geometries. At time $t \approx 140\mu s = t_{focus}$ TS auto-reflects at the convergence center and gain strength as the pressure and density at this point are highly augmented by the shock wave.

In ICF, it is at this peculiar point that fusion conditions are desired to be triggered by the shock increased strength. Interestingly, the linear shock propagation after shock auto-focus has become a non-linear shock propagating outwards as seen in figure 5.1 at $t > t_{focus}$. TS is then a divergent strong shock

wave; as it travel outwards, the shock strength is decreased contrary to convergent shock waves. Moments after the shock focus at the convergence center, the interface experiences the opposite case of a heavy fluid penetrating a light gas (SF_6 to air) which inhibits the instability evolution as a consequence of RT stabilization effects(Juchun et al., 2017). At this stage, the RT effects start to develop surpassing the RM and Bell-Plesset effects. Such inhibition of the interface occurs just before the first reshock i.e. TS dynamically interacts again with CD depositing more baroclinic vorticity at the interface at $t \approx 230\mu s = t_{reshock}$. The theoretical prediction becomes challenging at this stage since at reshock, the initial conditions are forgotten as suggested by Thornber et al.(Thornber et al., 2010) and a new non-linear shocked interface is being perturbed. After reshock, a new refraction process takes place at the interface. Recalling the fact that TS is being refracted from a high-density medium into a low-density transmitting medium, the newly transmitted wave correspond to a shock wave while the reflected wave traveling towards the convergence center correspond to a expansion fan (RF) in the high-density gas. RF will experience another auto-focus event at the convergence center. Depending on the strength of RS, there might be a second reshock process as the auto-focus event is able to amplify the strength of a wave. The simulation is stopped at $t = 500\mu s$ because only the mixing after one reshock is of interest in this work.

A second event of interest is observed in this kind of density stratification when the shock wave acts from a high-density to a low-density medium creating a phase inversion of the mixing zone. This event corresponds to the crests of the penetrating fluid stop growing as the bubbles evolve faster inducing a change in

the phase of the non-linear interface. When the reshock occurs, TS1 bifurcates into an outward-going TS2 and an convergent reflected expansion wave. Hence, no more than one phase inversion befalls during the course of the simulation for positive Atwood numbers. We observe an increasing slope after the reshock (see for instance figure 5.2) which is the result of a higher growth rate of the interface. Thus, the reshock process augments the rate at which the interface develops making it grow faster than initially with the interaction with the initial incident shock. Despite the lack of experimental realizations, it is believed that all of the aforementioned physics transpires for positive Atwood numbers.

The RM instability in this case acts twice: at the start of the interface growth process when the main shock wave hits the interface and at the reshock process as an additional impulsive acceleration is deposited at the mixing zone. RT instability start occurring after the impulsive character of the acceleration has passed and the interface inherits a continuous accelerative character. RT takes place at the approximate time frame $100 < t < 200$ and after reshock at late times. One more geometric growth is evidenced as the shell moves in a spherical or cylindrical system: BP effects. Finally, KH instability is observe as a secondary instability due to the shear interactions of the mushroom-like structures with the medium. The growth of the mixing zone can be estimated. In both equations 2.7 and 2.8 the growth due to the RMI corresponds to the second term of the right hand side while the RTI and BP effects on the growth of the mixing layer is described by the last term in the right hand side of the same equations.

Two parameters of the initial perturbation wave are of importance, namely, the wavenumber (wavelength) and the amplitude. For analyzing the influence of each parameter in the late-time mixing layer development, one is kept constant while varying the other.

5.1.1 Wavenumber Effects

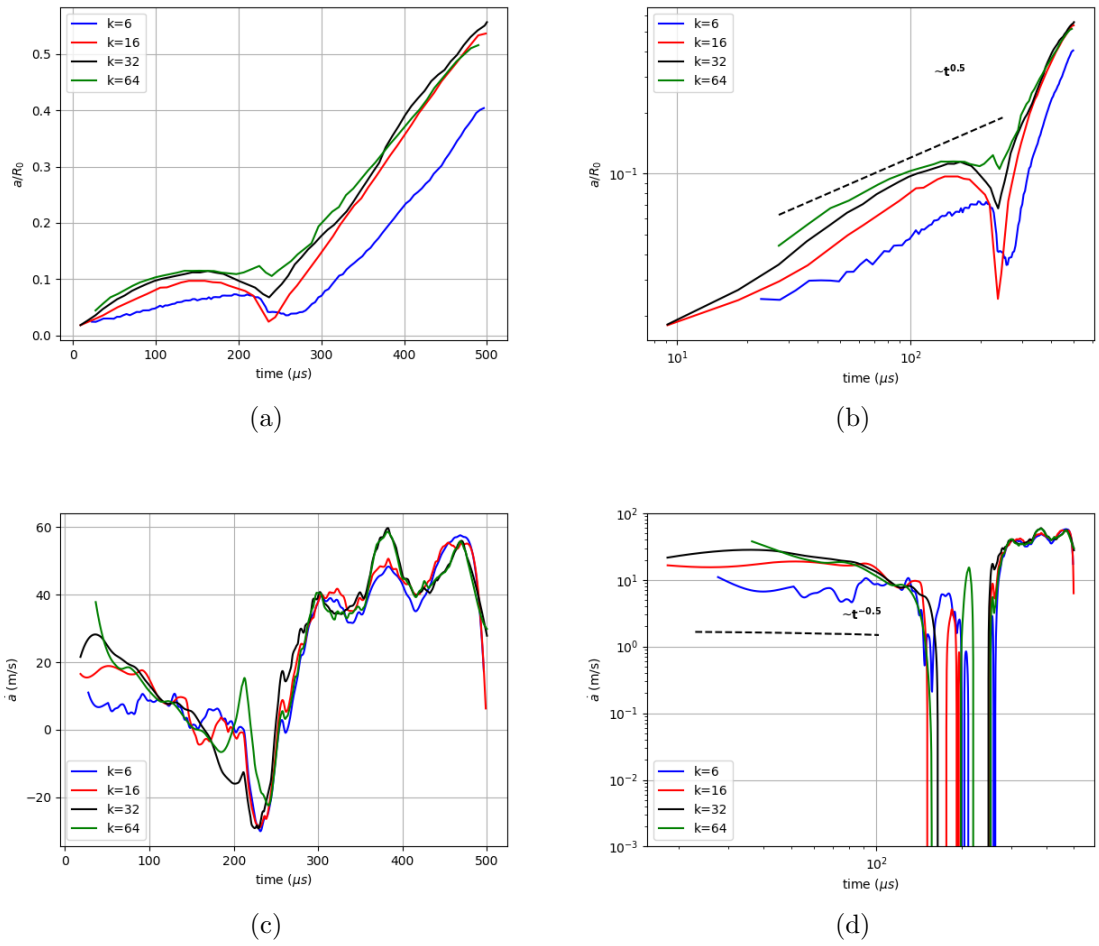

(a) (b)

(c) (d)

Figure 5.2: Mixing layer development for three different wavenumbers. The initial amplitude is kept constant as $a_0 = 10\% R_0$. The plots correspond to the width or amplitude of the mixing layer in a) normal and b) log scale and the mixing layer growth rate in c) regular and d) log scale

The inception of the interaction between coherent structures in the flow is dependent on the proximity of its bubbles and spikes. When the wavelength

is long[1], the interaction between two partially-developed mushroom-like bubbles might start later than perturbations with closer peak-to-peak distance in which eddies from different sources interact with its neighborhood eddies at earlier times. Hence, the peak proximity has more significant scope in mixing and they are more likely to occur rather than having a sphere with big differences in amplitude on its perturbation spectra.

We maintain a constant initial small amplitude of $a_0 = 0.25$mm and the wavenumbers analyzed here are 6, 16, 32 and 64 corresponding to $a_0/\lambda = 0.00955$, 0.0255, 0.051 and 0.102 respectively with $\lambda = 2\pi R_0/k$. The importance of analyzing each mode separately is crucial to later understand the interaction between modes for a more realistic multimode perturbation wave at the interface.

Single-Mode Perturbation

The lowest frequency case ($k = 6$) presents considerable contrasts in comparison with the different cases. Before reshock and after the previously-described interface compression, a different concavity is observed in Figure 5.2(a) compared with higher frequencies. This is directly related to the acceleration of the interface width. The main remark is that contrary to the cases of $k = 16$ and $k = 32$, the case of $k = 6$ displays initially a linear shape in the range $10\mu\text{s} \leq t \leq 200\mu\text{s}$. The linearity in such case suggests a linear growth rate at this stage before reshock when the wavenumber of the perturbed interface is low (see figure 5.2(c)). Interestingly, increasing the wavenumber changes the concavity of the interface amplitude at early times as depicted in Figure 5.2(a). Furthermore, another noticeable feature of augmenting the wavenumber of the

[1]Wavelength is interchangeably used with wavenumber to describe the same effects. Long (short) wavelengths are equivalent to low (high) wavenumbers; thus, the reader can interpret wavelength as well as wavenumber in a similar fashion.

initial perturbation at early times before reshock is that the acceleration tends to a constant acceleration of the interface amplitude thus confirming the initial linear growth rate for RM instability. However, Implicit Large Eddy Simulations (ILES) filter small scales and then use the inherently dissipation for generating such scales.

After reshock the perturbed interface appears to present the same behavior qualitatively regardless of the wavenumber. The contraction of the interface or the RT stabilization effect can be treated as a reduction in the growth rate of the interface amplitude. Reshocking the interface results in a second compression/expansion process of the mixing layer. The incident mach number at reshock is greater than the initial mach number because of the shock auto-focuses at the convergence center and hence the mixing layer after reshock starts to become wider caused by the rise in growth rate. Although reshocking the mixing layer has similar results for all wavenumbers analyzed, the behavior at late time is distinct. The growth rate of the mixing layer for the cases with $k = 6$, $k = 16$ and $k = 32$ at final times of the simulations present a higher growth rate than the case of highest wavenumber $k = 64$ as seen in figure 5.2(c) at $t > 425\mu s$. It is suggest that such phenomena in the growth rate of the interface width is caused by the interaction of different type of waves. Precisely, the reshock is causing a shock bifurcation process in which a shock wave is transmitted to the light gas while an expansion fan is being reflected towards the convergence center of the heavy medium. Thus, the flow behind the exploding transmitted shock wave is being compressed while the flow behind the imploding expansion fan is being expanded. In more chaotic interfaces as for the cases of

$k = 64$, these compressibility effects are better remarked because of the complex wave interactions. Hence, we prompt that for high wavenumbers after reshock, the flow compression dominates over the flow expansion resulting in a deceleration of the mixing layer growth speed. In other words, flow compression decelerates the flow behind the transmitted shock front and at late time when the shock front is sufficiently far from the mixing layer, the pressure starts to decay resulting in a velocity increment causing an sudden acceleration of the mixing layer width. It is also an evidence that if $a_0/\lambda > 0.1$, the linear regime does not hold anymore. Observe also in figure 5.2(a) that at final times the mixing layers originated by the perturbation waves initialized with wavenumbers $k = 16$ and $k = 32$ surpass the mixing layer width of the case with initial wavenumber of $k = 64$. After such event, no more shock waves are expected to interact in the timeframe of our simulations with the mixing layer hence we observe a constantly growing mixing layer until the saturation point where no more energy is being deposited at the interface. This significant demeanor of the mixing layer as the wavenumber of the initial perturbation is increased may render to the belief that the initial conditions are not completely forgotten for the RM instability in convergent geometries; nevertheless, experimental evidence is necessary to confirm this scenario. Furthermore, figures 5.2(b) and 5.2(d) suggest that before reshock the slope of the scaling law of the mixing layer width and growth rate are $\sim t^{0.5}$ and $\sim t^{-0.5}$ which doubles the scaling law exponent obtained in a planar shock tube case (Zeng, Pan, Sun, & Ren, 2018).

Multi-Mode Perturbation

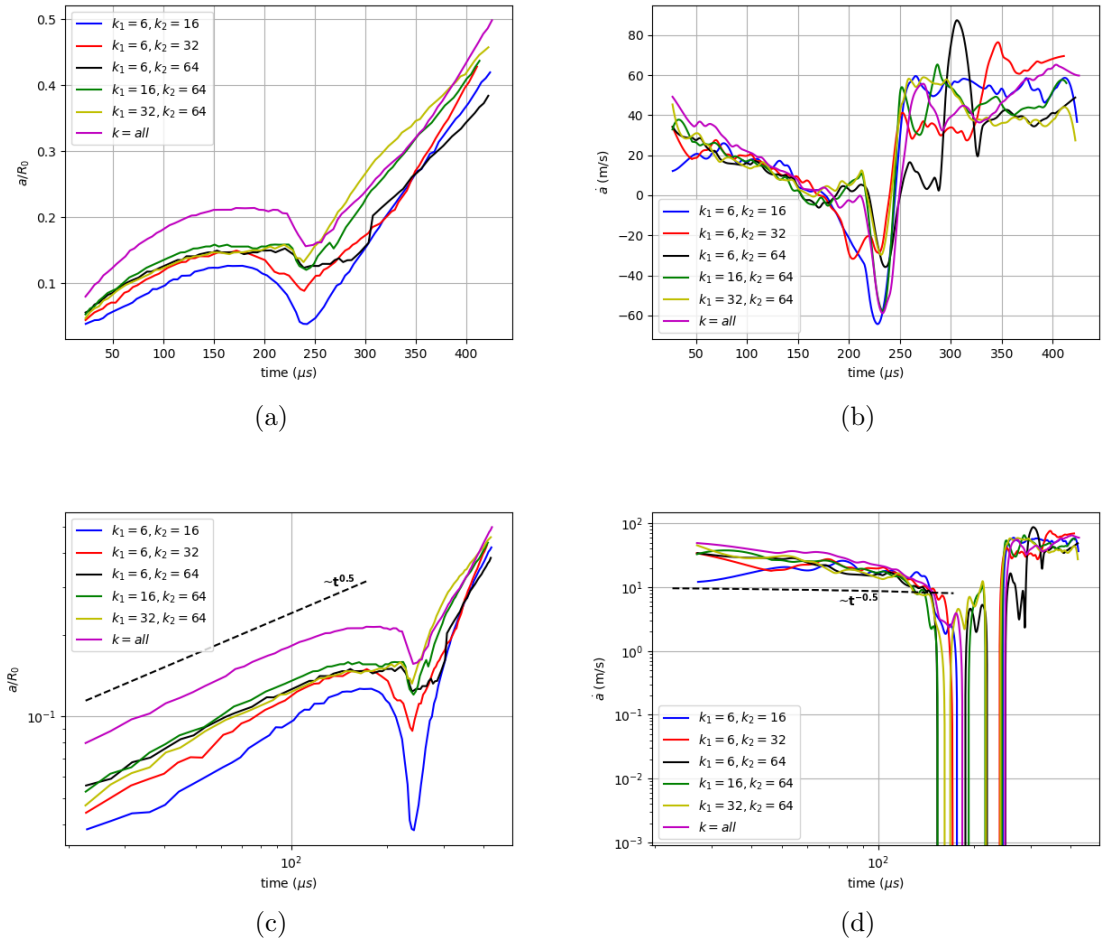

Figure 5.3: Mixing layer width and growth rate for initial constant amplitude and variable wavelength multimodal interface perturbation

More modes are added in the following way: first, two different waves are superimposed with different amplitudes and wave lengths and then all the four wavenumber modes are superimposed in a single perturbation wave. Much insight can be gain by fully-characterizing the perturbation rather than placing randomly-generated perturbations. The analysis here is also carried out in terms of the single mode waves analyzed previously as the main interest of this work is in the affectation on late-time mixing and mixing zone development as a function of the perturbation initial conditions. The single mode analysis does not

include any mixing quantification as all the analysis regarding mixing for the multimode and isolated modes is performed at this stage. In reality, ICF-like conditions are represented by multimode perturbations and much of the analysis is performed in this section of this work. Furthermore, a small amplitude is considered again in order to reduce the effects of amplitude since the main interest in this section is just the affectation of the initial wavelength. Forward in the analysis, high amplitudes are analyzed.

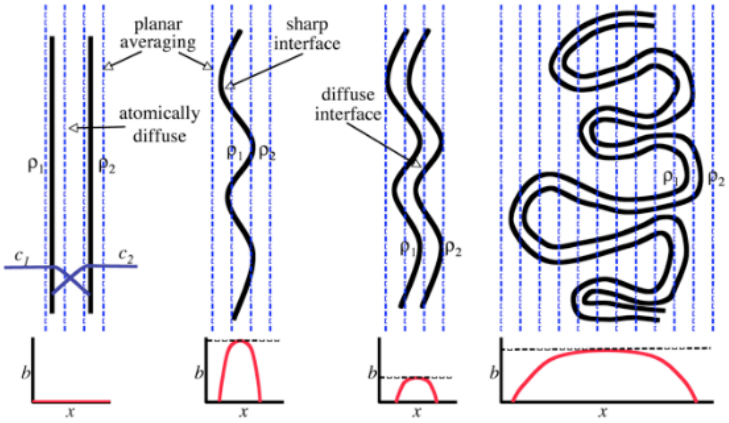

Figure 5.4: A representation of the b parameter or density-specific volume correlation for planar averaging along the dashed lines. Image reproduced from LANL LA-UR-11-04773 report Stalsberg, 2011.

Mixing is quantified initially by the density-specific volume correlation b. This parameter is zero in the case of an atomically-diffuse interface. As the interface grows, the parameter b increase; hence, the higher the b the less the mixing it is describing (see figure 5.4). This parameter formally is defined as

$$b = \overline{\rho' \left(\frac{1}{\rho}\right)} - 1 \tag{5.2}$$

The correlation presented in equation 5.2 is implemented in order to compute mixing in different radial locations in the whole computational domain and then calculating averages. For a complete description and formalization of the b

correlation, the reader is refered to a different source (Stalsberg-Zarling & Gore, 2011).

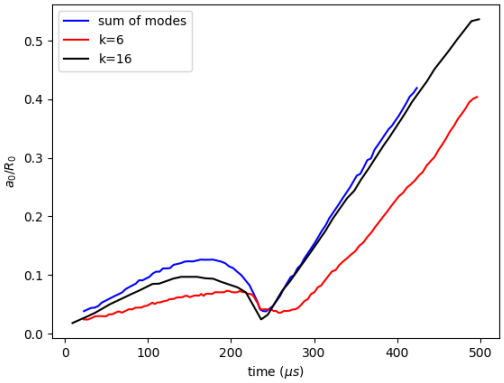

(a) $k_1 = 6$, $k_2 = 16$

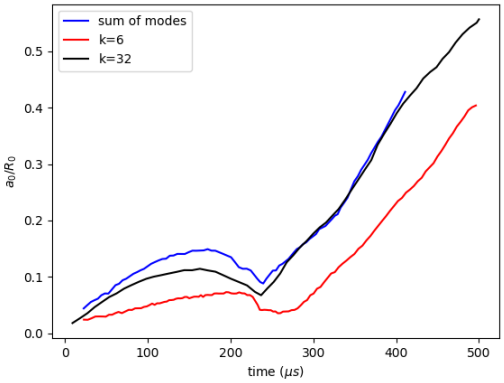

(b) $k_1 = 6$, $k_2 = 32$

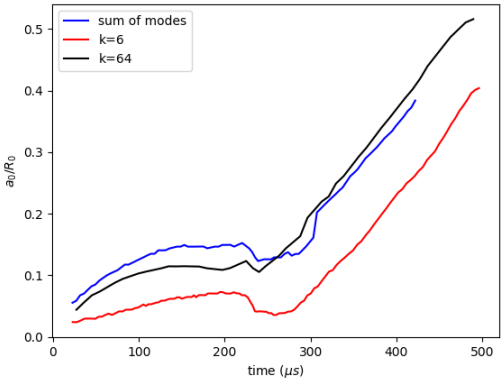

(c) $k_1 = 6$, $k_2 = 64$

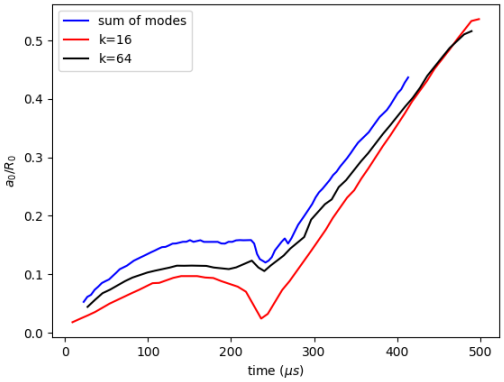

(d) $k_1 = 16$, $k_2 = 64$

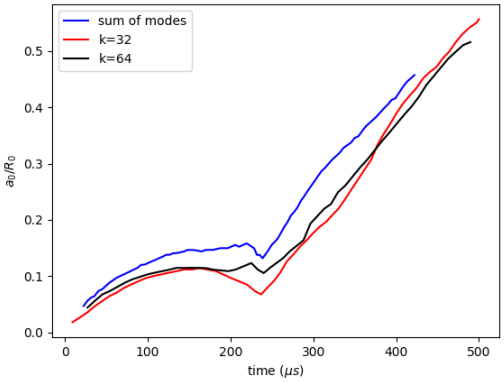

(e) $k_1 = 32$, $k_2 = 64$

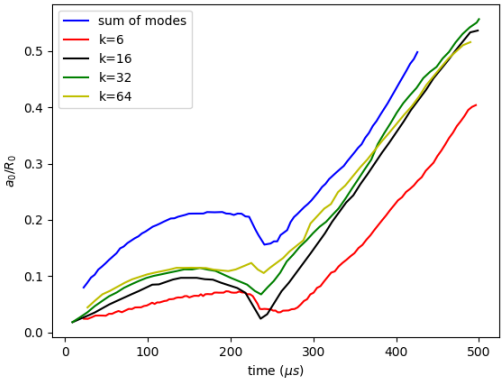

(f) $k_1 = 6$, $k_2 = 16$, $k_3 = 32$, $k_4 = 64$

Figure 5.5: Mixing layer widths of all multimode perturbations analyzed with its single modes composing the total wave.

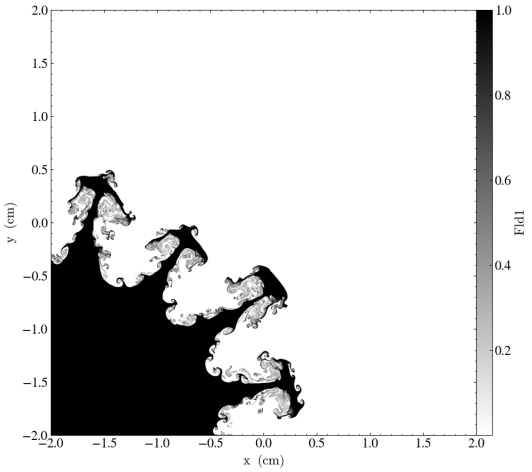

(a) $k_1 = 6$, $k_2 = 16$

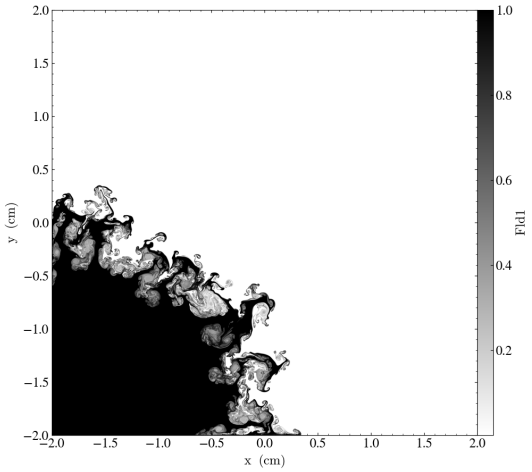

(b) $k_1 = 6$, $k_2 = 32$

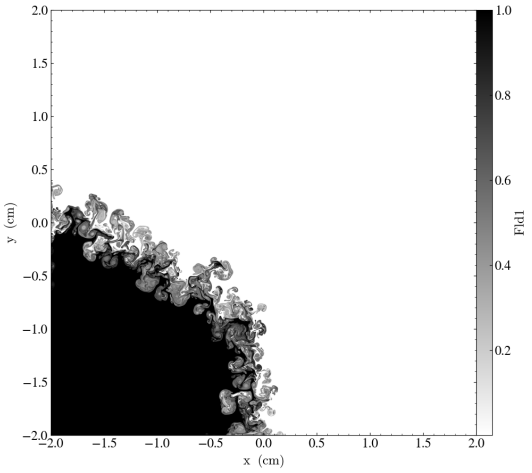

(c) $k_1 = 6$, $k_2 = 64$

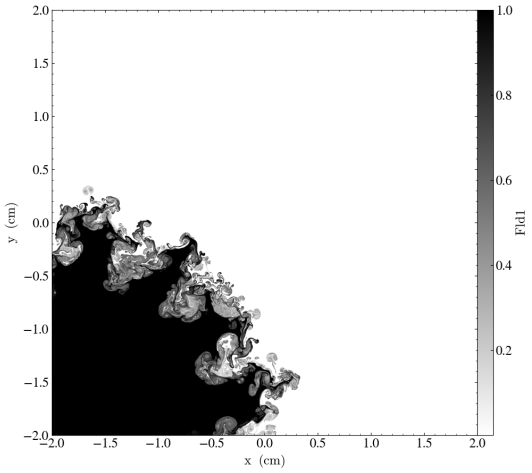

(d) $k_1 = 16$, $k_2 = 64$

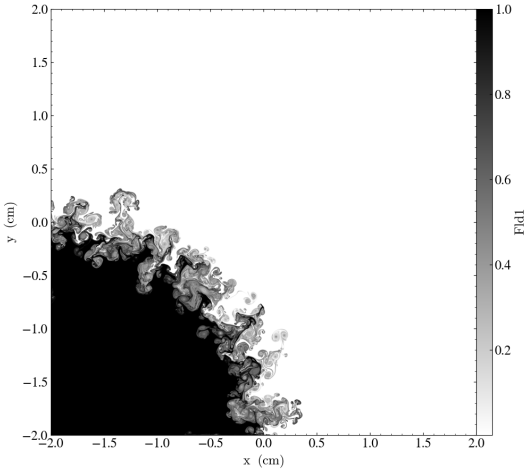

(e) $k_1 = 32$, $k_2 = 64$

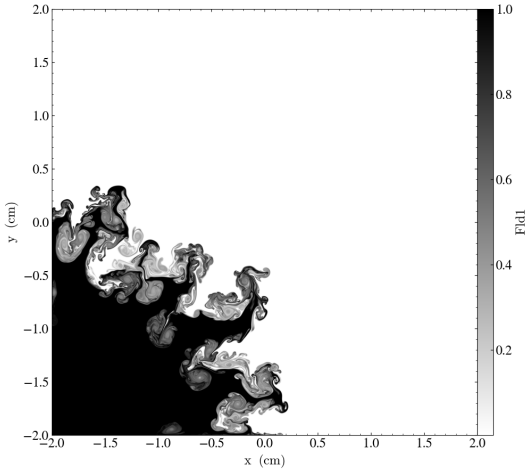

(f) $k_1 = 6$, $k_2 = 16$, $k_3 = 32$, $k_4 = 64$

Figure 5.6: Mass fraction surface plot for each 2d multimode case analyzed at the final time of simulation. Moments after reshocking the interface but before the second reshock $t = 500\mu s$. The inital amplitude is $a_0 = 0.25mm$.

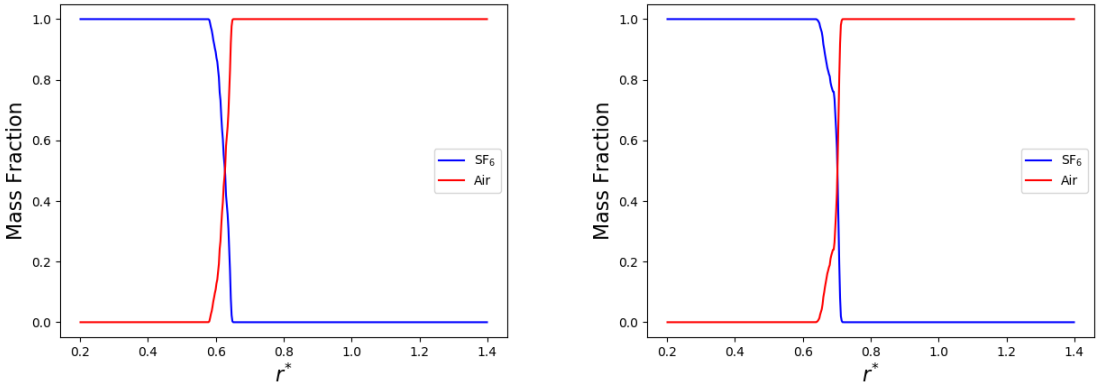

(a) $t = t_{res} = 230\mu s$

(b) $t = t_{res} = 260\mu s$

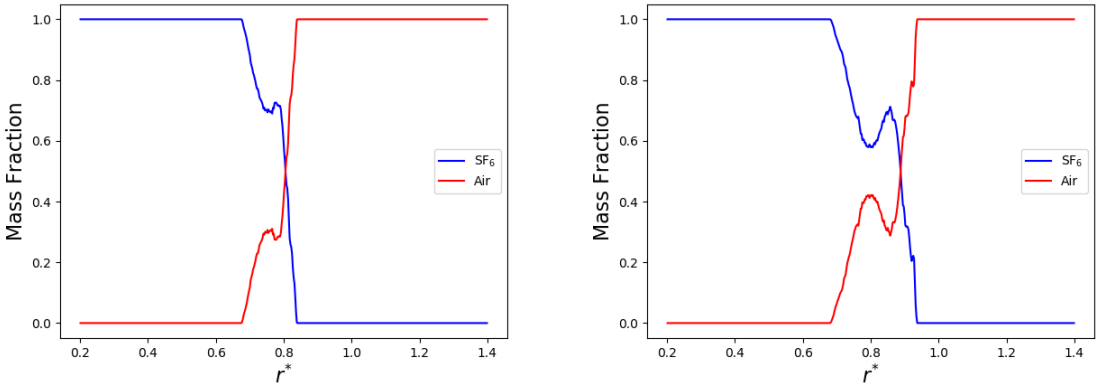

(c) $t = t_{res} = 300\mu s$

(d) $t = t_{res} = 340\mu s$

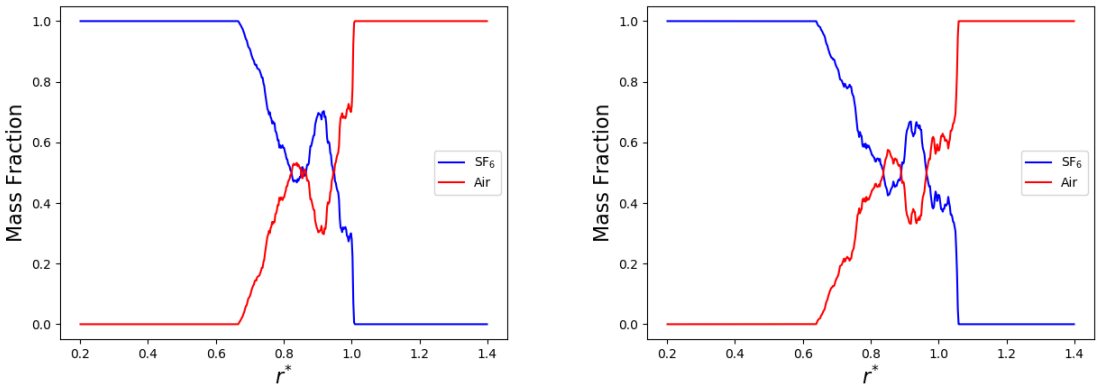

(e) $t = t_{res} = 380\mu s$

(f) $t = t_{res} = 415\mu s$

Figure 5.7: Mass fraction during and after reshock for $a = 0.25mm$ and $k_1 = 6$, $k_2 = 16$

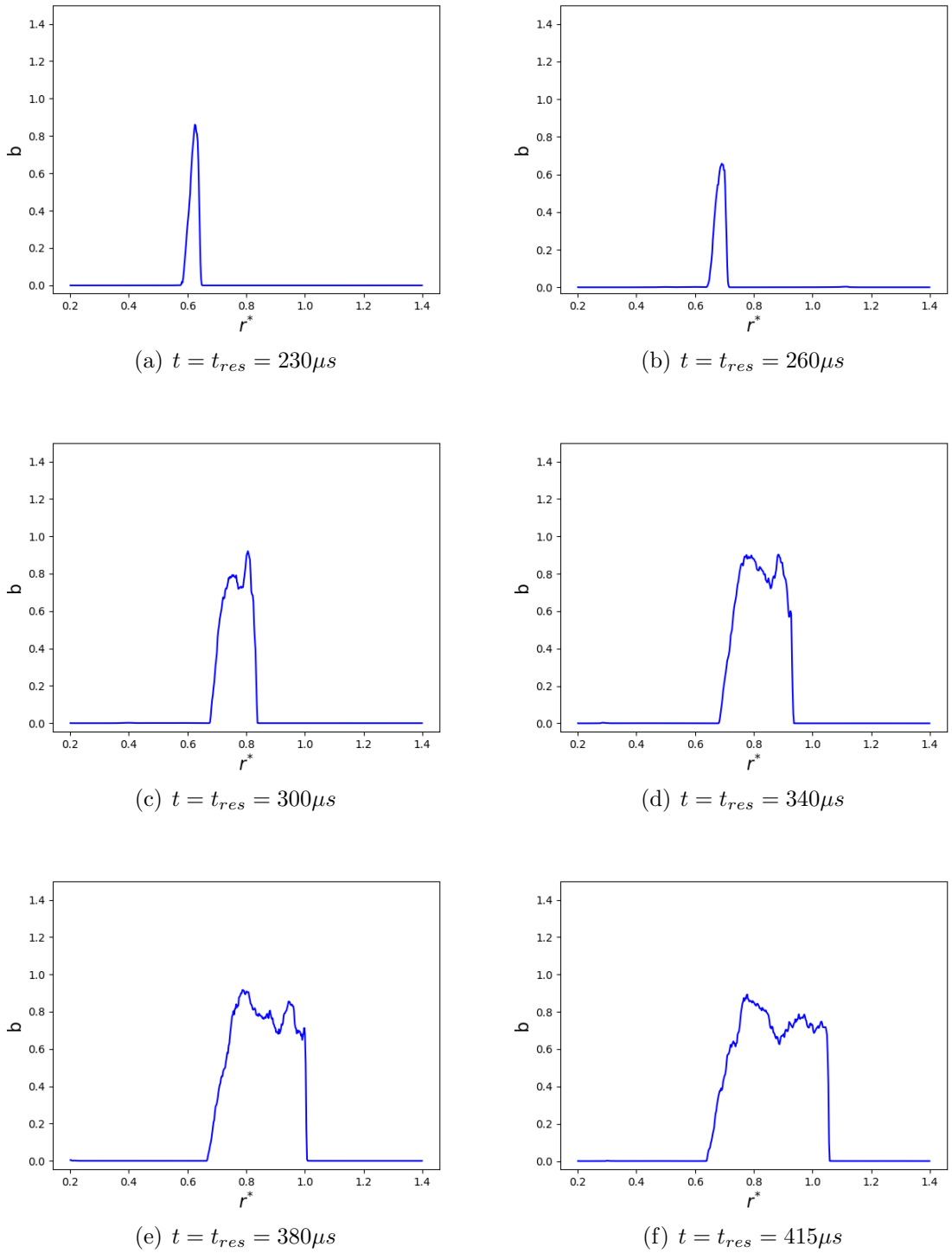

(a) $t = t_{res} = 230\mu s$

(b) $t = t_{res} = 260\mu s$

(c) $t = t_{res} = 300\mu s$

(d) $t = t_{res} = 340\mu s$

(e) $t = t_{res} = 380\mu s$

(f) $t = t_{res} = 415\mu s$

Figure 5.8: Density-specific volume correlation, a.k.a b parameter, during and after reshock for $a = 0.25mm$ and $k_1 = 6$, $k_2 = 16$

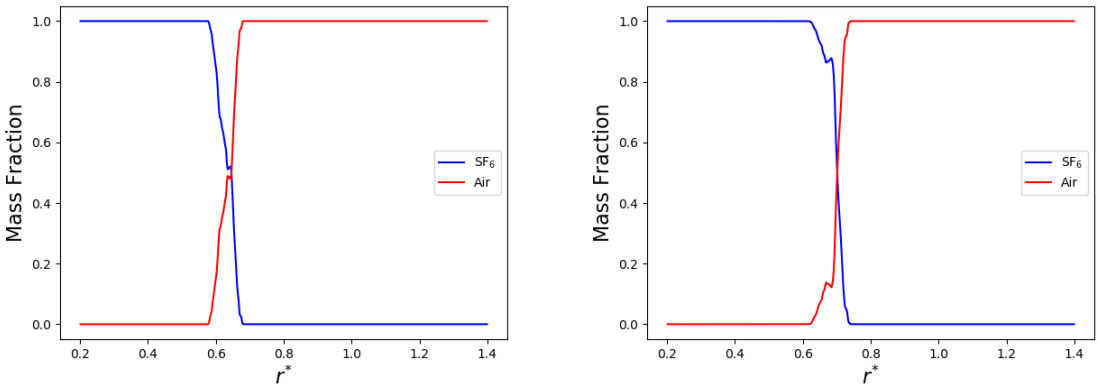

(a) $t = t_{res} = 230\mu s$

(b) $t = t_{res} = 260\mu s$

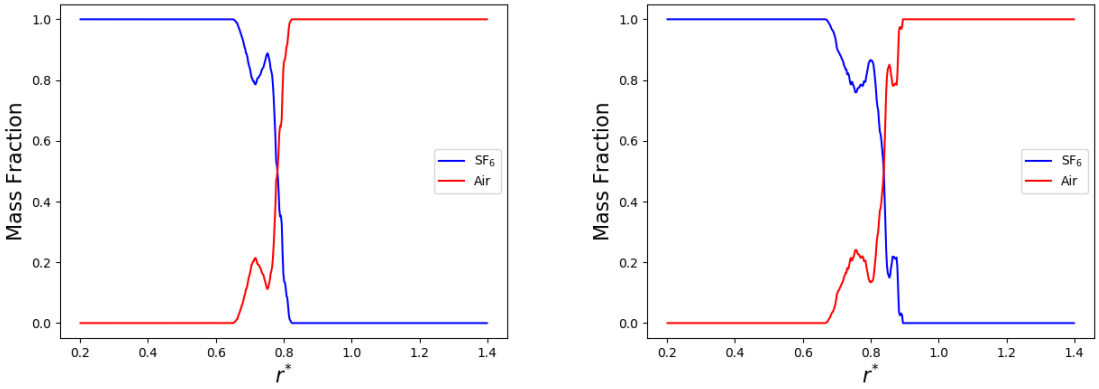

(c) $t = t_{res} = 300\mu s$

(d) $t = t_{res} = 340\mu s$

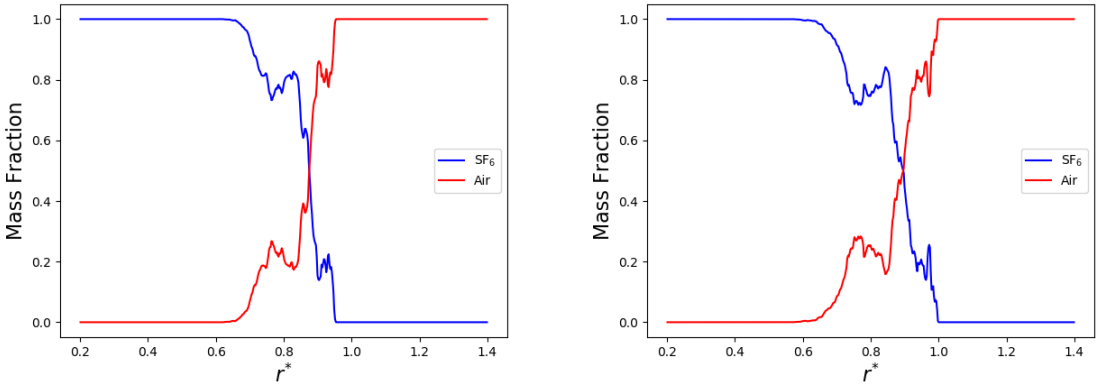

(e) $t = t_{res} = 380\mu s$

(f) $t = t_{res} = 415\mu s$

Figure 5.9: Mass fraction during and after reshock for $a = 0.25mm$ and $k_1 = 6$, $k_2 = 32$

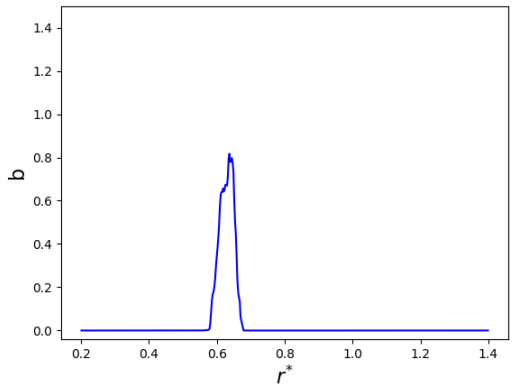

(a) $t = t_{res} = 230\mu s$

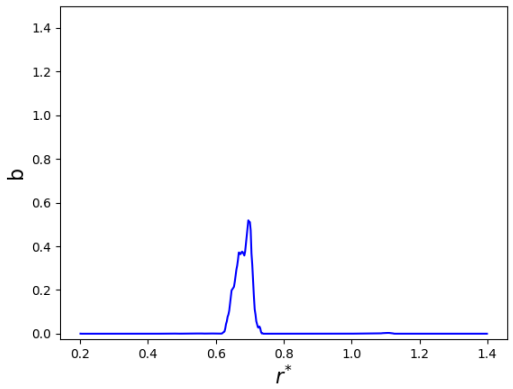

(b) $t = t_{res} = 260\mu s$

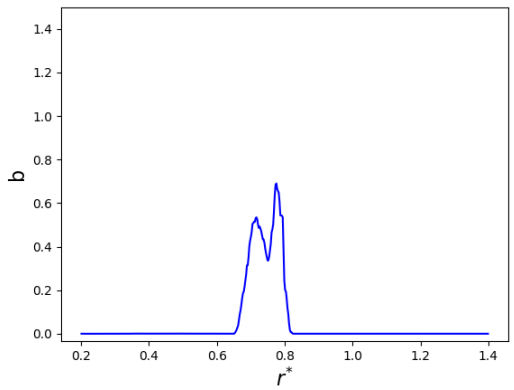

(c) $t = t_{res} = 300\mu s$

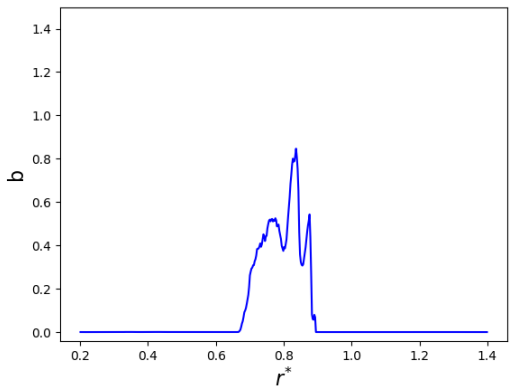

(d) $t = t_{res} = 340\mu s$

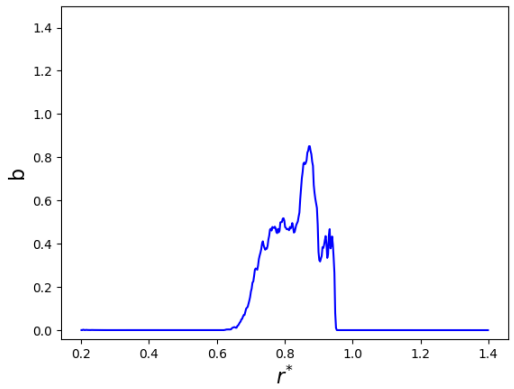

(e) $t = t_{res} = 380\mu s$

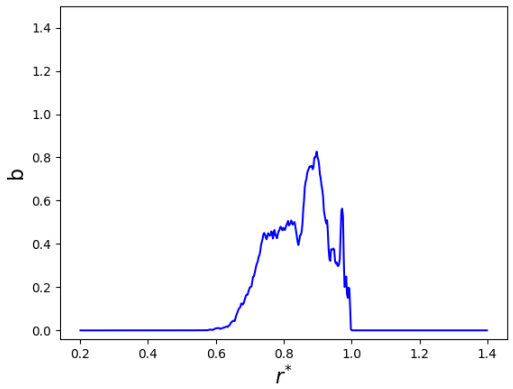

(f) $t = t_{res} = 415\mu s$

Figure 5.10: Density-specific volume correlation, a.k.a b parameter, during and after reshock for $a = 0.25mm$ and $k_1 = 6$, $k_2 = 32$

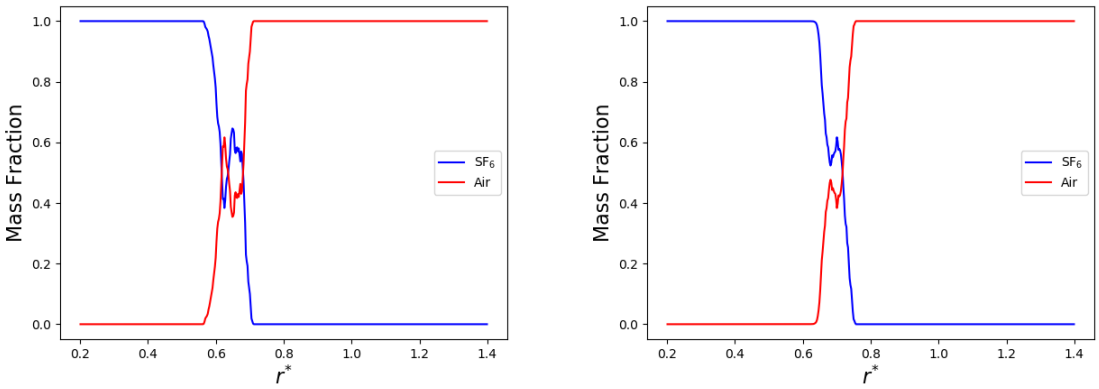

(a) $t = t_{res} = 230\mu s$

(b) $t = t_{res} = 260\mu s$

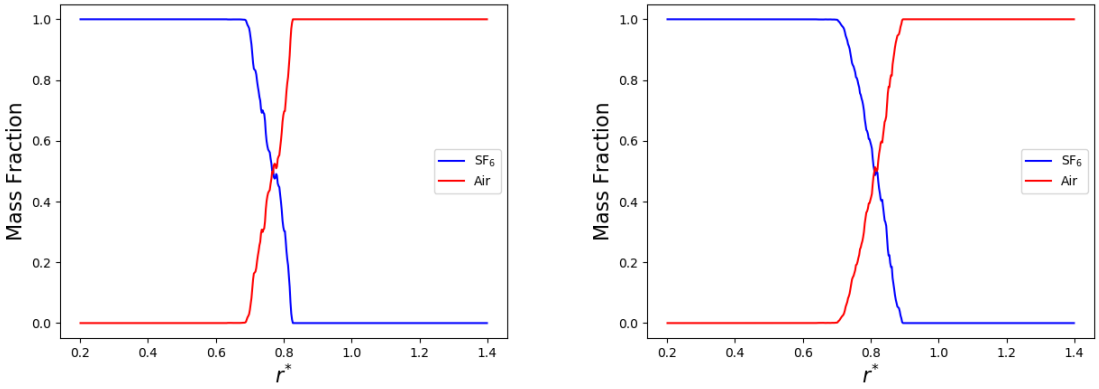

(c) $t = t_{res} = 300\mu s$

(d) $t = t_{res} = 340\mu s$

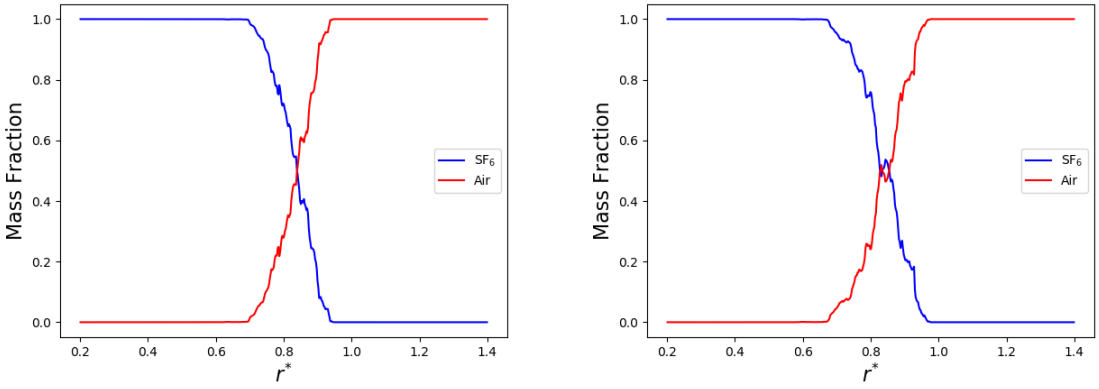

(e) $t = t_{res} = 380\mu s$

(f) $t = t_{res} = 415\mu s$

Figure 5.11: Mass fraction during and after reshock for $a = 0.25mm$ and $k_1 = 6$, $k_2 = 64$

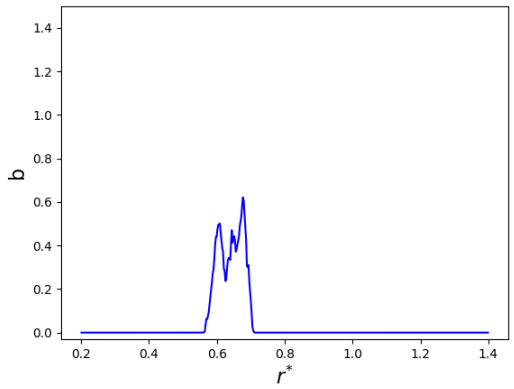

(a) $t = t_{res} = 230\mu s$

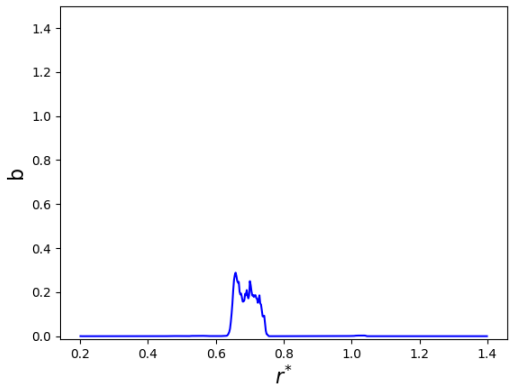

(b) $t = t_{res} = 260\mu s$

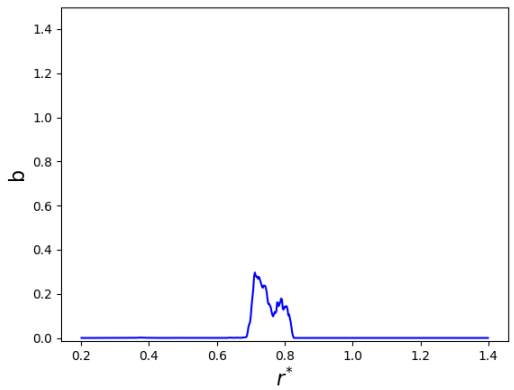

(c) $t = t_{res} = 300\mu s$

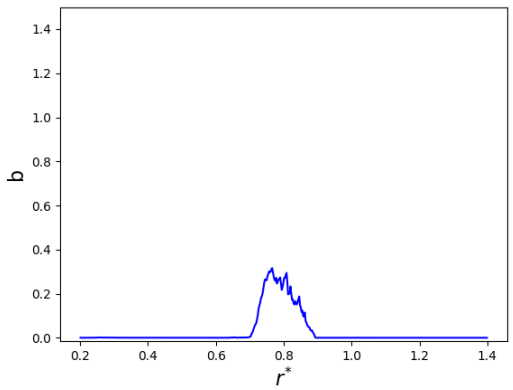

(d) $t = t_{res} = 340\mu s$

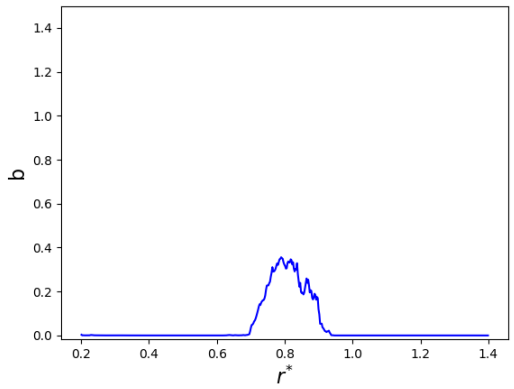

(e) $t = t_{res} = 380\mu s$

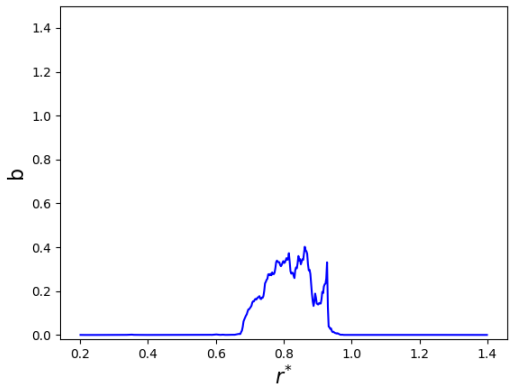

(f) $t = t_{res} = 415\mu s$

Figure 5.12: Density-specific volume correlation, a.k.a b parameter, during and after reshock for $a = 0.25mm$ and $k_1 = 6$, $k_2 = 64$

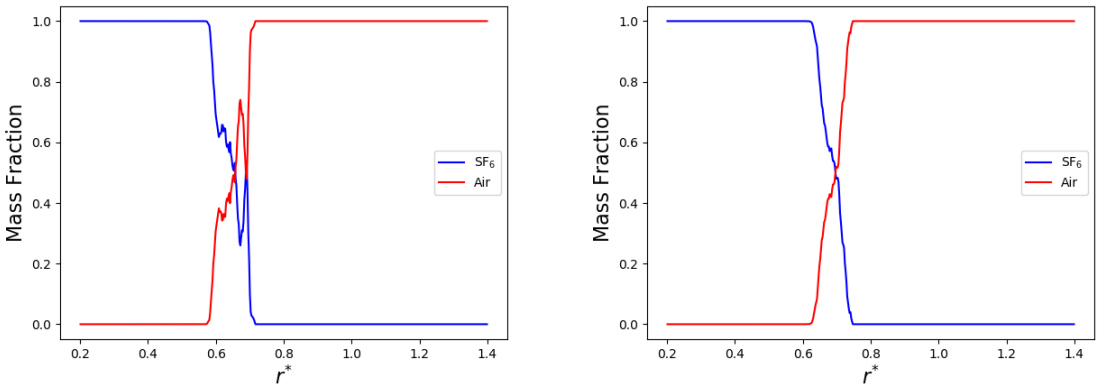

(a) $t = t_{res} = 230\mu s$

(b) $t = t_{res} = 260\mu s$

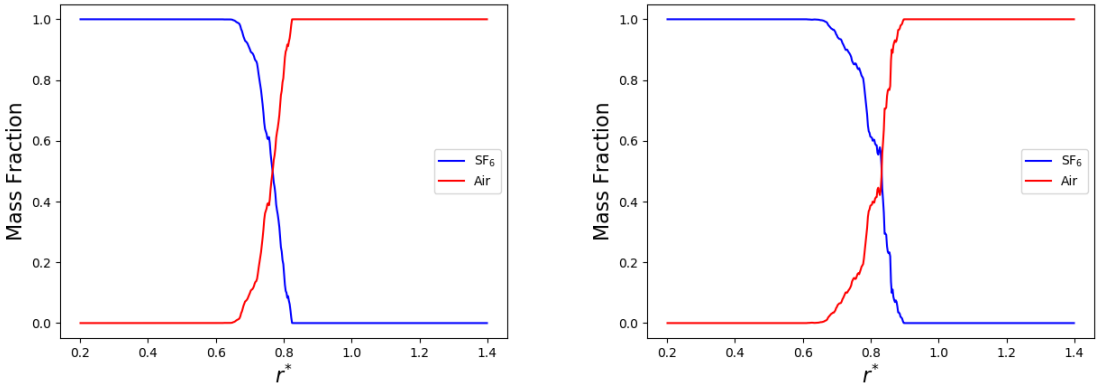

(c) $t = t_{res} = 300\mu s$

(d) $t = t_{res} = 340\mu s$

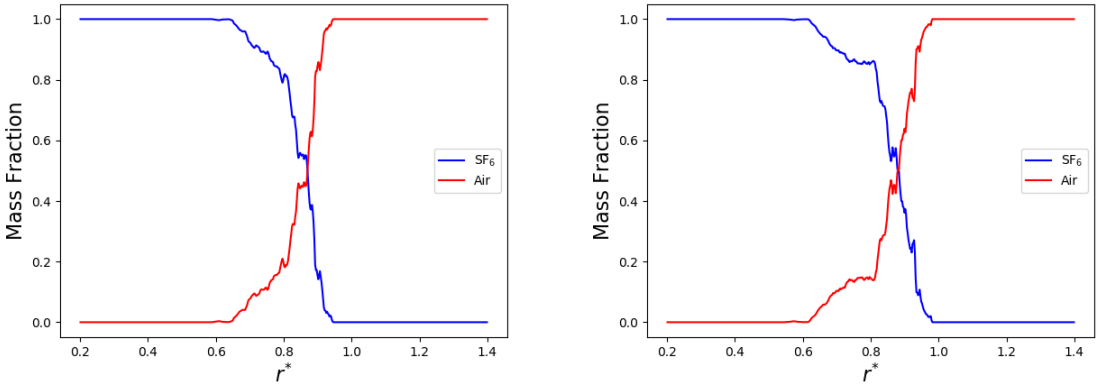

(e) $t = t_{res} = 380\mu s$

(f) $t = t_{res} = 415\mu s$

Figure 5.13: Mass fraction during and after reshock for $a = 0.25mm$ and $k_1 = 16$, $k_2 = 64$

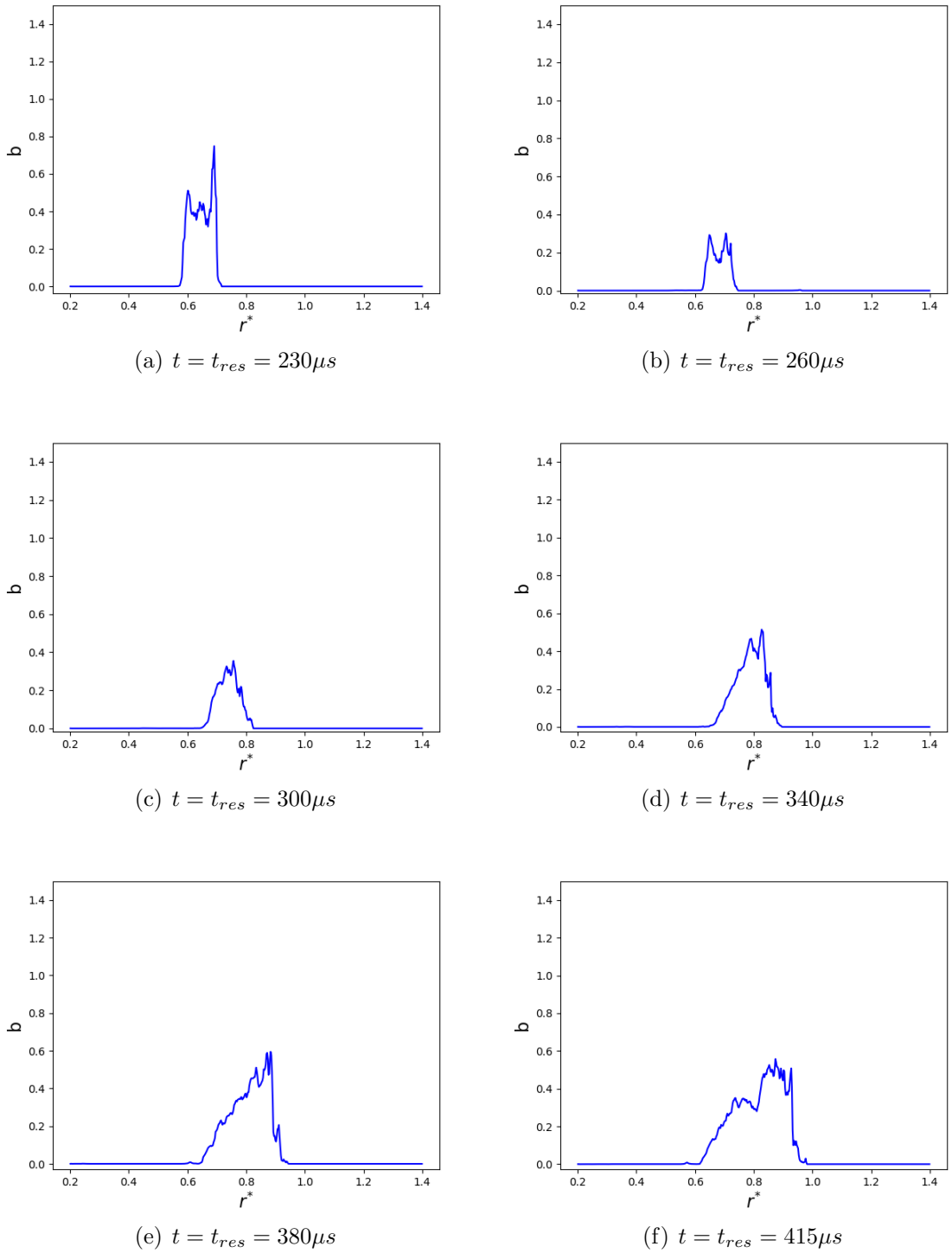

(a) $t = t_{res} = 230\mu s$

(b) $t = t_{res} = 260\mu s$

(c) $t = t_{res} = 300\mu s$

(d) $t = t_{res} = 340\mu s$

(e) $t = t_{res} = 380\mu s$

(f) $t = t_{res} = 415\mu s$

Figure 5.14: Density-specific volume correlation, a.k.a b parameter, during and after reshock for $a = 0.25mm$ and $k_1 = 16$, $k_2 = 64$

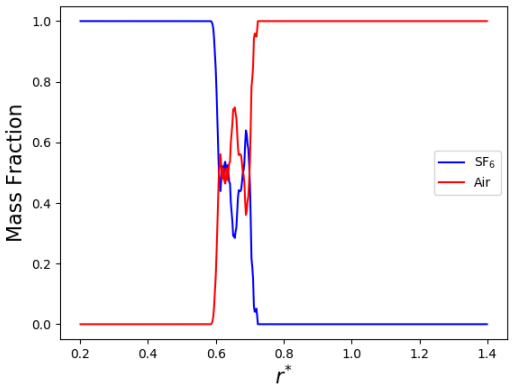

(a) $t = t_{res} = 230\mu s$

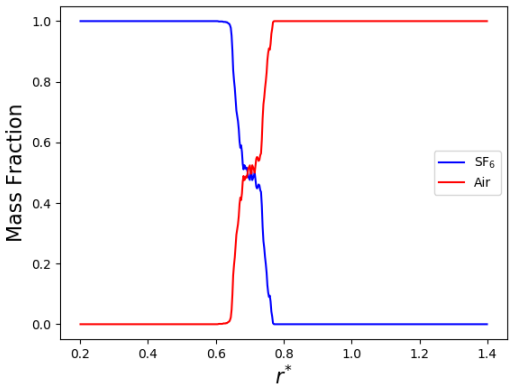

(b) $t = t_{res} = 260\mu s$

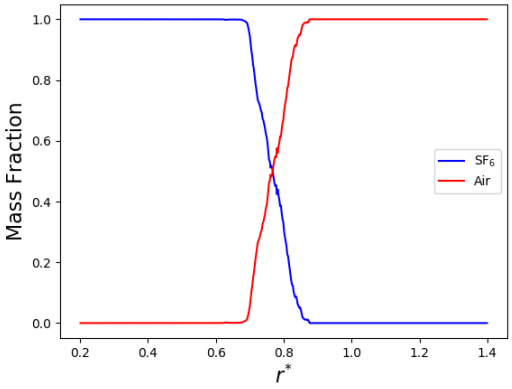

(c) $t = t_{res} = 300\mu s$

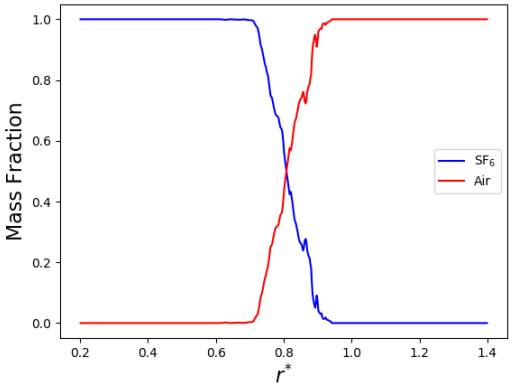

(d) $t = t_{res} = 340\mu s$

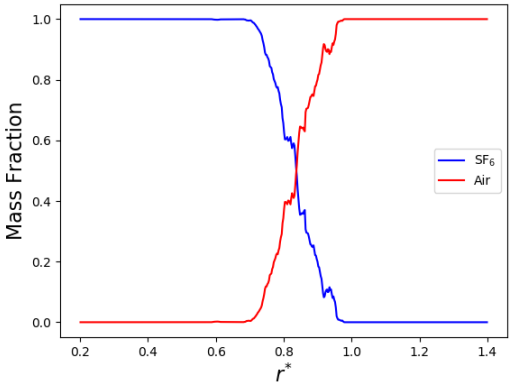

(e) $t = t_{res} = 380\mu s$

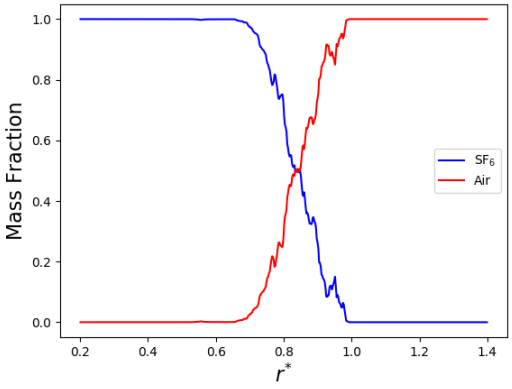

(f) $t = t_{res} = 415\mu s$

Figure 5.15: Mass fraction during and after reshock for $a = 0.25mm$ and $k_1 = 32$, $k_2 = 64$

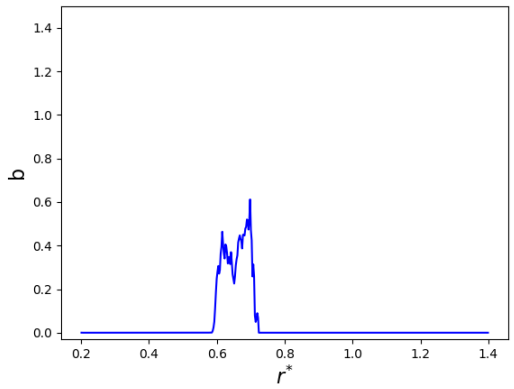

(a) $t = t_{res} = 230\mu s$

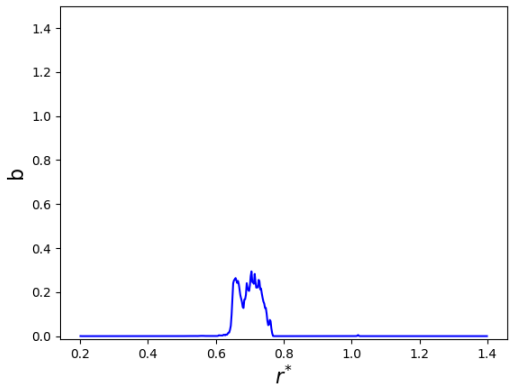

(b) $t = t_{res} = 260\mu s$

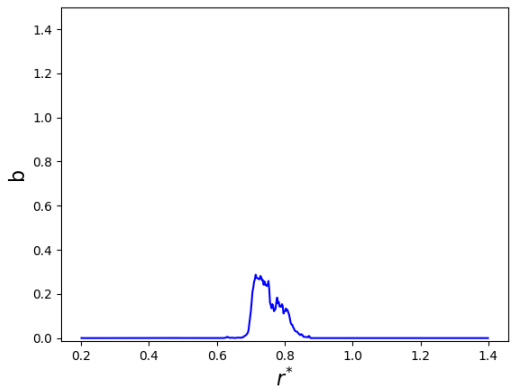

(c) $t = t_{res} = 300\mu s$

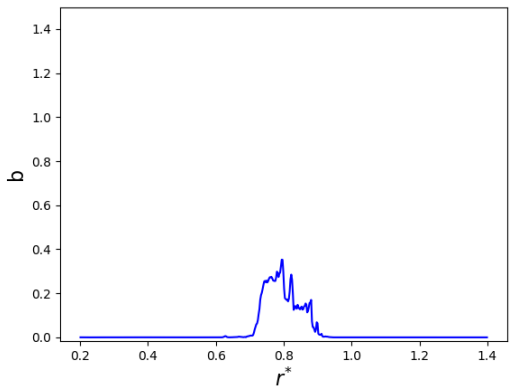

(d) $t = t_{res} = 340\mu s$

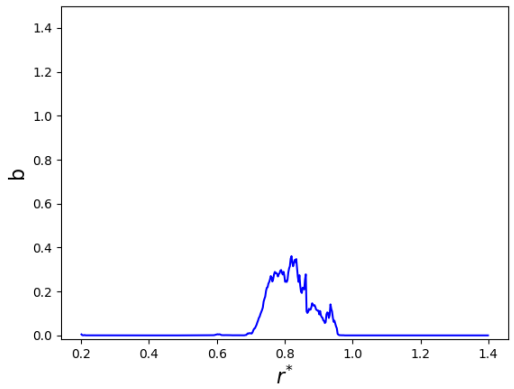

(e) $t = t_{res} = 380\mu s$

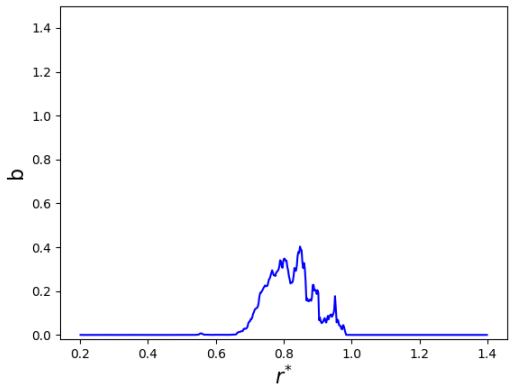

(f) $t = t_{res} = 415\mu s$

Figure 5.16: Density-specific volume correlation, a.k.a b parameter, during and after reshock for $a = 0.25mm$ and $k_1 = 32$, $k_2 = 64$

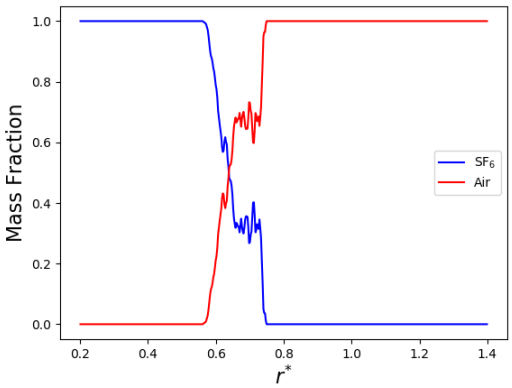

(a) $t = t_{res} = 230\mu s$

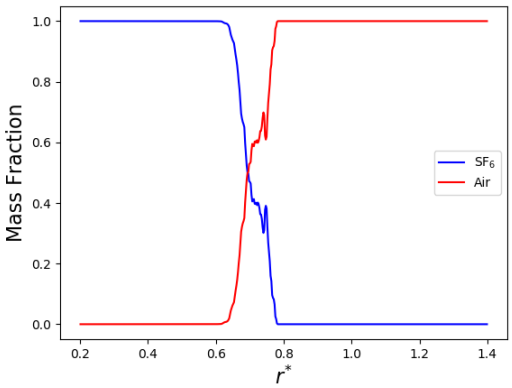

(b) $t = t_{res} = 260\mu s$

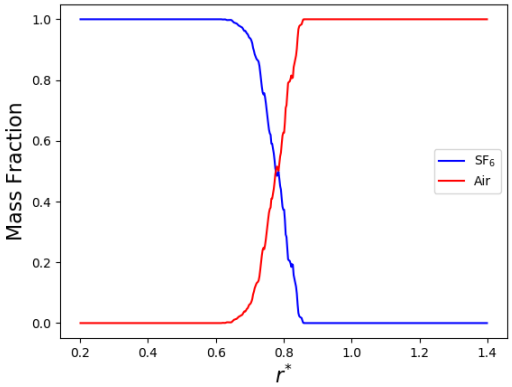

(c) $t = t_{res} = 300\mu s$

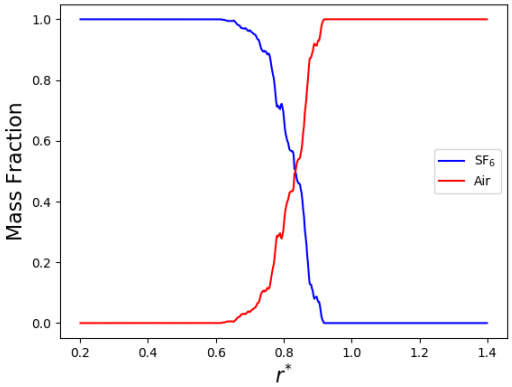

(d) $t = t_{res} = 340\mu s$

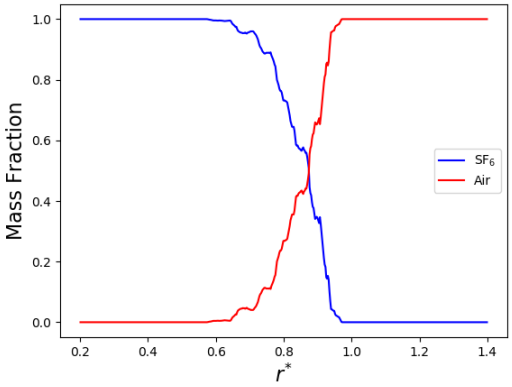

(e) $t = t_{res} = 380\mu s$

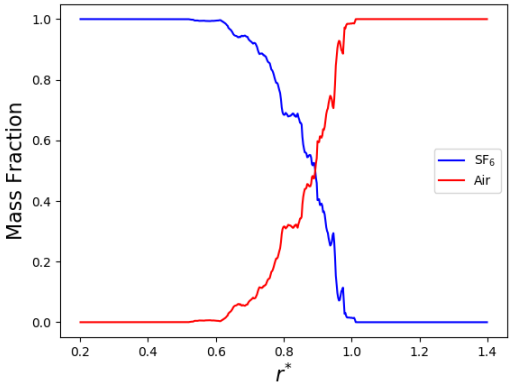

(f) $t = t_{res} = 415\mu s$

Figure 5.17: Mass fraction during and after reshock for $a = 0.25mm$ and $k_1 = 6$, $k_2 = 16$, $k_3 = 32$ and $k_4 = 64$

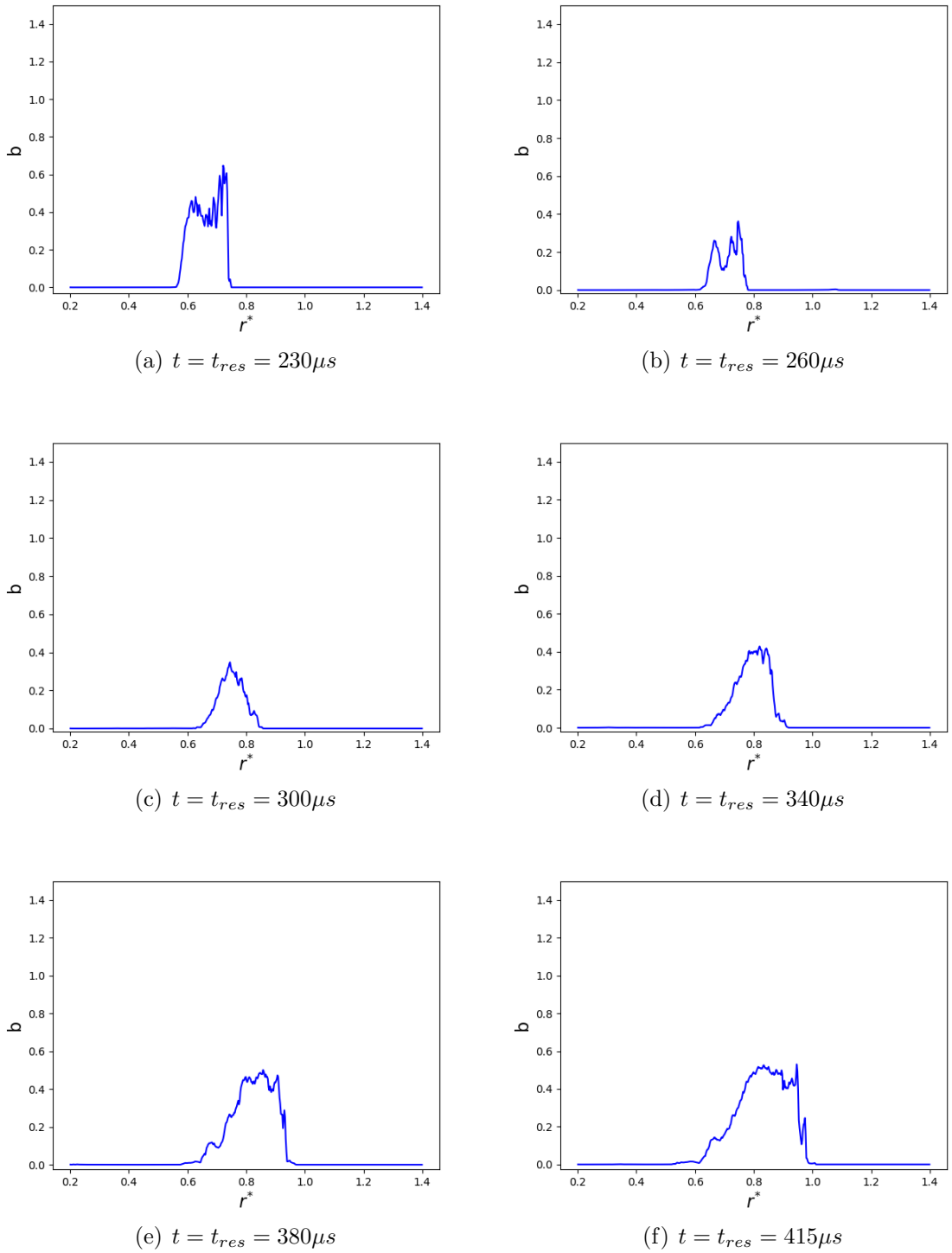

(a) $t = t_{res} = 230\mu s$

(b) $t = t_{res} = 260\mu s$

(c) $t = t_{res} = 300\mu s$

(d) $t = t_{res} = 340\mu s$

(e) $t = t_{res} = 380\mu s$

(f) $t = t_{res} = 415\mu s$

Figure 5.18: Density-specific volume correlation, a.k.a b parameter, during and after reshock for $a = 0.25mm$ and $k_1 = 6$, $k_2 = 16$, $k_3 = 32$ and $k_4 = 64$

Using an initially deterministic wave perturbation delivers a remarkable insight on the interaction of modes in a multimodal perturbation at late time.

The changes in wavelength or equivalently in wavenumber display more considerable effects in the late time mixing and interface evolution.

When the wavelength is long (equivalent to high wavenumber) and the modes wavenumber are close to each other e.g. $k = 6$ and $k = 16$ are close to each other, then the mixing region is well separated in terms of its species. This means that each species mass fraction will fluctuate near the vicinity of the average value of $\overline{Y_1} = \overline{Y_2} = 0.5$ at the mixing zone as depicted in figure 5.7. The fluids for long-wavelength perturbations are not well entrained due to the high separation between peaks and valleys and hence interaction between structures from one peak to another starts at very late time when the mixing layer possesses a very wide amplitude and non-linearities as the mixing region at late times is highly non-linear. This assertion is sustained by figure 5.8 which displays the mixing during and after reshock for the case with the highest wavelengths; the b parameter for this case is high demonstrating the low diffused interface hence low mixing is quantified by the density-specific volume correlation.

Now, let one of the wavelengths composing the interfacial perturbation to reduce or equivalently increase one of the wavenumbers $k_1 = 6$ and $k_2 = 32$. The immediate expectation is to enhance mixing due to the peak-to-peak distance decreasing. In this case, the interaction between different vortical structures evolving at each peak or valley of the wave starts earlier than the previous case. The mixing layer becomes more diffuse i.e. SF_6 has propagated in all directions in the air medium as depicted by figure 5.9. At late time after reshock, the mass fraction of each species shows a high deviation from the expected average of 0.5 when the interface is not very well mixed as in figures 5.9(d) - 5.9(f) for instance

(see also figures 5.7(c) - 5.7(b) for contrast). The highest concentration of SF_6 is located below the interface mean line while the contrary occurs for air. Mixing is indeed confirmed to be enhanced as displayed in figure 5.10 in which a smaller b parameter is obtained due to the mixing enhancement.

As one of the wavelengths is further reduced to obtain wavenumbers of $k_1 = 6$ and $k_2 = 64$, now the two modes comprehending the wave perturbation are separated by a high difference in wavenumber. Thus, as previously mixing enhancement is expected as well as a better entrainment between the mixture. This is confirmed in figure 5.11 which shows a well-distributed mass fraction radial profiles after reshock for both species as compared with figures 5.7 and 5.9. This is consequence of the earlier peak-to-peak interaction caused by the small separation between peaks. Thus, mixing is induced in a more chaotic manner in this case causing more mixing to be computed at the interface as demonstrated in figure 5.12 which displays low density-specific volume correlation meaning more mixing in comparison with figures 5.8 and 5.10 for the previous cases.

As before, now let the two wavenumbers of the perturbation to be less separated, keeping one of the waveumbers high at 64 while the other lower than that at 16. The concentration of the mixture zone is similar as the previous case just displaying the concentration of each gas to be a little bit higher near to its original origin as portrayed in figure 5.13 showing at late times a more discontinuous mass fraction distribution compared with the case of figure 5.11. This effect is caused by the domination of the long wavelength over the short wavelength after the reshock. Previous to reshock a very chaotic mixing zone is present due to the peak-to-peak initial distance and initial shock-interface interaction which

amplifies the growth of the high frequency. The reshock amplifies the low frequency (or long wavelength) modes. This modes of the perturbation are closer than before compared to case m.III in terms of their wavenumbers.

At late times after reshocking the interface, the long-wavelengths (low-wavenumber) modes dominate over the short-wavelengths (high-wavenumber) modes in the perturbation spectrum in terms of the radial growth of the interface as after reshock the low-wavenumber is amplified and RMI is experienced mainly by this mode as the higher-wavenumber mode experiences a mixing enhancement. The previously-mentioned feature is observed clearly when the two wavenumbers of the initial perturbation are separated for each other as in the case of $k_1 = 6$ and $k_2 = 64$. In figure 5.6(c), the low-wavenumber mode $k_1 = 6$ is noticeable in the mixing layer as it drives the mixing layer growth while the high-wavenumber mode $k_2 = 64$ drives mixing. This is most noticeable in figure 5.5(c) in which after $t_{reshock} \approx 240\mu s$, the interface width corresponding to the multimode initial perturbation is below the interface width for the single mode case of the high-wavenumber. In contrast, at initial times, the high-wavenumber modes drive the RM instability and its initial mixing zone as depicted in all subfigures in figure 5.5. Thus, reshocking the interface not only causes an initial RT stabilization effect but also an amplification of the low frequency modes displaying a new primary RM instability while enhancing the growth of the previous. This finding is sustained by the stability of the shock wave. Initially as the main shock wave bifurcates at the initial shock-interface interaction, the convergent transmitted shock wave and the divergent refracted shock wave shapes as the initial perturbation at the interface but as they travel inwards for the convergent shock

wave and outwards for the divergent shock wave, the tendency of the waves are to retake its original cylindrical or spherical shape as they become stronger or weaker. Nonetheless, as the convergent shock wave auto-focuses at the convergence center it amplifies its strength. At reshock, the RM instability is taking place in the high frequency mode but the stronger divergent shock wave tend to amplify the low frequency mode as it is driving the mean shape of the reshocked interface and then the RM instability is observed for the long wavelength mode while the previous primary RM instability is, after reshock, a secondary instability. Hence, the RT instability is driven by the low frequency modes while the high frequency modes present secondary instabilities at late times.

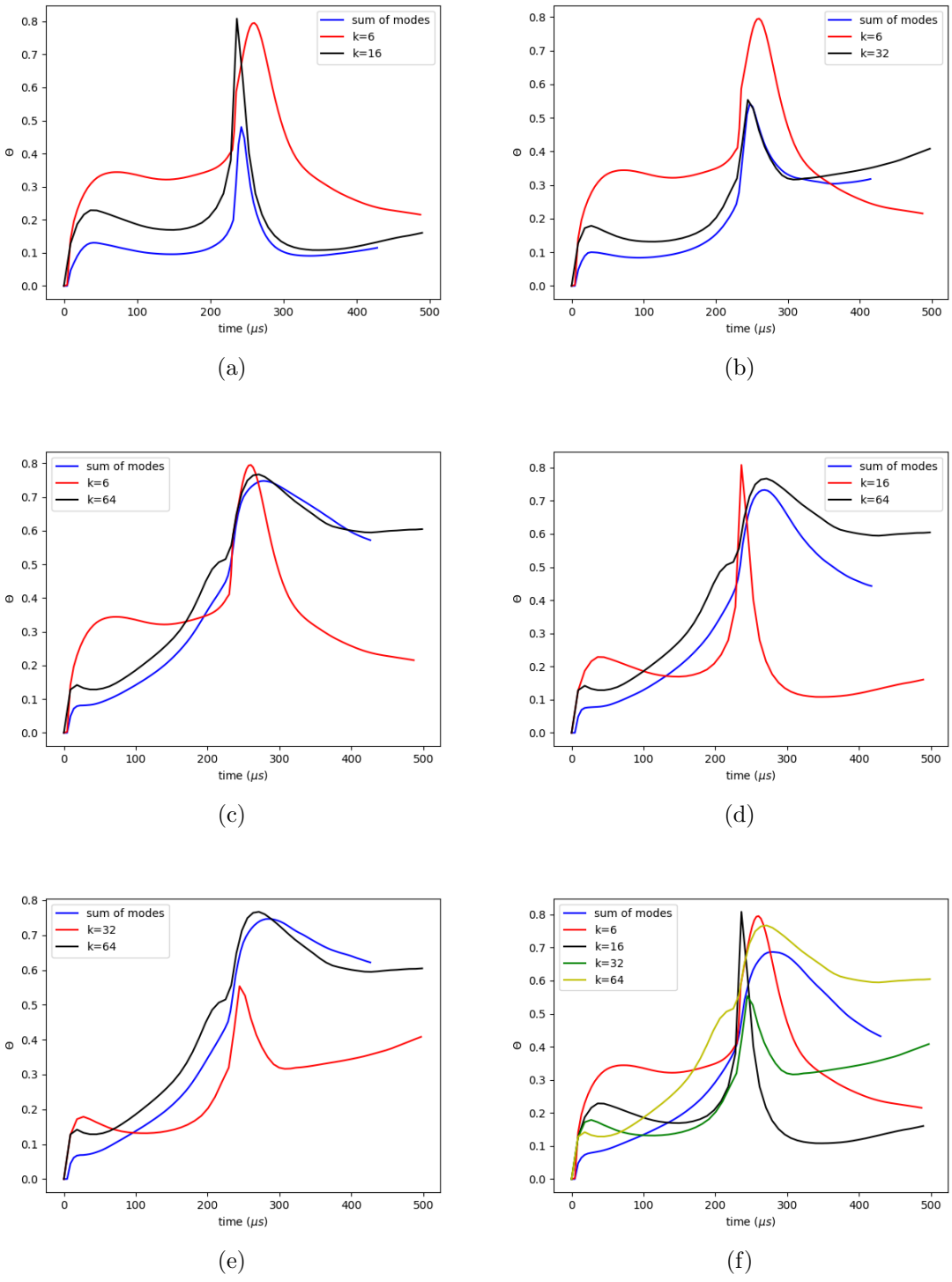

(a) (b)

(c) (d)

(e) (f)

Figure 5.19: Mixing fraction for each multimode case and the single mode cases for ease of comparison and depiction of dominant mode.

To estimate the level of molecular mixing of the interface separating two fluids, Youngs provided a ratio of the amount of "chemical reaction" to the actual

amount to be proportional to the products $\overline{Y_1} \cdot \overline{Y_2}$ and $\overline{Y_1 \cdot Y_2}$ respectively for two different species mass fraction(Youngs, 1991, 1994).

$$\theta\left(x\right) = \frac{\overline{Y_1 \cdot Y_2}}{\overline{Y_1} \cdot \overline{Y_2}} \tag{5.3}$$

Nevertheless, the quantity in equation describes molecular mixing in one plane only. The interest is in the overall mixing layer or turbulent mixing zone for which the integral quantity of equation 5.3 is computed as described by Youngs for turbulent mixing triggered by RT and RM instabilities.

$$\Theta\left(t\right) = \frac{\int_{x_u}^{x_l} \overline{Y_1 \cdot Y_2} dx}{\int_{x_u}^{x_l} \overline{Y_1} \cdot \overline{Y_2} dx} \tag{5.4}$$

In equation 5.4 the limits x_l and x_u are the lower and upper limits of the extent of the mixing zone in the plane x. Knowing that for a mixture consisting of two species the mass fraction of the species is related as $Y_2 = 1 - Y_1$; this drives equation 5.4 to

$$\Theta\left(t\right) \frac{\int_{x_u}^{x_l} \overline{Y_1 \cdot (1 - Y_1)} dx}{\int_{x_u}^{x_l} \overline{Y_1} \cdot \overline{1 - Y_1} dx} \tag{5.5}$$

Equation 5.5 can then be computed by using numerical integration techniques in order to obtain the degree of molecular mixing as a function of the simulated time. Notice that equation 5.5 is integrated linearly along an axial axis. For the cases under consideration in this work, the planes are concave and thus the molecular mixing needs to be integrated radially as

$$\Theta\left(t\right) \frac{\int_{r_i}^{r_o} \overline{Y_1 \cdot (1 - Y_1)} dr}{\int_{r_i}^{r_o} \overline{Y_1} \cdot \overline{1 - Y_1} dr} \tag{5.6}$$

where the limits of integration r_i and r_o are the most inner and outer radial locations of the mixing layer in a cylindrical or spherical framework. Equation

5.6 is the definitive equation solved using the trapezoidal numerical integration technique at each radial location for each time step output.

Figure 5.19 shows the results obtained from equation 5.6 for all the cases under consideration. Each multimode interface is accompanied by its single mode components in order to properly differentiate the effects of each mode in the molecular mixing development.

The molecular mixing at late times after reshock is clearly affected by the initial conditions of the initial interface perturbation. Concisely, it is demonstrated in figures 5.19(a) - 5.19(f) that depending on the initial wavelength, or equivalently wavenumber, the late time molecular mixing of a multimode interface is highly characterized for its shortest wavelength or highest wavenumber. For instance, observe figure 5.19(a), the late time molecular mixing after reshock is dominated by its highest mode even though both modes are of high wavelength; nonetheless, the highest mode is the dominant at late time. This feature is also confirmed in figure5.19(b) in which reducing the wavelength has caused a clear dominance of the highest wavenumber mode to dominate over all the simulated time as the molecular mixing of the multimode interface is closely equivalent to the molecular mixing of its single mode interface of the highest wavenumber. This happen in all of the multimode cases of figure 5.6; the molecular mixing before and after reshock are closely similar to the molecular mixing of its highest wavenumber single mode contribution. Having several modes as in figure 5.19(f) also shows the same result regarding the highest wavenumber mode but with more deviation than from its single mode interface component than the other cases analyzed corresponding to only two modes. Observe that

if the modes are well separated, the almost complete dominance of the highest wavenumber single mode component is accentuated as shown in figures 5.19(c) - 5.19(e). Thus, confirming the previous finding that high-wavenumber modes drive mixing at late times while low-wavenumber modes drive the interface radial evolution.

5.1.2 Amplitude Effects

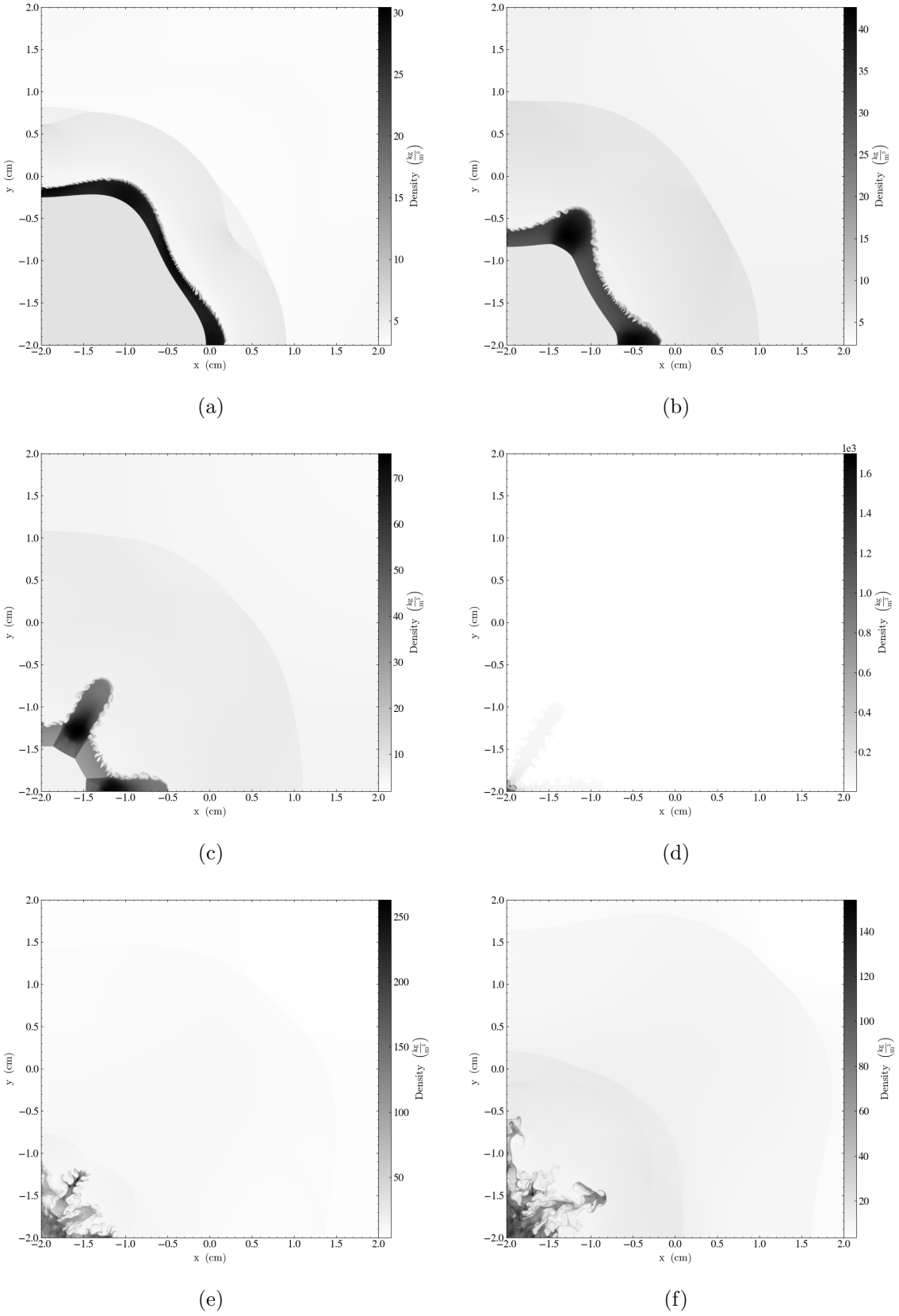

Figure 5.20: Density field for several times for $a = 2mm$ and $k = 6$

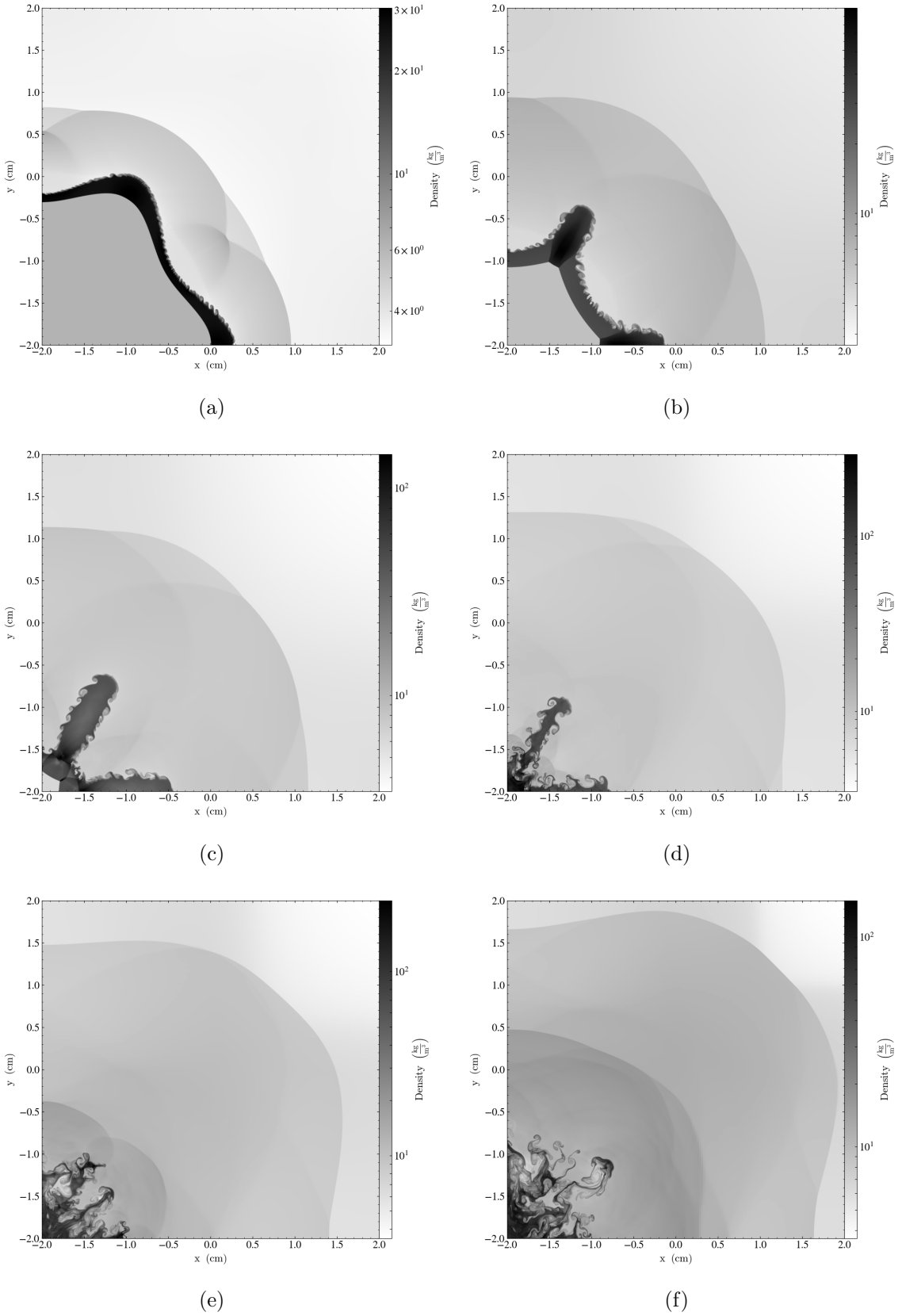

Figure 5.21: Density field for several times for $a = 3mm$ and $k = 6$

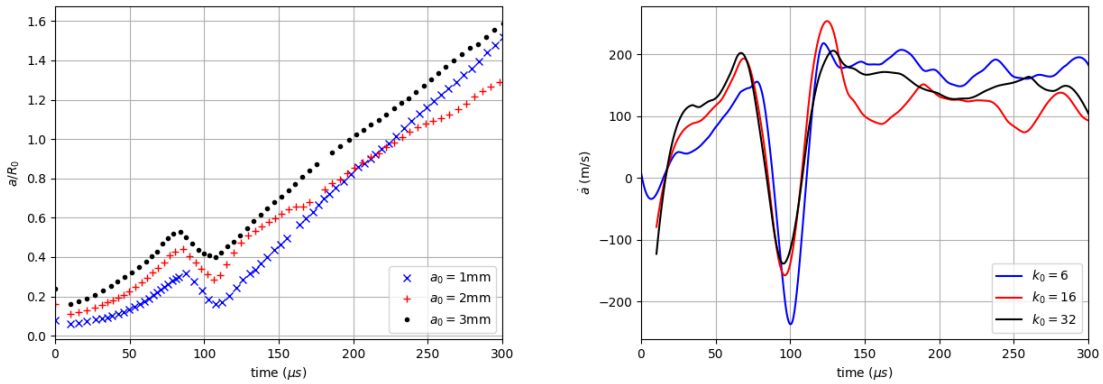

(a) (b)

Figure 5.22: Mixing layer amplitude development for three different initial amplitudes. The initial wavenumber is kept constant as $k = 6$. The plots correspond to a) the width or amplitude of the mixing layer and b) the mixing layer growth rate.

Three different amplitudes are analyzed ,namely, $a = 1$mm, $a = 2$mm and $a = 3$mm with constant wavenumber $k = 6$ and $a_0/\lambda = 0.0382$, 0.0764, and 0.1145 respectively. The amplitude growth of the mixing layer is non-dimensionalized by the initial radius of the cylindrical target for a case of constant wavenumber $k = 6$. Initially, no significant contrasts exist between the three cases as depicted in Figure 5.22.

As expected, the mixing layer is wider as the amplitude of the initial perturbation wave is augmented. Similarly after reshock, the interface with the highest amplitude exhibits the widest mixing layer as well as the higher growth rate. At $t = 215\mu$s, the low-amplitude case ($a = 1$mm) surpasses the medium amplitude case by delivering a wider mixing layer. Hence, after reshock, the low-amplitude case displays the highest growth rate which is quasi-constant as stated previously because of the low wavenumber. Moreover, the high growth rate of the low-amplitude case result in a surpassing also with respect of the highest amplitude case ($a = 3$mm). Therefore, at late times the lowest amplitude case is

expected to exhibit the widest mixing layer but more simulation time and a bigger computational domain is necessary to confirm this.

The explanation for this phenomena may be found in the secondary KH instability present. Secondary instabilities tend to saturate the evolution of turbulent mixing layers due to their dissipative nature. In our cases of study in this work, the KH instability is present causing a necking in the mushroom-like structures of the RM and RT instability. As advection takes place, the interaction of scales start to become wider and KH effects become considerable. Due to high amplitude of the initial wave, shear effects start early and as a consequence the interaction between fluid vortical structures start swifter than for the lower amplitude cases ergo saturating the growth rate in a lower value. This ansatz suggests that for a higher initial amplitude of the perturbation wave, the late-time growth rate saturates in a lower value causing a wider mixing layer at late times for the low-amplitude case.

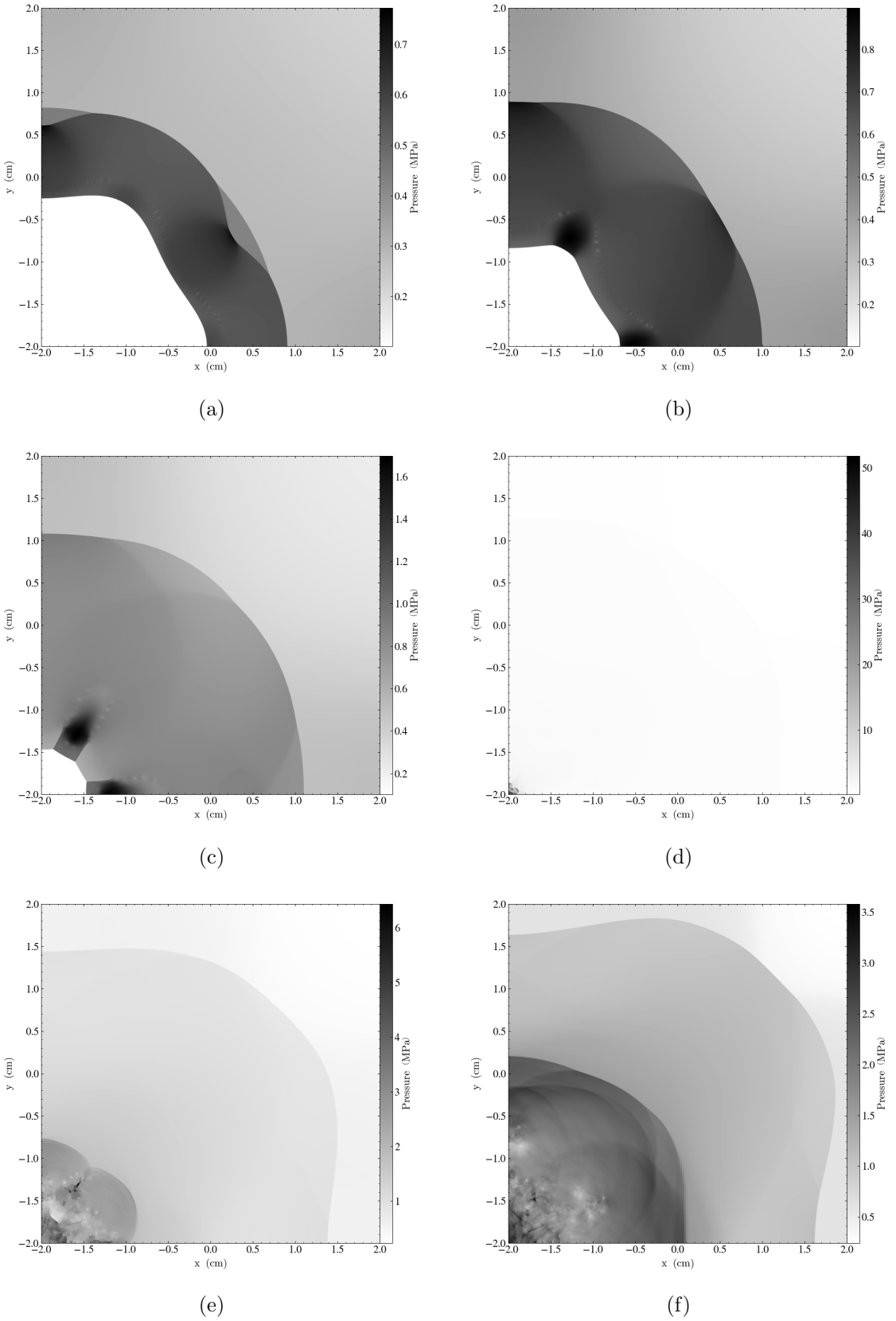

Figure 5.23: Pressure field for several times for $a = 2mm$ and $k = 6$

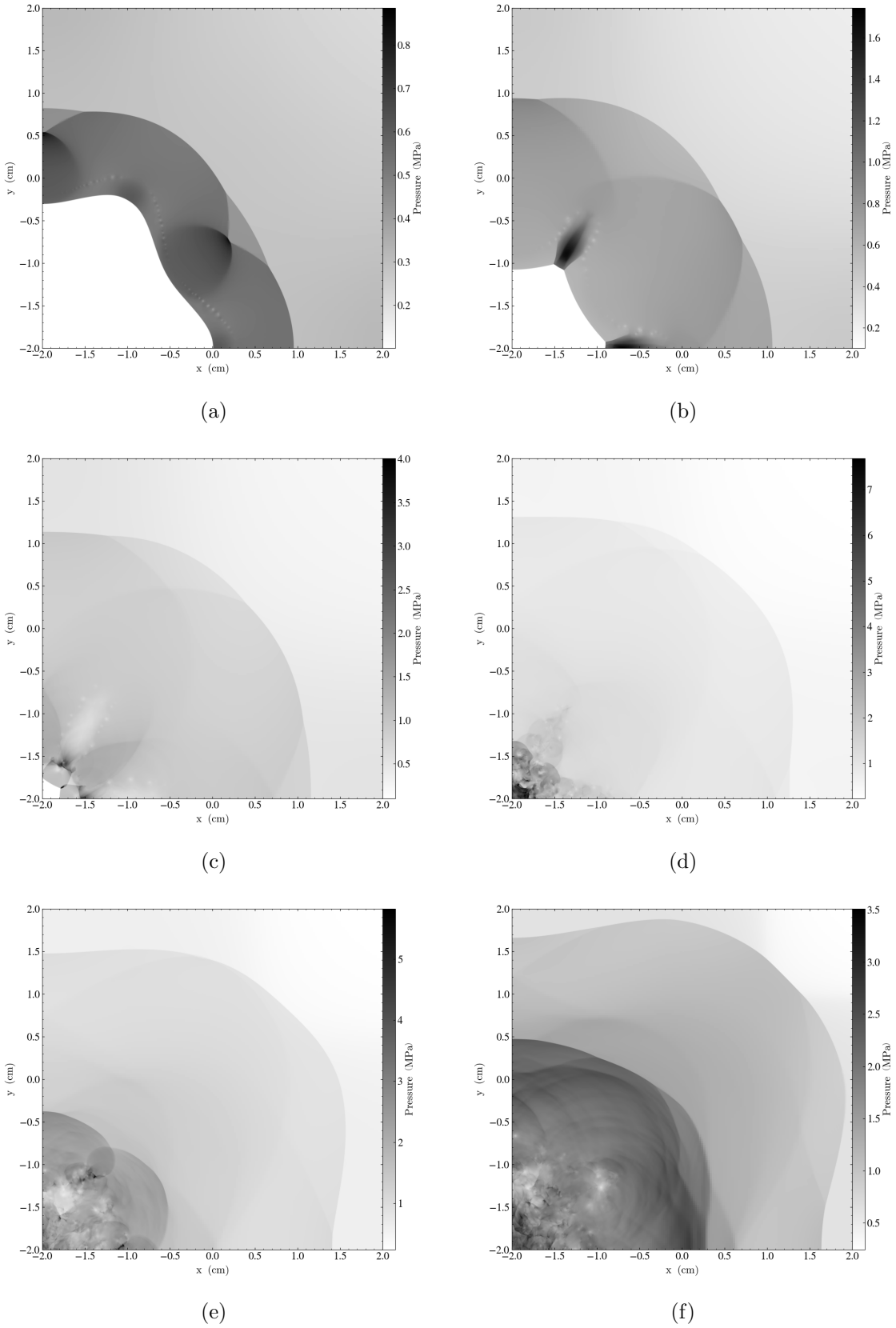

Figure 5.24: Pressure field for several times for $a = 3mm$ and $k = 6$.

The shock dynamics of these cases are observed in figures 5.23, 5.24. Observe that after the shock initially bifurcates into a transmitted shock and a reflected shock, both shocks shape as the initial amplitude with the divergent shock displaying an amplification in shock front amplitude as shown in figures 5.23(a), 5.24(a), As the transmitted shock and reflected shock travel inwards and outwards respectively, the peaks and valleys of the wave-like shock start to form a polygonal converging shock wave and a curvilinear divergent shock wave as depicted in figures 5.23(b), 5.23(b). As the transmitted shock moves toward the convergence center, the polygonal shock wave is more accentuated and also show a Mach stem for the case of high amplitude as depicted in figures 5.23(c), 5.24(c).

An interesting effect on perturbation amplitude is found at this stage as the initially convergent cylindrical shock wave has become into a strong polygonal shock wave. It has been demonstrated that a convergent shock wave is always unstable (Takayama, Kleine, & Grönig, 1987) but its polyginal counterpart behaves in a stable manner as it converges and just showing an angular shift(Schwendeman & Whitham, 1987); Hence, the main effect of a high amplitude is to transmit an stable polygonal shock wave instead of an unstable cylindrical shock. The moment of shock auto-reflection at the convergence center is shown in figures 5.23(d), 5.24(d). There, it is observed a shock strength of approximately 50 times the initial pressure. Thus, the convergent shock wave, whether cylindrical (spherical) or polygonal, becomes a strong divergent shock wave compared with the initial shock wave that hits the interface at time $t = 0$. Reshock happens at figures 5.23(e), 5.24(e). It is observed a complex wave pat-

tern as the interface is very chaotic at reshock and shock bifurcation is a highly non-linear phenomena at this stage.

At late times, complex wave interactions happen inside the SF_6 target in also traveling outside the domain as shown in figures 5.23(f), 5.24(f). Due to the increasing strength of the auto-reflected transmitted shock wave, a high interface width and growth rate is obtained at and after reshocking the interface. Therefore, the main effect of a high amplitude perturbation is in the stability of the shock wave as increasing the amplitude of the initial wave perturbation gives a convergent polygonal shock wave which is of stable nature.

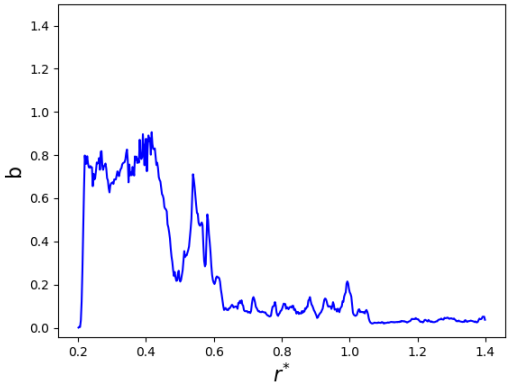

(a)

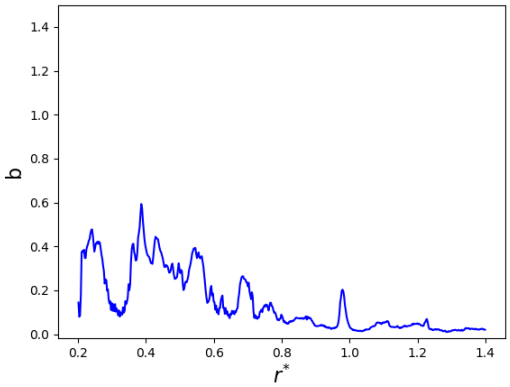

(b)

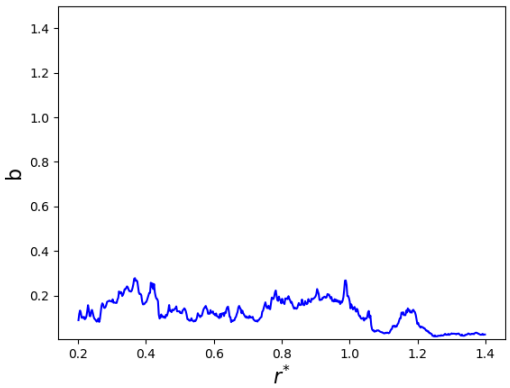

(c)

Figure 5.25: b mixing correlation for the case of contans wavelenght and variable amplitude perturbations at final times.5.25(a) corresponds to $a = 1mm$, 5.25(b) corresponds for $a = 2mm$ and 5.25(c) shows the density-specific volume correlation for $a = 3mm$.

In terms of mixing effects due to the increase in the initial amplitude of the perturbation, the relation found is a proportional relation between the initial

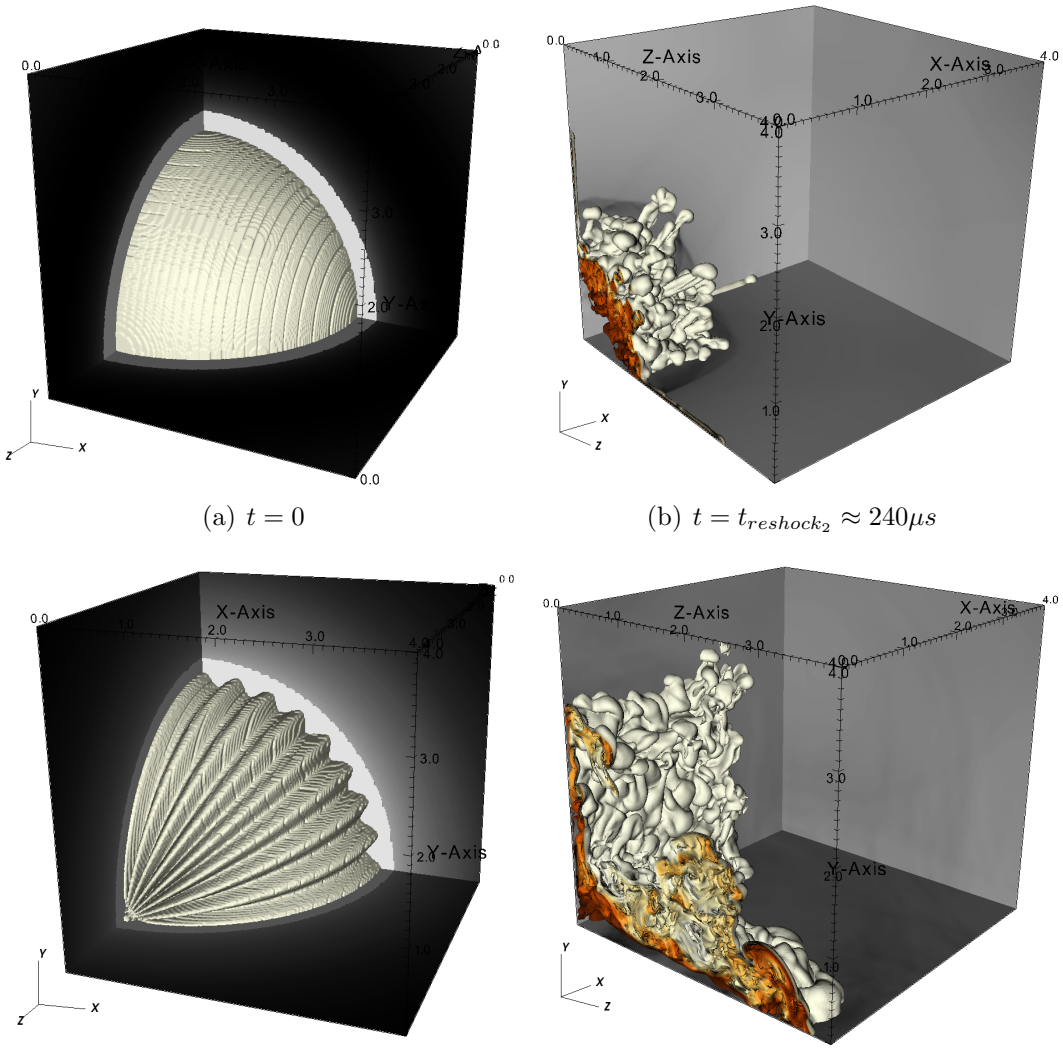

(a) $t = 0$ (b) $t = t_{reshock_2} \approx 240\mu s$

(c) $t = 0$ (d) $t == t_{reshock_2} \approx 240\mu s$

Figure 5.26: Spherical frames with mass fraction contours showing the mixing layer and pressure surfaces showing the waves. a) and b) correspond to the initially unperturbed case while c) and d) belongs to the perturbed case.

amplitude and the mixing quantified by the density-specific volume correlation. As depicted in figure 5.25, keeping in mind that a high b value means low molecular mixing, increasing the amplitude presents a proportional relation to the late-time mixing as a high amplitude delivers a low b value which portrays more mixing.

5.2 Spherical Simulation

In contrast to the previous results presented, considering the full geometry of the problem present real turbulence due to the addition of vortex stretching which was zero in two dimensions. Hence, quantitatively the mixing layer width must be different than in 2D. The perturbation becomes more challenging to implement in spherical coordinates as the need of spherical harmonics augments the difficulty of modeling the interfacial perturbation.

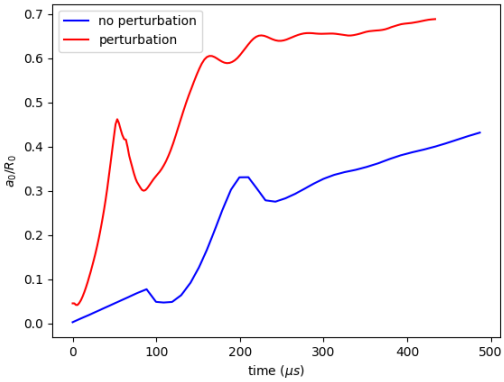

Figure 5.27: Mixing layer width of a 3D simulation for similar Mach number with only a Cartesian grid-induced step-like perturbation

Notice from figure 5.27 the mixing layer width in comparison with the mixing layer widths of the two-dimensional cases previously presented as the interface and shock movement is faster and the mixing layer width development saturation is shown at late times. In three dimensions, even the physics of the shock is different i.e. the shock traveling path differs as it is observed that reshock occurs at an earlier time than in a 2D case i.e. $t_{reshock_{3D}} \approx 0.54 t_{reshock_{2D}}$. Hence, two reshock process are captured since the reflected expansion fan when autofocused at the convergence center become a divergent shock wave for a second reshock process and after that no more shock waves hit the density interface.

Two cases are analyzed for an unperturbed case and a perturbed case with a high amplitude and moderate wavenumber of $k = 32$. It is observed that the perturbed case presents always the widest mixing layer compared to an unperturbed case as it is shown in figure 5.27. The perturbed case displays a perfect linear growth (constant slope or growth rate) initially before reshock contrary to the perturbed case. After reshock, nonlinear features are amplified and the unperturbed case displays high growth in the mixing layer but the perturbed case always leads the growth. A second reshock happens and settles the growth rate as similar slopes are observed in figure 5.27 at late times.

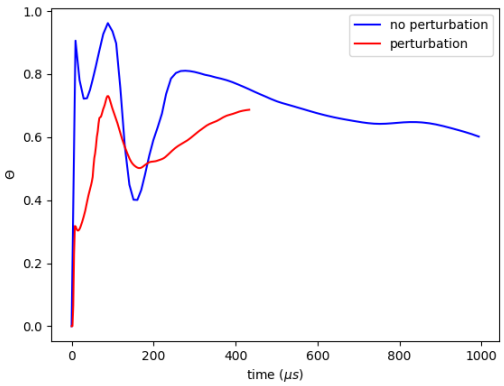

Figure 5.28: Molecular mixing fraction for unperturbed and perturbed cases.

The mixing for the spherical cases is quantified by the molecular mixing fraction Θ evolution in time as depicted in figure 5.28. It is observed an initial highly-mixed interface for the unperturbed case before reshock occurs. This might be caused by the initial perturbation inherently induced by the grid resolution. In 3D, the maximum resolution considered is of a Cartesian structured grid of size $256 \times 256 \times 256$ due to the constraint in computational power available at hand. This high mixing before reshock goes in accordance to the 2D simulations in which low-wavenumber perturbations display high mixing ini-

tially; hence, the grid-induced mixing resembles to a low-wavenumber perturbation due to the low resolution grid generated. Thus, the perturbed case being initialized with a wavenumber of $k = 32$ and a high amplitude displays less mixing due to the initial high wavenumber as in the 2D cases before reshock. After reshock, the unperturbed case still displays more mixing but it starts to be reduced whereas the perturbed case displays a mixing enhancement. Eventually at late times, it is expected to have a more mixed interface for the perturbed case compared to the unperturbed case similar as in 2D cases where high-wavenumber perturbation modes dominate the late time mixing. Such expectation is based on figure 5.28 in which the molecular mixing fraction of the perturbed case increases at late time while the unperturbed case displays a diminishing in molecular mixing; nonetheless, more simulation time is required for confirming such conjecture.

5.3 Proper Orthogonal Decomposition

The POD achieves an order reduction by decomposing the data into modes and projecting such modes into a different orthogonal space. This decomposition is applied to the fluctuations of the dynamic and thermodynamic quantities. Specifically, the POD is applied to the state vector $\mathbf{q}$ composed by the following fluctuating flow variables: $\mathbf{q} = (\rho', u', v', T')$ with ρ' being the density fluctuations, u' & v' the horizontal and vertical components of the velocity field and T' the temperature fluctuations; this state vector is choosen as the inner product considered is the inner product devised by Yang and Fu(Yang & Fu, 2008) presented in equation 3.5. The fluctuations are computed by using the Favre averages $\tilde{\mathbf{q}}(\mathbf{x}, t)$ from equation 3.7. Once that the average flow is computed, then

it is subtracted from the flow field in order to obtain the fluctuations $\mathbf{q}''(\mathbf{x}, t)$ as described in equation 3.6. From these fluctuations the POD can be properly applied.

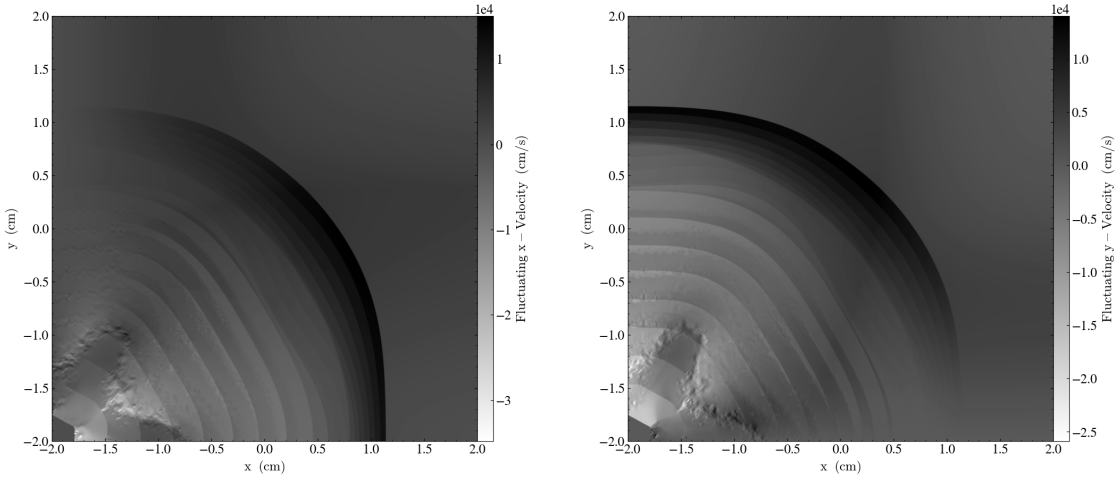

(a) (b)

Figure 5.29: Fluctuating velocity components for a 2-dimensional case. These fluctuations were computed after substracting the mean flow (computed with Favre averaging) to the original flow.

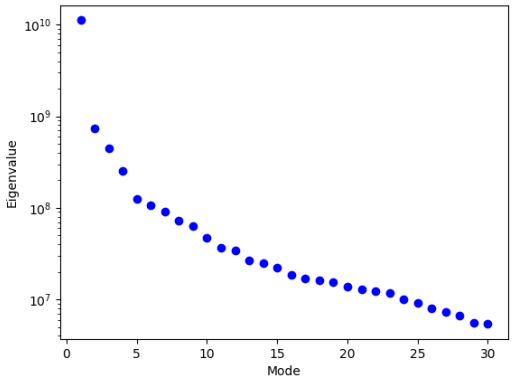

Figure 5.30: Eigenvalues obtained from the SVD applied to the flow. Each eigenvalue represents the total amount of energy captured by each POD mode.

Figure 5.29 shows the velocity fluctuations captured before performing the POD analysis to the flow by computing Favre averages and extracting them from the original data output provided by the FLASH simulations. It is observed that for these cases the fluctuating velocities are high with respect to the

mean flow as the order of magnitude is similar than the mean flow, i.e. $\mathbf{v}' \sim 10^4 cm \cdot s^{-1}$ and $\overline{\mathbf{v}} \sim 10^4 cm \cdot s^{-1}$. This result suggests that the velocity fluctuations contribute with as much energy as the mean flow in this type of flow system. This is caused by the addition of more baroclinic vorticity at the interface at reshock; hence, after reshock more energy is deposited at the mixing zone but such energy is more noticeable at the fluctuating quantities rather than in the mean flow.

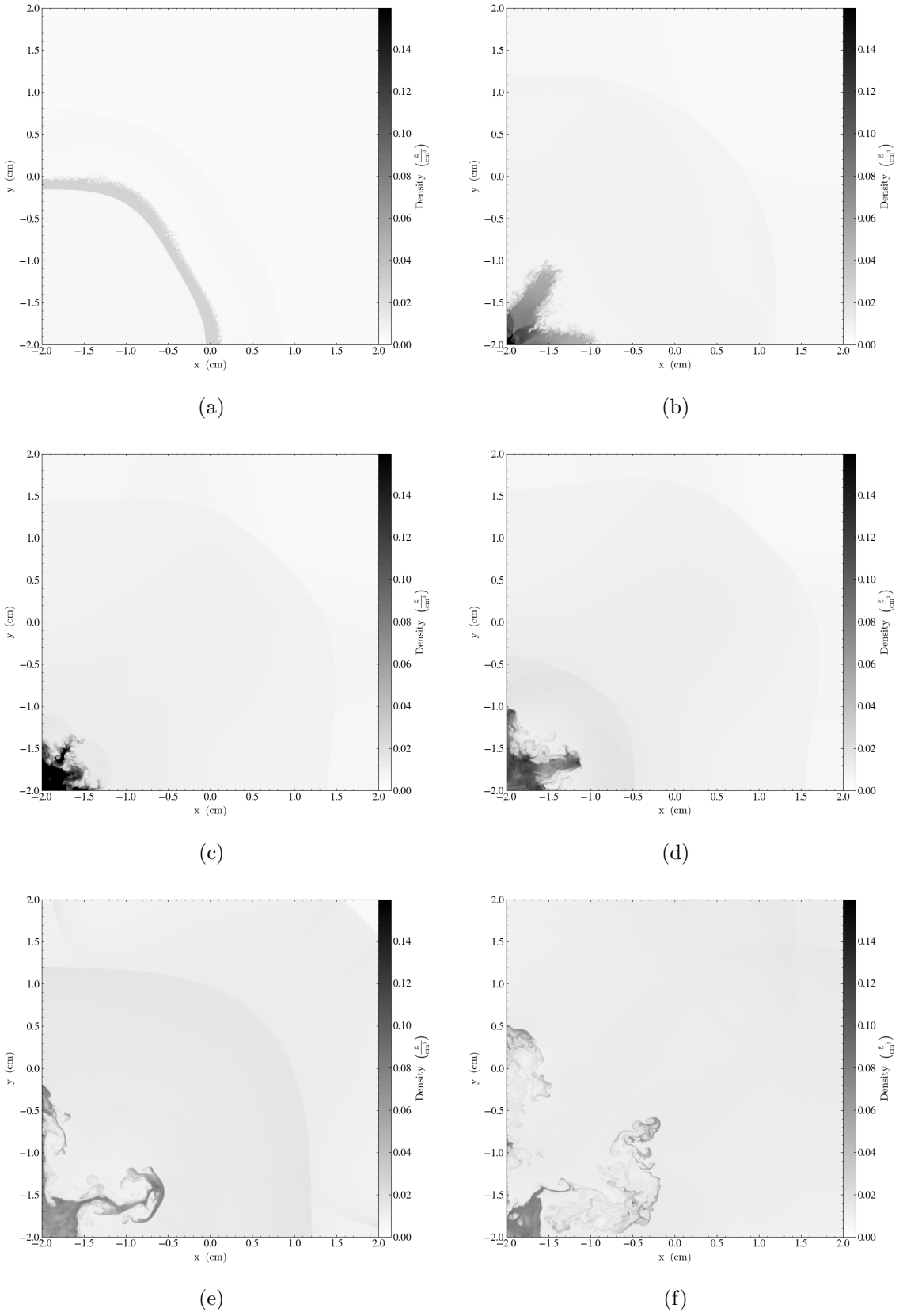

Figure 5.31: Total Density field of the original simulation data at several times.

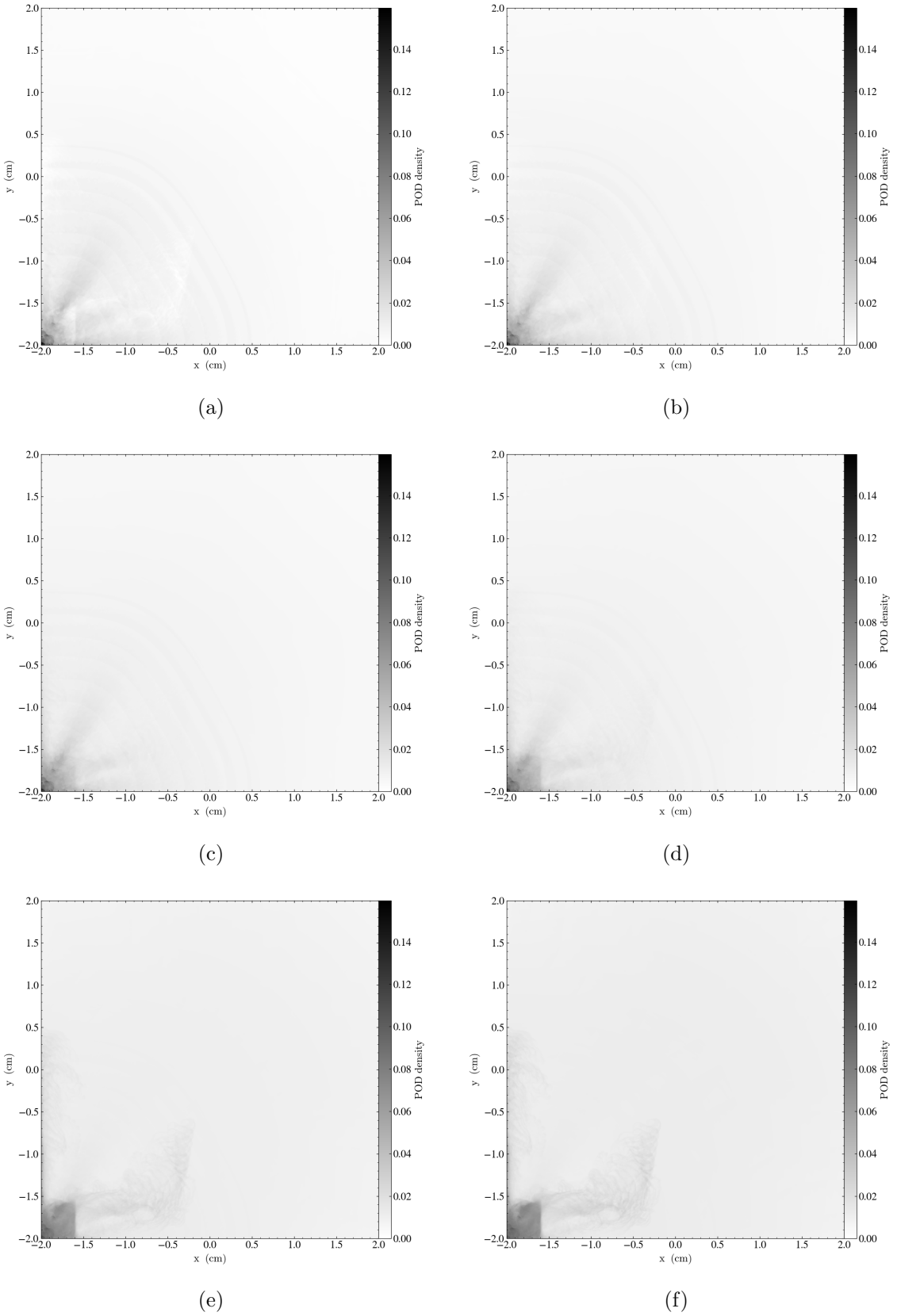

Figure 5.32: Total Density field reconstruction using the 1st mode after performing the POD to the simulation data at several times.

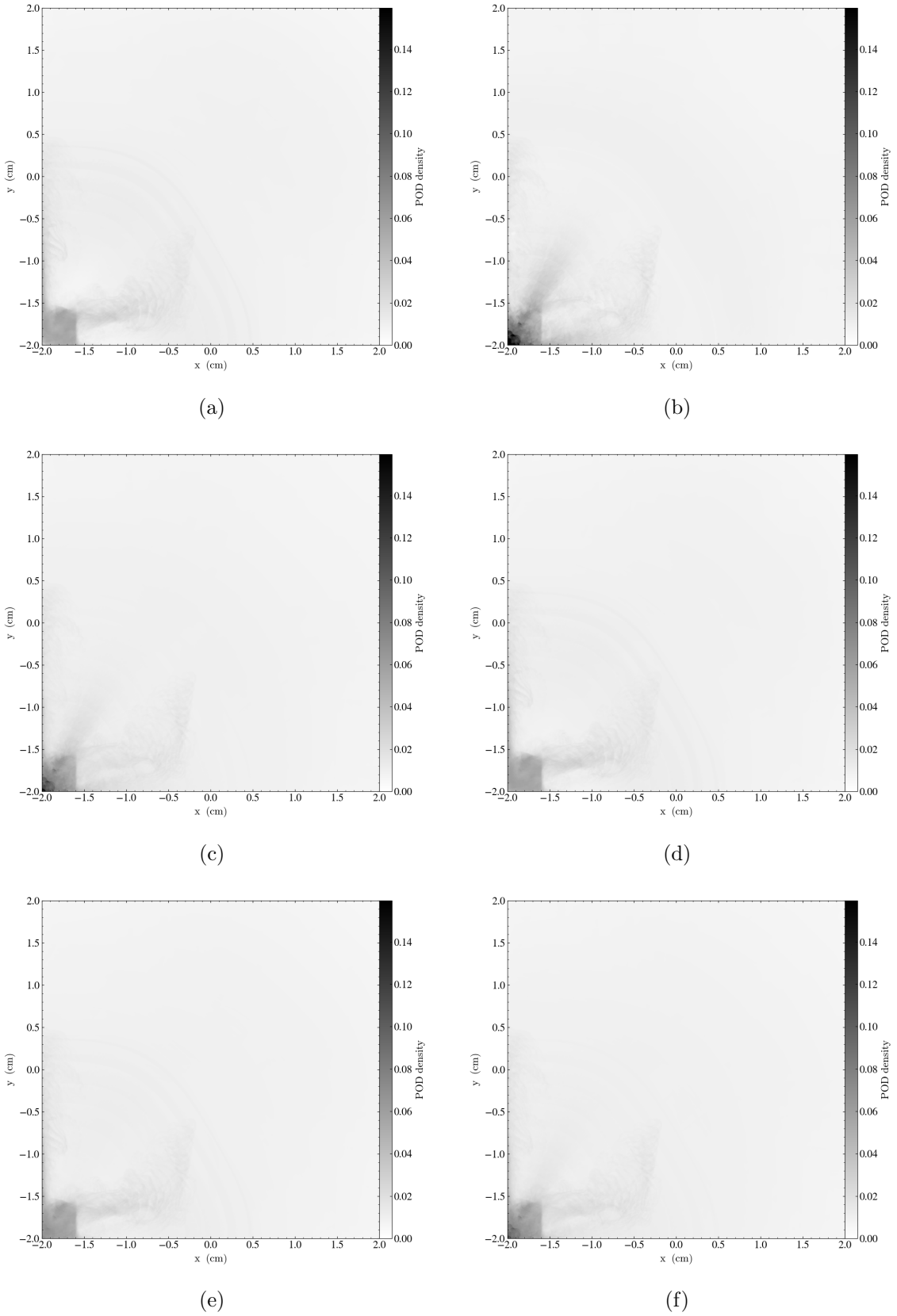

Figure 5.33: Total Density field reconstruction using the 2nd mode after performing the POD to the simulation data at several times.

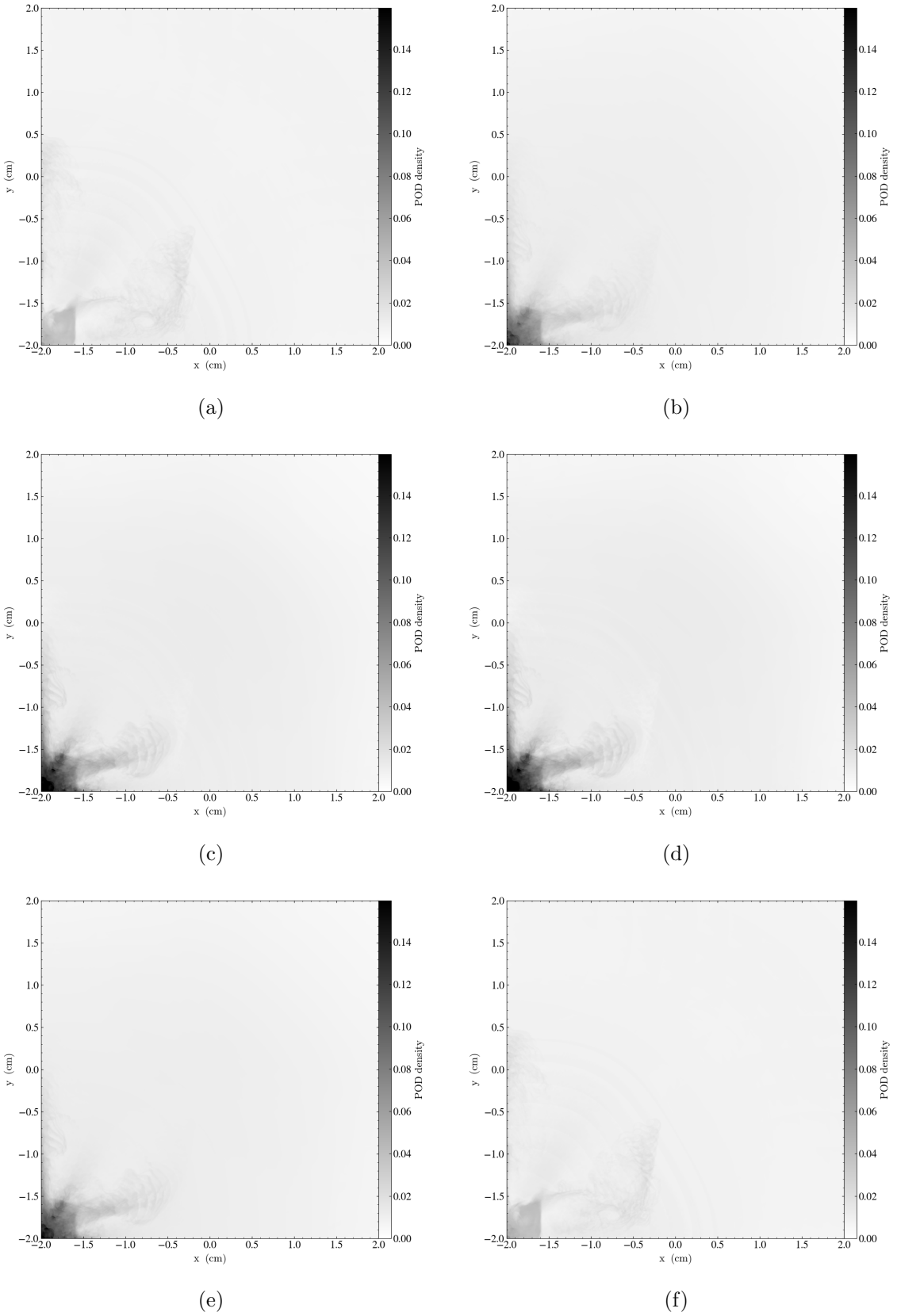

Figure 5.34: Total Density field reconstruction using the 3rd mode after performing the POD to the simulation data at several times.

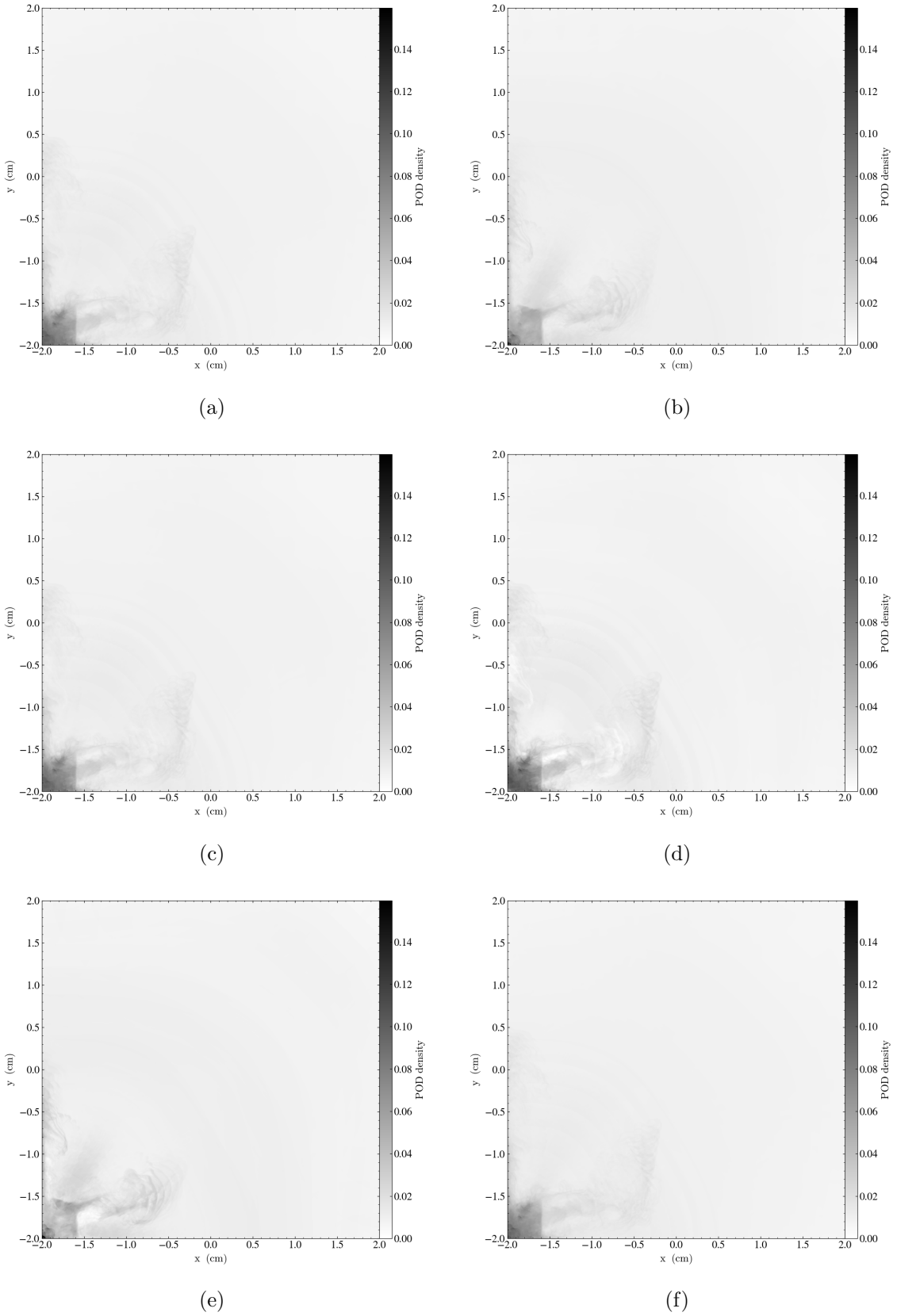

Figure 5.35: Total Density field reconstruction using the 4th mode after performing the POD to the simulation data at several times.

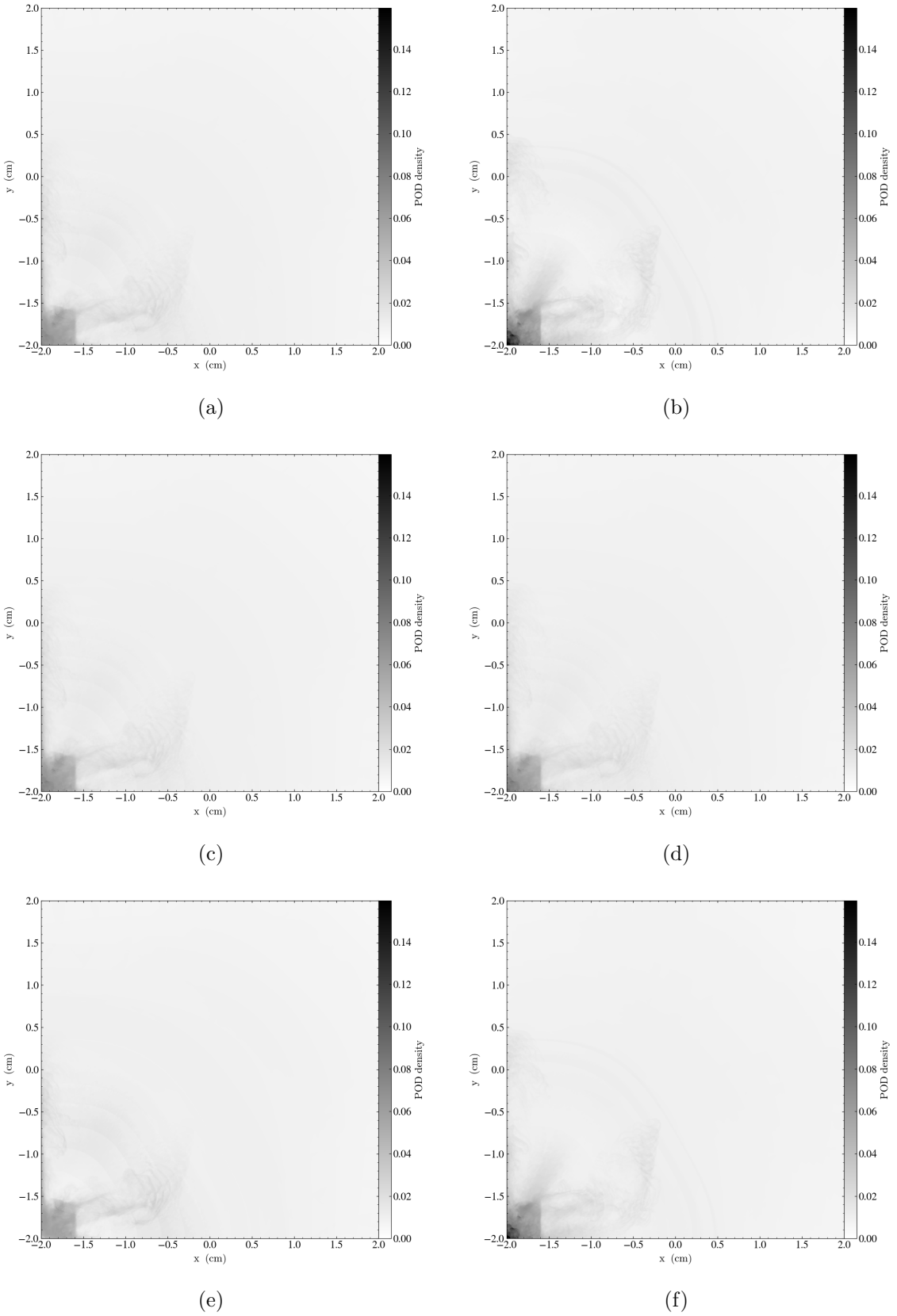

Figure 5.36: Total Density field reconstruction using the 5th mode after performing the POD to the simulation data at several times.

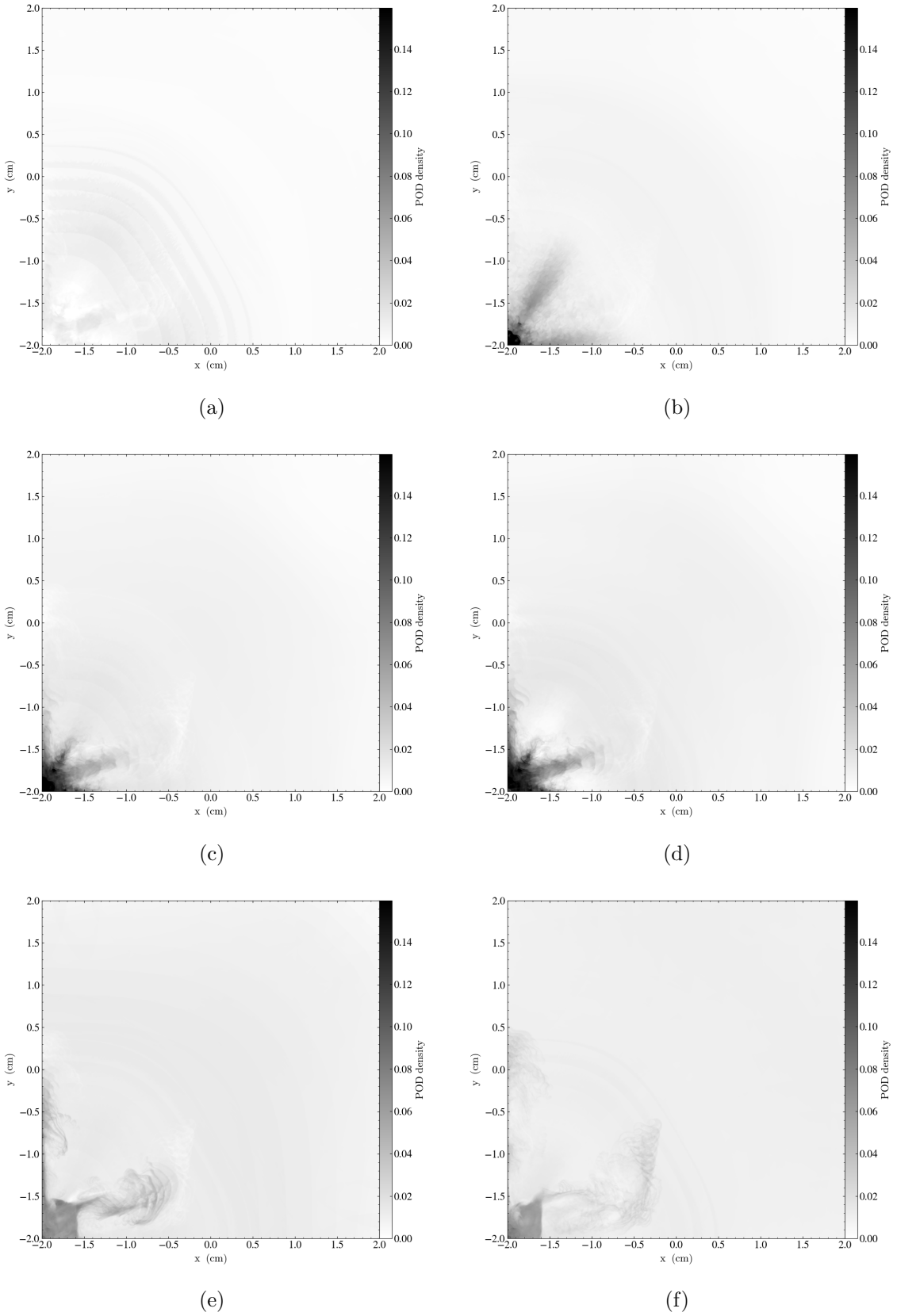

Figure 5.37: Total Density field reconstruction considering the contribution of the first 5 modes after performing the POD to the simulation data at several times.

The purpose of performing the POD is to accurately, at some extent, model the flow behavior in order to compute an estimation of the extent of the mixing layer at late times i.e. after reshock. The POD performs poorly at early times as it can be seen by comparing figures 5.31(a) and 5.32(a). It is suggested here than before reshock, the mean flow drives the initial mixing and growth rate. Fluctuations start evolving at this stage but are not significant compared to the average flow. The POD is performed considering the fluctuating quantities and they are not very well remarked at early times in the reconstructed POD density field of figure 5.32(a) as in the simulated flow of figure 5.31(a).

As the shock wave converges and vortical structures start to evolve and interact, the POD reconstruction start to deliver some coherent results. Observe from figures 5.31(b) and 5.32(b) the resemblance in the structures captured by the POD compared to the simulated flow; nonetheless, the energy captured for one single mode is not enough to accurately be compared to the simulated flow as can be seen from figures 5.31(b) and 5.32(b).

At reshock, the POD reconstructed density field start to deliver a more accurate representation of the flow structures as observed in figures 5.31(c) and 5.32(c). Moments after reshock, the POD reconstructed field is able to capture the phase inversion process as fluctuations have gained energy from reshocking the interface as shown in figures 5.31(d) and 5.32(d). The complex non-linear wave interaction taking place at the SF_6 target amplifies the intensity of the structures at the target's boundary; thus, the first mode of the POD captures this strong interactions but does not capture the mixing layer very well as it diplays a very weak density field in figure 5.32(d) compared to figure 5.31(d).

At late times as depicted in figures 5.31(e) and 5.32(e), the density at the vicinity of the convergence center is still well captured by the first POD mode and the mixing layer structures are more remarked but still weakly captured. At a very late time as shown in figures 5.31(f) and 5.32(f), a similar behavior is portrayed by the first POD mode. At this instance, the POD captured better the outer mixing layer but still is not very well conspicuous as compared with the original density field depicted in figure 5.31(f).

Hence, the first POD mode captures most of the energy deposited by the shock-interface interactions but it is still not sufficient for a proper depiction of the whole phenomena. Nevertheless, a POD analysis just at reshock and afterwards shall deliver a better depiction of the flow as the fluctuations will have a more remarked effect of the total flow rather than if POD is performed as shown in this analysis.

Observe now from figure 5.33 the density field reconstructed using the second POD mode. Initially, this mode does not capture large energetic flow as mode 1 captures high energy flow at the convergence center before reshock (see figures 5.32(a) and 5.33(a)). Thus initially before reshock, mode 1 handles better the wave passage. In contrast, at shock reflection at the center of the target, mode 2 becomes important as it is capturing more energy at this location as seen in figure 5.33(b) compared to figure 5.32(b); nonetheless, mode 1 is still performing better for capturing the weak wave time passage. At reshock snapshot in figure 5.33(c) for mode 2 reconstruction, the density field is stronger as compared with mode 1 for the similar snapshot figure 5.32(c). Thus, at reshock mode 2 delivers a better depiction of the structures of the mixing layer as it is observed from

figure 5.33(c). A few moments after reshock, mode 1 retakes its dominant role as the most energy-containing mode (see figure 5.32(d)) but mode 2 remarks better the structures of the mixing layer as depicted in figure 5.33(d). Mode 2 then dominant in terms of carrying mixing information than mode 1 just after reshock. However, as shown in the rest of the original and POD-reconstructed snapshots, mode 1 overtakes its dominant role once again as the waves-mixing layer interaction ceases (see figures 5.32(e)-5.32(f) and 5.33(e)-5.33(f)). It is suggested then that mode 2 carries information of strong shocks at the vicinity of the convergence center; after such instant, mode 1 reconstructs the overall flow more properly. Mode 2 is then non-negligible for a complete qualitative flow depiction using the POD.

After shock bifurcation but before shock auto-reflection, mode 3 initially (see figure 5.34(a)) does not properly portrays the initial RM instability evolving as in figure 5.31(a). At shock self-reflection stage, mode 3 from figure 5.34(b) portrays better the mixing layer in terms of density than the previous modes 1 and 2 depicted in figures 5.32(b) and 5.33(b) respectively. Mode 2 still performs better than modes 1 and 3 to capture the strong divergent shock wave originated at the convergence center. At reshock time, mode 3 portrays a stronger density field representing the mixing layer but also possesses unphysical structures that are meant to appear in the flow afterwards at late times as it can be seen from figure 5.34(c) in which the future mixing layer appears weakly. A few snapshots after reshock has taken place, mode 3 is still strong in capturing the target density fluctuations as well as the mixing layer but similarly as before, it still presents this future mixing layer, as seen in figure 5.34(d), that mode 1 in fig-

ure 5.32(d) does not present and mode 2 weakly portrays in figure 5.33(d). At a later time, mode 3 captures more fluctuations at the target fluid and a new wave structure near the convergence center as shown in figure 5.34(e). Similarly as mode 2 captured properly the first self-reflected divergent shock wave, mode 3 captures a second divergent shock wave structure copared to mode 1 in 5.32(e) and mode 2 in figure 5.33(e). At a very late time, after all the complex wave interactions have ceased, mode 3 weakly captures the mixing layer but once more mode 1 gains strength at late times; nonetheless, mode 3 is also considered as it captures properly complex post-reshock wave effects.

Mode 4 reconstruction shown in figure 5.35 follows the same sequence as previously outlined. Initially, mode 4 performs poorly as it does not capture any RM instability at all as observed in figure 5.35(a). At shock self-reflection at the center, mode 4 is still not capturing important present features (see figure 5.35(b)). Contrary than mode 3, mode 4 at reshock reproduces a weaker density field as shown in figure 5.35(c). Similar effect happens at a later snapshot in figure 5.35(d). Nonetheless, at the vicinity of the convergence center mode 4 portrays a stronger density field compared to modes 1 and 2 (refer to figures 5.32(d) and 5.33(d)). At a later time, mode 4 weakens except at the convergence center where a strong shock structure is observed in figure 5.35(e). Thus, at a very late time, the evolution of that outwardly-evolving wave structure is better remarked by mode 4 as depicted in 5.35(f). The mixing layer on the other hand is better portrayed by mode 1 as seen in figure 5.32(f).

Consider now mode 5 as depicted in figure 5.36. Concerning initial flow description. this mode is not performing well at all for initial flow fluctuations.

Surprisingly, mode 5 is the best mode thus far for reproducing the first strong shock wave originated by the self-reflection of the convergent shock as it is seen in figure 5.36(b). The reproduction of the density field after the previous snapshot is weak and does not contribute largely to the overall density field. Nevertheless, the strong late-time wave structures captured properly by mode 4 shown in figure 5.35(f) is better remarked by mode 5 as demonstrated in figure 5.36(f) at the cost of a poor reproduction of the mixing layer fluctuations. Hence, mode 5 accentuates strong late-time waves. The addition of more modes is not considered as with 5 modes the analysis is performed over a range of energy of two order of magnitudes as can be observed from figure 5.30. Noticed that to properly reproduce another energy scale of less magnitude, a high quantity of modes are necessary; hence, augmenting the complexity of the correlation tensor in the POD computations.

The overall contribution to the density field of the first 5 modes, previously-analyzed in an isolated manner, is shown in figure 5.37. Observe the close similarities of the POD reconstruction using five modes with respect to the simulation data shown in figure 5.31. Therefore, it is suggested here that reproducing two dominant energy order of magnitudes portrays the flow in a proper way in order to model the mixing layer width and growth rate at reshock. The POD is also suggested to performed more accurately after reshock where high fluctuations are present and more coherent structures interactions occur.

6. Final Remarks

6.1 Conclusions

This work displays ILES simulations of a cylindrical convergent Chisnell-type shock wave propagating in an air medium acting on a azimuthally perturbed SF_6 target immersed in the main medium corresponding to an Atwood number of $A_t = 0.67$. The effects of wavenumber and amplitude of the perturbed initial wave separately to fully characterize interaction between modes is analyzed. It is suggested that low wavenumbers render a wider mixing layer at late times. Moreover, it is found that a low wavenumber before the reshock, the interface amplitude accelerates at a different rate than the higher wavenumber cases. At late times, for constant low-amplitude and varying wavenumber, the low frequency case once more contrasts with the other higher-frequency cases in terms of acceleration again. Hence, at initial shock-interface interaction, the high-wavenumber mode experiences RMI more noticeable but at reshock the low-wavenumber mode is amplified and RMI growth is observed for this mode at late times while a mixing enhancement is mostly observed at reshock and late times related to the high-wavenumber modes in multimode perturbations. Thus, it is suggested that the initial conditions of the induced-spatial perturbation may not be forgotten as previous works have reported. Furthermore, more diffuse interfaces are obtained by high-wavenumbers or short-wavelengths initial perturbations. At such perturbations, it is found that the mass fraction at the mixing layer fluctuates far from the mean of 0.5.

Next, we maintain the wavenumber constant with the purpose of survey on the effects of amplitude variations at the initial perturbation. As expected, we found that initially an amplitude increase widens the mixing layer. Moments after reshock however, we encounter that interaction between scales occur earlier for high-frequency cases. It is reported that such early energy dissipation between scales is the result of secondary shear instabilities being formed promptly for high interface amplitudes. As a consequence, at late time a wider mixing layer is expected for the low amplitude case. In addition, an important finding is that for a high-amplitude initial perturbation, the transmitted shock become a stable polygonal shock wave. Such finding might be useful as a new method for generating polygonal shock waves.

A ROM analysis using the POD technique is performed in the two-dimensional data. The inner product used is non-dimensional in order to be able to sum all the quantities comprehending the state vector. The POD is performed in the fluctuating quantities extracted by a Reynolds decomposition and Favre averaging. Before reshock, the mean flow appear to dominate but it does not capture accurately the energy at this stage. At late times, after reshock, the POD performs well and mode 1 solely can reproduce the density fluctuations driving the interface growth accurately. Five modes are chosen for the final reconstruction in order to capture different structures of the flow. The main observation is that the POD is suitable after reshock which is the stage to model the growth of the interface.

The main observation extracted from this work is that wavelength effects are more interesting than amplitude changes in the wave-like density interface.

6.2 Future Work

A wide variety of 2-dimensional cases were analyzed; nevertheless, more insight into 3D simulations is necessary in order increase the order of accuracy of the interface development. Fractal analysis is also a direction that might be explored for mixing characterization. Experimental realizations are strongly encouraged for future work releases in order to confirm the findings suggested in the present disquisition.

Although the POD reconstructs the flow well after reshock, different ROM techniques such as Dynamical Mode Decomposition or variations of POD such as spectral POD might be implemented for evaluating the best technique to reconstruct the flow. A Galerkin projection of the full governing equations including the mass fraction diffusion equation is necessary for a later interface growth model based on ROM.

REFERENCES

Aglitskiy, Y., Velikovich, A. L., Karasik, M., Metzler, N., Zalesak, S. T., Schmitt, A. J., ... Obenschain, S. P. (2010). Basic hydrodynamics of richtmyer–meshkov-type growth and oscillations in the inertial confinement fusion-relevant conditions. *Philosophical Transactions of the Royal Society of London A: Mathematical, Physical and Engineering Sciences*, *368*(1916), 1739–1768. Retrieved from http://rsta.royalsocietypublishing.org/content/368/1916/1739 doi: 10.1098/rsta.2009.0131

Amendt, P. (2006, 4). Bell-plesset effects for an accelerating interface with contiguous density gradients. *Physics of Plasmas*, *13*(4). doi: 10.1063/1.2174718

Amendt, P., Colvin, J. D., Ramshaw, J. D., Robey, H. F., & Landen, O. L. (2003). Modified bellplesset effect with compressibility: Application to double-shell ignition target designs. *Physics of Plasmas*, *10*(3), 820-829. Retrieved from https://doi.org/10.1063/1.1543926 doi: 10.1063/1.1543926

Anderson, J. (1982). *Modern compressible flow, with historical perspective*. McGraw-Hill.

Atzeni, S., & Meyer-Ter-Vehn, J. (2009). *The Physics of Inertial Fusion: Beam-Plasma Interaction, Hydrodynamics, Hot Dense Matter*. Oxford Science.

Bakhsh, A., Gao, S., Samtaney, R., & Wheatley, V. (2016). Linear simulations of the cylindrical richtmyer-meshkov instability in magnetohydrodynamics. *Physics of Fluids (1994-present)*, *28*(3), 034106.

Balasubramanian, S., Orlicz, G. C., & Prestridge, K. P. (2013). Experimental study of initial condition dependence on turbulent mixing in shock-accelerated richtmyermeshkov fluid layers. *Journal of Turbulence*, *14*(3), 170-196. Retrieved from http://dx.doi.org/10.1080/14685248.2013.792932 doi: 10.1080/14685248.2013.792932

Balasubramanian, S., Orlicz, G. C., Prestridge, K. P., & Balakumar, B. J. (2012). Experimental study of initial condition dependence on richtmyer-meshkov instability in the presence of reshock. *Physics of Fluids*, *24*(3), 034103. Retrieved from http://dx.doi.org/10.1063/1.3693152 doi: 10.1063/1.3693152

Bell, I., G. (1951). *Taylor instability on cylinders and spheres in small amplitude approximation* (Tech. Rep. No. LA-1324). Los Alamos Scientific Laboratory.

Braams, C. M., & Stott, P. E. (2002, aug). Nuclear fusion: half a century of magnetic confinement research. *Plasma Physics and Controlled Fusion*, *44*(8), 1767–1767. doi: 10.1088/0741-3335/44/8/701

Brouillette, M. (2002). The richtmyer-meshkov instability. *Annual Review of Fluid Mechanics*, *34*(1), 445-468. Retrieved from http://dx.doi.org/10.1146/annurev.fluid.34.090101.162238 doi: 10.1146/annurev.fluid.34.090101.162238

Chandrasekhar, S. (1981). *Hydrodynamic and hydromagnetic stability*. Dover Publications.

Cheng, B., Glimm, J., & Sharp, D. H. (2002, Sep). Dynamical evolution of rayleigh-taylor and richtmyer-meshkov mixing fronts. *Phys. Rev. E*, *66*, 036312. Retrieved from https://link.aps.org/doi/10.1103/PhysRevE.66.036312 doi: 10.1103/PhysRevE.66.036312

Chester, W. (1954). Cxlv. the quasi-cylindrical shock tube. *The London, Edinburgh, and Dublin Philosophical Magazine and Journal of Science*, *45*(371), 1293-1301. Retrieved from https://doi.org/10.1080/14786441208561138 doi: 10.1080/14786441208561138

Chisnell, R. F. (1957). The motion of a shock wave in a channel, with applications to cylindrical and spherical shock waves. *Journal of Fluid Mechanics*, *2*(3), 286298. doi: 10.1017/S0022112057000130

Chisnell, R. F. (1998, January). An analytic description of converging shock waves. *Journal of Fluid Mechanics*, *354*, 357-375. Retrieved from http://adsabs.harvard.edu/abs/1998JFM...354..357C (Provided by the SAO/NASA Astrophysics Data System)

Courant, R., & Friedrichs, K. (1999). *Supersonic flow and shock waves*. Springer New York.

De Groot, J. S., Toor, A., Golberg, S. M., & Liberman, M. A. (1997). Growth of the rayleightaylor instability in an imploding z-pinch. *Physics of Plasmas*, *4*(3), 737-747. Retrieved from https://doi.org/10.1063/1.872168 doi: 10.1063/1.872168

Dimonte, G., & Schneider, M. (1996, Oct). Turbulent rayleigh-taylor instability experiments with variable acceleration. *Phys. Rev. E*, *54*, 3740–3743. Retrieved from https://link.aps.org/doi/10.1103/PhysRevE.54.3740 doi: 10.1103/PhysRevE.54.3740

Dimotakis, P. E. (2005). Turbulent mixing. *Annual Review of Fluid Mechanics*, *37*(1), 329-356. Retrieved from https://doi.org/10.1146/annurev.fluid.36.050802.122015 doi: 10.1146/annurev.fluid.36.050802.122015

Ding, J., Si, T., Wang, M., & Luo, X. (2017). A semi-annular cylindrically converging shock tube for richtmyer-meshkov instability studies. In G. Ben-Dor, O. Sadot, & O. Igra (Eds.), *30th international symposium on shock waves 2* (pp. 1079–1083). Cham: Springer International Publishing.

Drazin, P. G. (1992). *Nonlinear systems*. Cambridge University Press. doi: 10.1017/CBO9781139172455

Dutta, S., Glimm, J., Grove, J. W., Sharp, D. H., & Zhang, Y. (2004, May). Spherical richtmyer-meshkov instability for axisymmetric flow. *Math. Comput. Simul.*, *65*(4-5), 417–430. Retrieved from http://dx.doi.org/10.1016/j.matcom.2004.01.020 doi: 10.1016/j.matcom.2004.01.020

Epstein, R. (2004, 10). On the bellplesset effects: The effects of uniform compression and geometrical convergence on the classical rayleightaylor instability. *Physics of Plasmas*, *11*, 5114-5124. doi: 10.1063/1.1790496

Favre, A. (1965). Equations des gaz turbulents compressibles. *Journal de Mecanique*(4), 361–390.

Flash user's guide version 4.5 [Computer software manual]. (2018, December).

Fryxell, B., Olson, K., Ricker, P., Timmes, F. X., Zingale, M., Lamb, D. Q., ... Tufo, H. (2000). Flash: An adaptive mesh hydrodynamics code for modeling astrophysical thermonuclear flashes. *The Astrophysical Journal Supplement Series*, *131*(1), 273. Retrieved from http://stacks.iop.org/0067-0049/131/i=1/a=273

Gatski, T. B., & Bonnet, J.-P. (2013). *Compressibility, turbulence and high speed flow (second edition)* (Second Edition ed.). Oxford: Academic Press. Retrieved from http://www.sciencedirect.com/science/article/pii/B9780123970275000046 doi: https://doi.org/10.1016/B978-0-12-397027-5.00004-6

Godunov, S. (1959). A difference method for numerical calculation of discontinuous solutions of the equations of hydrodynamics. *Mat. Sbornik*, *47*(3), 271–306. Retrieved from http://mi.mathnet.ru/eng/msb4873

Grinstein, F. F., Gowardhan, A. A., & Wachtor, A. J. (2011). Simulations of richtmyermeshkov instabilities in planar shock-tube experiments. *Physics of Fluids*, *23*(3). Retrieved from http://scitation.aip.org/content/aip/journal/pof2/23/3/10.1063/1.3555635 doi: http://dx.doi.org/10.1063/1.3555635

Guderley, G. v. (1942). Starke kugelige und zylindrische verdichtungsstösse in der nähe des kugelmittelpunktes bzw. der zylinderachse. *Luftfahrtforschung*, *19*(9), 302–312.

Hecht, J., Ofer, D., Alon, U., Shvarts, D., Orszag, S., Shvarts, D., & McCrory, R. (1995). Three-dimensional simulations and analysis of the nonlinear stage of the rayleigh-taylor instability. *Laser and Particle Beams*, *13*(3), 423440. doi: 10.1017/S026303460000954X

Hosseini, S. H. R., & Takayama, K. (2005). Experimental study of richtmyermeshkov instability induced by cylindrical shock waves. *Physics of Fluids*, *17*(8), 084101. Retrieved from https://doi.org/10.1063/1.1964916 doi: 10.1063/1.1964916

Hsing, W. W., Barnes, C. W., Beck, J. B., Hoffman, N. M., Galmiche, D., Richard, A., ... Thomas, B. (1997). Rayleightaylor instability evolution in ablatively driven cylindrical implosions. *Physics of Plasmas*, *4*(5), 1832-1840. Retrieved from https://doi.org/10.1063/1.872326 doi: 10.1063/1.872326

Infeld, E. (2000, aug). Fusion: A Voyage through the Plasma Universe. *Journal of Plasma Physics*, *64*, 201–203. Retrieved from http://adsabs.harvard.edu/abs/2000JPlPh..64..201I (Provided by the SAO/NASA Astrophysics Data System) doi: 10.1017/S0022377800228523

Jacobs, J. W., & Sheeley, J. M. (1996). Experimental study of incompressible richtmyer-meshkov instability. *Physics of Fluids*, *8*(2), 405-415. Retrieved from http://dx.doi.org/10.1063/1.868794 doi: 10.1063/1.868794

Joggerst, C., Nelson, A., Woodward, P., Lovekin, C., Masser, T., Fryer, C. L., ... Rockefeller, G. (2014). Cross-code comparisons of mixing during the implosion of dense cylindrical and spherical shells. *Journal of Computational Physics*, *275*, 154 - 173. Retrieved from http://www.sciencedirect.com/science/article/pii/S0021999114004446 doi: http://dx.doi.org/10.1016/j.jcp.2014.06.037

Jourdan, G., & Houas, L. (2005, November). High-Amplitude Single-Mode Perturbation Evolution at the Richtmyer-Meshkov Instability. *Physical Review Letters*, *95*(20), 204502. Retrieved from http://adsabs.harvard.edu/abs/2005PhRvL..95t4502J (Provided by the SAO/NASA Astrophysics Data System) doi: 10.1103/PhysRevLett.95.204502

Juchun, D., Si, T., Yang, J., Lu, X., Zhai, Z., & Luo, X. (2017, 07). Measurement of a richtmyer-meshkov instability at an air- sf6 interface in a semiannular shock tube. *Physical Review Letters*, *119*.

Lei, F., Juchun, D., Si, T., Zhai, Z., & Luo, X. (2017, 09). Experimental study on a sinusoidal air/sf interface accelerated by a cylindrically converging shock. *Journal of Fluid Mechanics*, *826*, 819-829.

Liang, Y., Ding, J., Zhai, Z., Si, T., & Luo, X. (2017). Interaction of cylindrically converging diffracted shock with uniform interface. *Physics of Fluids*, *29*(8), 086101. Retrieved from https://doi.org/10.1063/1.4997071 doi: 10.1063/1.4997071

Liu, X.-D., Osher, S., & Chan, T. (1994). Weighted essentially non-oscillatory schemes. *Journal of Computational Physics*, *115*(1), 200–212. Retrieved from www.sciencedirect.com/science/article/pii/S0021999184711879 doi: http://dx.doi.org/10.1006/jcph.1994.1187

Liu, Y. (2008). Richtmyer-meshkov instability and gas-particle interaction of contoured shock-tube flows: a numerical study. *World Academy of Science, Engineering and Technology*, *22*, 365–369.

Livescu, D., & Ristorcelli, R. (2007, 11). Buoyancy-driven variable-density turbulence. *Journal of Fluid Mechanics*, *591*, 43 - 71. doi: 10.1017/S0022112007008270

Lombardini, M., I. Pullin, D., & Meiron, D. (2014a, 06). Turbulent mixing driven by spherical implosions. part1. flow description and mixing-layer growth. *Journal of Fluid Mechanics*, *748*, 85-112.

Lombardini, M., I. Pullin, D., & Meiron, D. (2014b, 06). Turbulent mixing driven by spherical implosions. part 2. turbulence statistics. *Journal of Fluid Mechanics*, *748*, 113-142.

Lombardini, M., & Pullin, D. I. (2009, November). Small-amplitude perturbations in the three-dimensional cylindrical Richtmyer-Meshkov instability. *Physics of Fluids*, *21*(11), 114103-114103. Retrieved from http://adsabs.harvard.edu/abs/2009PhFl...21k4103L (Provided by the SAO/NASA Astrophysics Data System) doi: 10.1063/1.3258668

Lombardini, M., & Pullin, D. I. (2009). Startup process in the richtmyermeshkov instability. *Physics of Fluids*, *21*(4), 044104. Retrieved from https://doi.org/10.1063/1.3091943 doi: 10.1063/1.3091943

Lumley, J. L. (1967). The Structure of Inhomogeneous Turbulent Flows. In A. M. Yaglom & V. I. Tatarski (Eds.), *Atmospheric turbulence and radio propagation* (pp. 166–178). Moscow: Nauka.

Luo, X., Ding, J., Wang, M., Zhai, Z., & Si, T. (2015). A semi-annular shock tube for studying cylindrically converging richtmyer-meshkov instability. *Physics of Fluids*, *27*(9), 091702. Retrieved from https://aip.scitation.org/doi/abs/10.1063/1.4931929 doi: 10.1063/1.4931929

Marocchino, A., Atzeni, S., & Schiavi, A. (2010). Numerical study of the ablative richtmyermeshkov instability of laser-irradiated deuterium and deuterium-tritium targets. *Physics of Plasmas*, *17*(11), 112703. Retrieved from https://doi.org/10.1063/1.3505112 doi: 10.1063/1.3505112

Meshkov, E. E. (1969). Instability of the interface of two gases accelerated by a shock wave. *Fluid Dynamics*, *4*(5), 101–104. Retrieved from http://dx.doi.org/10.1007/BF01015969 doi: 10.1007/BF01015969

Mikaelian, K. O. (1990, Sep). Rayleigh-taylor and richtmyer-meshkov instabilities and mixing in stratified spherical shells. *Phys. Rev. A*, *42*, 3400–3420. Retrieved from https://link.aps.org/doi/10.1103/PhysRevA.42.3400 doi: 10.1103/PhysRevA.42.3400

Mikaelian, K. O. (2005). Rayleigh-taylor and richtmyer-meshkov instabilities and mixing in stratified cylindrical shells. *Physics of Fluids*, *17*(9), 094105. Retrieved from https://doi.org/10.1063/1.2046712 doi: 10.1063/1.2046712

Morton, G. (1966). A computer oriented geodetic data base and a new technique. In *in file sequencing. tech. rep., ibm ltd.*

Mostert, W., Wheatley, V., Samtaney, R., & Pullin, D. I. (2015). Effects of magnetic fields on magnetohydrodynamic cylindrical and spherical richtmyer-meshkov instability. *Physics of Fluids*, *27*(10), 104102. Retrieved from https://doi.org/10.1063/1.4932110 doi: 10.1063/1.4932110

National Research Council. (2013). *An assessment of the prospects for inertial fusion energy.* Washington, DC: The National Academies Press. Retrieved from https://www.nap.edu/catalog/18289/an-assessment-of-the-prospects-for-inertial-fusion-energy doi: 10.17226/18289

Niederhaus, C. E., & Jacobs, J. W. (2004). An experimental study of the richtmyer-meshkov instability in microgravity. *Annals of the New York Academy of Sciences*, *1027*(1), 403–413. Retrieved from http://dx.doi.org/10.1196/annals.1324.033 doi: 10.1196/annals.1324.033

Ockendon, H., & Ockendon, J. (2016). *Waves and compressible flow.* Springer New York.

Olson, B. J., & Greenough, J. A. (2014). Comparison of two- and three-dimensional simulations of miscible richtmyer-meshkov instability with multimode initial conditions. *Physics of Fluids*, *26*(10), 101702. Retrieved from http://dx.doi.org/10.1063/1.4898157 doi: 10.1063/1.4898157

Pfalzner, S. (2006, mar). An Introduction to Inertial Confinement Fusion. *An Introduction to Inertial Confinement Fusion.*, *19*. Retrieved from http://adsabs.harvard.edu/abs/2006SPP....19.....P (Provided by the SAO/NASA Astrophysics Data System) doi: 10.1201/9781420011845

Plesset, M. S. (1954). On the stability of fluid flows with spherical symmetry. *Journal of Applied Physics*, *25*(1), 96-98. Retrieved from https://doi.org/10.1063/1.1721529 doi: 10.1063/1.1721529

Pletcher, R., Tannehill, J., & Anderson, D. (2012). *Computational fluid mechanics and heat transfer, third edition.* Taylor & Francis.

Poggi, F., Thorembey, M. H., & Rodriguez, G. (1998). Velocity measurements in turbulent gaseous mixtures induced by richtmyer-meshkov instability. *Physics of Fluids*, *10*(11), 2698-2700. Retrieved from http://scitation.aip.org/content/aip/journal/pof2/10/11/10.1063/1.869794 doi: http://dx.doi.org/10.1063/1.869794

Prasad, J. K., Rasheed, A., Kumar, S., & Sturtevant, B. (2000). The late-time development of the richtmyermeshkov instability. *Physics of Fluids*, *12*(8), 2108-2115. Retrieved from https://doi.org/10.1063/1.870456 doi: 10.1063/1.870456

Ramsey, S. D., Kamm, J. R., & Bolstad, J. H. (2012, February). The Guderley problem revisited. *International Journal of Computational Fluid Dynamics*, *26*, 79-99. doi: 10.1080/10618562.2011.647768

Rayleigh, L. (1882). Investigation of the character of the equilibrium of an incompressible heavy fluid of variable density. *Proceedings of the London Mathematical Society*, *s1-14*(1), 170-177. Retrieved from http://plms.oxfordjournals.org/content/s1-14/1/170.short doi: 10.1112/plms/s1-14.1.170

Remington, B. A., Haan, S. W., Glendinning, S. G., Kilkenny, J. D., Munro, D. H., & Wallace, R. J. (1992). Large growth, planar rayleightaylor experiments on nova. *Physics of Fluids B: Plasma Physics*, *4*(4), 967-978. Retrieved from https://doi.org/10.1063/1.860113 doi: 10.1063/1.860113

Richtmyer, R. D. (1960). Taylor instability in shock acceleration of compressible fluids. *Communications on Pure and Applied Mathematics*, *13*(2), 297–319. Retrieved from http://dx.doi.org/10.1002/cpa.3160130207 doi: 10.1002/cpa.3160130207

Rikanati, A., Oron, D., Sadot, O., & Shvarts, D. (2003, Feb). High initial amplitude and high mach number effects on the evolution of the single-mode richtmyer-meshkov instability. *Phys. Rev. E*, *67*, 026307. Retrieved from https://link.aps.org/doi/10.1103/PhysRevE.67.026307 doi: 10.1103/PhysRevE.67.026307

Rowley, C. W., Colonius, T., & Murray, R. M. (2004). Model reduction for compressible flows using pod and galerkin projection. *Physica D: Nonlinear Phenomena*, *189*(1), 115 - 129. Retrieved from http://www.sciencedirect.com/science/article/pii/S0167278903003841 doi: https://doi.org/10.1016/j.physd.2003.03.001

Samtaney, R. (2003). Suppression of the richtmyer-meshkov instability in the presence of a magnetic field. *Physics of Fluids*, *15*(8), L53-L56. Retrieved from http://scitation.aip.org/content/aip/journal/pof2/15/8/10.1063/1.1591188 doi: http://dx.doi.org/10.1063/1.1591188

Sano, T., Nishihara, K., Matsuoka, C., & Inoue, T. (2012, oct). Magnetic Field Amplification Associated with the Richtmyer-Meshkov Instability. , *758*, 126. Retrieved from http://adsabs.harvard.edu/abs/2012ApJ...758..126S (Provided by the SAO/NASA Astrophysics Data System) doi: 10.1088/0004-637X/758/2/126

Schilling, O., & Latini, M. (2010). High-order weno simulations of three-dimensional reshocked richtmyermeshkov instability to late times: dynamics, dependence on initial conditions, and comparisons to experimental data. *Acta Mathematica Scientia*, *30*(2), 595–620. Retrieved from http://www.sciencedirect.com/science/article/pii/S0252960210600641 doi: http://dx.doi.org/10.1016/S0252-9602(10)60064-1

Schwendeman, D. W., & Whitham, G. B. (1987). On converging shock waves. *Proceedings of the Royal Society of London. A. Mathematical and Physical Sciences*, *413*(1845), 297-311. Retrieved from https://royalsocietypublishing.org/doi/abs/10.1098/rspa.1987.0116 doi: 10.1098/rspa.1987.0116

Seadawy, A. R., & El-Rashidy, K. (2016, Jul 07). Nonlinear rayleigh–taylor instability of the cylindrical fluid flow with mass and heat transfer. *Pramana*, *87*(2), 20. Retrieved from https://doi.org/10.1007/s12043-016-1222-x doi: 10.1007/s12043-016-1222-x

Shapiro, A. (1953). *The dynamics and thermodynamics of compressible fluid flow* (No. v. 1). Ronald Press Co.

Shapiro, A. (1954). *The dynamics and thermodynamics of compressible fluid flow* (No. v. 2). Ronald Press Co.

Shi, H., Zhang, G., Du, K., & Jia, H. (2009). Experimental study on the mechanism of the richtmyer-meshkov instability at a gas-liquid interface. *Journal of Hydrodynamics*, *21*(3), 423 - 428. Retrieved from http://www.sciencedirect.com/science/article/pii/S1001605808601663 doi: http://dx.doi.org/10.1016/S1001-6058(08)60166-3

Sinars, D. B., Slutz, S. A., Herrmann, M. C., McBride, R. D., Cuneo, M. E., Jennings, C. A., ... Porter, J. L. (2011). Measurements of magneto-rayleightaylor instability growth during the implosion of initially solid metal liners. *Physics of Plasmas*, *18*(5), 056301. Retrieved from https://doi.org/10.1063/1.3560911 doi: 10.1063/1.3560911

Sinars, D. B., Slutz, S. A., Herrmann, M. C., McBride, R. D., Cuneo, M. E., Peterson, K. J., ... Porter, J. L. (2010, Oct). Measurements of magneto-rayleigh-taylor instability growth during the implosion of initially solid al tubes driven by the 20-ma, 100-ns z facility. *Phys. Rev. Lett.*, *105*, 185001. Retrieved from https://link.aps.org/doi/10.1103/PhysRevLett.105.185001 doi: 10.1103/PhysRevLett.105.185001

Sirovich, L. (1987a). Turbulence and the dynamics of coherent structures part i: Coherent structures. *Quarterly of Applied Mathematics*, *45*(3), 561-571. Retrieved from http://www.jstor.org/stable/43637457

Sirovich, L. (1987b). Turbulence and the dynamics of coherent structures part ii: Symmetries and transformations. *Quarterly of Applied Mathematics*, *45*(3), 573-582. Retrieved from http://www.jstor.org/stable/43637458

Stalsberg-Zarling, K., & Gore, R. (2011). *The bhr2 turbulence model: Incompressible isotropic decay, rayleigh-taylor, kelvin-helmholtz and homogeneous variable density turbulence* (Tech. Rep. No. 04773). Los Alamos National Laboratory.

Stone, J. M., & Gardiner, T. (2007). Nonlinear evolution of the magnetohydrodynamic rayleigh-taylor instability. *Physics of Fluids*, *19*(9), 094104. Retrieved from https://doi.org/10.1063/1.2767666 doi: 10.1063/1.2767666

Takayama, K., Kleine, H., & Grönig, H. (1987, Sep 01). An experimental investigation of the stability of converging cylindrical shock waves in air. *Experiments in Fluids*, *5*(5), 315–322. Retrieved from https://doi.org/10.1007/BF00277710 doi: 10.1007/BF00277710

Taylor, G. (1950). The instability of liquid surfaces when accelerated in a direction perpendicular to their planes. *Proceedings of the Royal Society of London A: Mathematical, Physical and Engineering Sciences*, *201*(1065), 192–196. Retrieved from http://rspa.royalsocietypublishing.org/content/201/1065/192 doi: 10.1098/rspa.1950.0052

Thornber, B., Drikakis, D., Youngs, D. L., & Williams, R. J. (2010). The influence of initial conditions on turbulent mixing due to richtmyermeshkov instability. *Journal of Fluid Mechanics*, *654*, 99139. doi: 10.1017/S0022112010000492

Toro, E. F., Spruce, M., & Speares, W. (1994, Jul 01). Restoration of the contact surface in the hll-riemann solver. *Shock Waves*, *4*(1), 25–34. Retrieved from https://doi.org/10.1007/BF01414629 doi: 10.1007/BF01414629

Tubbs, D. L., Barnes, C. W., Beck, J. B., Hoffman, N. M., Oertel, J. A., Watt, R. G., ... Knauer, J. (1999). Cylindrical implosion experiments using laser direct drive. *Physics of Plasmas*, *6*(5), 2095-2104. Retrieved from https://doi.org/10.1063/1.873462 doi: 10.1063/1.873462

Ukai, S., Balakrishnan, K., & Menon, S. (2011). Growth rate predictions of single- and multi-mode richtmyer–meshkov instability with reshock. *Shock Waves*, *21*(6), 533. Retrieved from http://dx.doi.org/10.1007/s00193-011-0332-0 doi: 10.1007/s00193-011-0332-0

Vandenboomgaerde, M., Gauthier, S., & Mgler, C. (2002). Nonlinear regime of a multimode richtmyermeshkov instability: A simplified perturbation theory. *Physics of Fluids*, *14*(3), 1111-1122. Retrieved from http://dx.doi.org/10.1063/1.1447914 doi: 10.1063/1.1447914

van Leer, B. (1979). Towards the ultimate conservative difference scheme. v. a second-order sequel to godunov's method. *Journal of Computational Physics*, *32*(1), 101 - 136. Retrieved from http://www.sciencedirect.com/science/article/pii/0021999179901451 doi: https://doi.org/10.1016/0021-9991(79)90145-1

Velikovich, A. L., & Schmit, P. F. (2015). Bell-plesset effects in rayleigh-taylor instability of finite-thickness spherical and cylindrical shells. *Physics of Plasmas*, *22*(12), 122711. Retrieved from https://doi.org/10.1063/1.4938272 doi: 10.1063/1.4938272

Vetter, M., & Sturtevant, B. (1995). Experiments on the richtmyer-meshkov instability of an air/sf6 interface. *Shock Waves*, *4*(5), 247–252. Retrieved from http://dx.doi.org/10.1007/BF01416035 doi: 10.1007/BF01416035

Wang, L. F., Wu, J. F., Ye, W. H., Zhang, W. Y., & He, X. T. (2013). Weakly nonlinear incompressible rayleigh-taylor instability growth at cylindrically convergent interfaces. *Physics of Plasmas*, *20*(4), 042708. Retrieved from https://doi.org/10.1063/1.4803067 doi: 10.1063/1.4803067

Whitham, G. B. (1958). On the propagation of shock waves through regions of non-uniform area or flow. *Journal of Fluid Mechanics*, *4*, 337-360.

Whitham, G. B. (1974). *Linear and nonlinear waves*. Wiley. Retrieved from https://books.google.com/books?id=f8oRAQAAIAAJ

Wurden, G. A., Hsu, S. C., Intrator, T. P., Grabowski, T. C., Degnan, J. H., Domonkos, M., ... others (2016). Magneto-inertial fusion. *Journal of Fusion Energy*, *35*(1), 69–77.

Yang, Q., & Fu, S. (2008, May). Analysis of flow structures in supersonic plane mixing layers using the POD method. *Science in China: Physics, Mechanics and Astronomy*, *51*, 541-558. doi: 10.1007/s11433-008-0029-2

Youngs, D. (1991). Threedimensional numerical simulation of turbulent mixing by rayleightaylor instability. *Physics of Fluids A: Fluid Dynamics*, *3*(5), 1312–1320. Retrieved from https://doi.org/10.1063/1.858059 doi: 10.1063/1.858059

Youngs, D. (1994). Numerical simulation of mixing by rayleightaylor and richtmyermeshkov instabilities. *Laser and Particle Beams*, *12*(4), 725–750. doi: 10.1017/S0263034600008557

Youngs, D. L., & Williams, R. J. R. (2008). Turbulent mixing in spherical implosions. *International Journal for Numerical Methods in Fluids*, *56*(8), 1597-1603. Retrieved from https://onlinelibrary.wiley.com/doi/abs/10.1002/fld.1594 doi: 10.1002/fld.1594

Yu, H., & Livescu, D. (2008). Rayleightaylor instability in cylindrical geometry with compressible fluids. *Physics of Fluids*, *20*(10), 104103. Retrieved from https://doi.org/10.1063/1.2991431 doi: 10.1063/1.2991431

Zel'dovich, Y., & Raizer, Y. (2002). *Physics of shock waves and high-temperature hydrodynamic phenomena*. Dover Publications. Retrieved from https://books.google.com/books?id=zVf27TMNdToC

Zeng, W.-G., Pan, J.-H., Sun, Y.-T., & Ren, Y.-X. (2018). Turbulent mixing and energy transfer of reshocked heavy gas curtain. *Physics of Fluids*, *30*(6), 064106. Retrieved from https://doi.org/10.1063/1.5032275 doi: 10.1063/1.5032275

Zhang, F., Zhai, Z., Si, T., & Luo, X. (2017). Experimental study on the interaction of cylindrical converging shock waves with sinusoidal light-heavy interface. In G. Ben-Dor, O. Sadot, & O. Igra (Eds.), *30th international symposium on shock waves 2* (pp. 1085–1089). Cham: Springer International Publishing.

Zhang, Q., & Graham, M. J. (1998). A numerical study of richtmyer-meshkov instability driven by cylindrical shocks. *Physics of Fluids*, *10*(4), 974-992. Retrieved from http://dx.doi.org/10.1063/1.869624 doi: 10.1063/1.869624

Zhou, Y. (2017a). Rayleightaylor and richtmyermeshkov instability induced flow, turbulence, and mixing. i. *Physics Reports*, *720-722*, 1 - 136. Retrieved from http://www.sciencedirect.com/science/article/pii/S0370157317302028 (Rayleigh-Taylor and Richtmyer-Meshkov instability induced flow, turbulence, and mixing. I) doi: https://doi.org/10.1016/j.physrep.2017.07.005

Zhou, Y. (2017b). Rayleightaylor and richtmyermeshkov instability induced flow, turbulence, and mixing. ii. *Physics Reports*, *723-725*, 1 - 160. Retrieved from http://www.sciencedirect.com/science/article/pii/S0370157317302958 (RayleighTaylor and RichtmyerMeshkov instability induced flow, turbulence, and mixing. II) doi: https://doi.org/10.1016/j.physrep.2017.07.008

Zohuri, B. (2017). *Inertial Confinement Fusion Driven Thermonuclear Energy*. Springer International Publishing. Retrieved from https://doi.org/10.1007/978-3-319-50907-5_3 doi: 10.1007/978-3-319-50907-5_3

A. Post-Processing

As mentioned previously, HDF5 data is a general and well-structured tree-like data structure for storing data in a hierarchical way. Several software for reading such data type are available freely and also with commercial licensing. The author chose to use the yt Python API for the present post-processing work as it delivers data treatment interface for reading Flash HDF5 output files and generate the desired plots and after-simulation quantities of interest such as gradients, mixing layer quantification, turbulence statistical analysis among others.

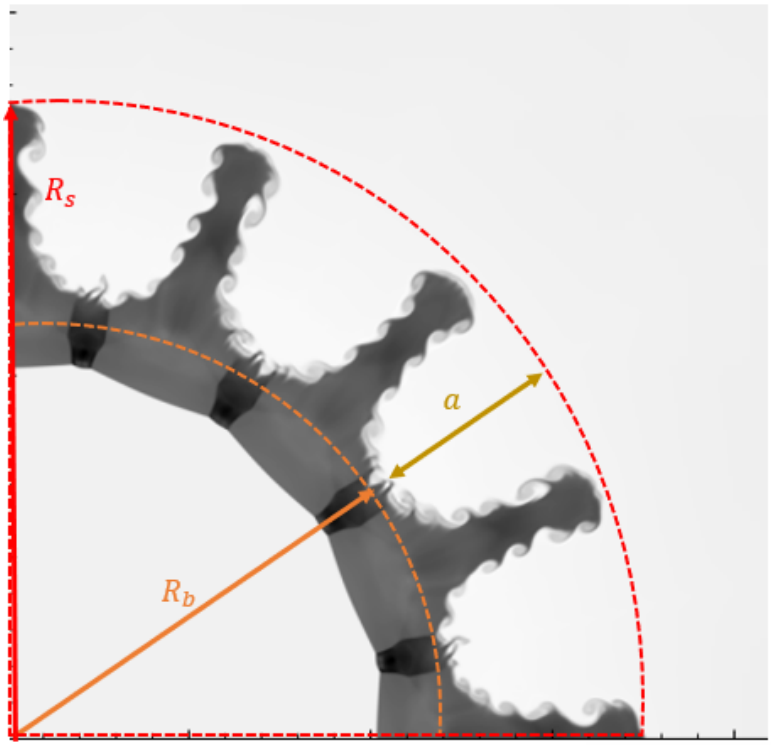

Figure A.1: Mixing layer definition for computations. The mixing layer width is defined for the scope of this document as the difference between the highest radial spike and the lowest radial bubble.

A.1 Mixing Layer Computation

The definition of the mixing layer width throughout this work is the whole measured width in time of the evolution of the mixing layer. That is, the radial location of the bubble penetrating the heaviest fluid is subtracted from the

maximum radial location of the spike penetrating the lightest fluid as depicted in figure A.1. From this definition, two approaches might be considered for the final computation of the interface width: a measurement approach or an statistical approach, both are based on the mass fraction of the fluids.

A.1.1 The "Measurement Method"

This methodology for computing the interface consists on interpolating the mass fraction field values along straight lines originated from the convergence center and varying the lines azimuthally. Consider a domain similar to the one displayed in figure A.1. Then, a line profile is defined with one extreme at the left-most down corner and the other at the right-most down corner. The mass fraction values interpolating such line profile are then extracted and the interface width along that line is saved. Next, a new line profile with one extreme at the left-most down corner and the other at the other at the right-most corner plus an angular increment in the azimuthal direction. A similar interpolation process is performed at this new 1D profile. Then, one of the extremes of the line profile is kept at the left-most corner while increasing the azimuthal angular offset at the other extreme and extracting the interface width in each step. Finally, when the last extreme of the line profile is at the upper left-most corner i.e. angular offset is 90^o, the iterations are stopped and each interface width from each generated profile are compared by extracting the minimum and the maximum of each profile and choosing the maximum spike minus the minimum bubble. This delivers the interface width for one time output. The whole process is repeated for each output until computing the evolution of the interface

width for the complete simulated time. Observed that ergodicity is not assume at any time while performing averaging.

A.1.2 Statistical Method

Although the "measurement method" delivers realistic values, it introduces a noisy interface width. The drawback of this noise is visualized when computing the derivative of that quantity i.e. the growth rate. Thus, a statistical approach is intended to deliver a mixing layer width with less noise by using the average values of the mass fraction. The mixing layer with this method is computed as

$$a = \int_{r_0}^{r_f} \overline{Y_1 \left(1 - Y_1\right)} dr \tag{A.1}$$

For this approach in a similar domain, polar 1D profiles are used instead of the line profiles described previously. Hence, a polar profile starting at an initial radius r_0 measured from the convergence center is generated by interpolating the values of the quantity inside the integral in equation A.1. An average of those values along each polar profile is calculated. The circular profiles are incremented in the radial direction until the whole domain has been covered at radius r_f. Next, a numerical integration presented in equation A.1 is performed using the trapezoidal rule. This process is carried out for each time output in order to obtain the time evolution of the interface.

The main advantage of the measurement method over the statistical approach is the accuracy obtained in computing the interface width as it extracts a more realistic mixing layer evolution. Nonetheless, the noise introduced causes issues in the computations of the growth rate due to the numerical derivation process. On the other hand, the statistical methodology lacks accuracy com-

pared to the measurement method but it delivers a smooth mixing layer width rendering a more doable numerical derivation for computing the growth rate. Furthermore, since the radial profiles are based on the intersection of a sphere centered at the convergence center with the computational domain, it makes more suitable and less expensive numerical-wise to compute the statistical quantity in a three-dimensional domain. Whereas in a 3D domain using the measurement method, slices along the whole domain are necessary due to the line profiles considered; thus, more iterations are introduced rendering the whole computations expensive. Therefore, two-dimensional simulations used the measurement approach while three-dimensional mixing layers are quantified using the statistical approach. In 2D simulations, the noise present due to the method used to measure the mixing zone thickness is minimized using a filter in order to compute the growth rate.

A.2 Mixing

Mixing is quantified using statistical quantities. Both, the density-specific volume correlation and the molecular mixing fraction, are based on averaged quantities. While the b correlation is not an integral quantity in this work, it is useful for characterizing mixing at each time step while the molecular mixing fraction portrays a more wide picture of the mixing evolution in time. Both quantities converged to the same conclusions but the molecular mixing fraction is more smooth.

The density-specific volume correlation algorithm is as follows: First, an initial polar profile near and centered at the convergence center is generated and the mean values of the interpolated density and specific volume are extracted.

The operation from equation 5.2 is performed at the present radial location and these b value is stored in an auxiliary variable. A similar procedure is performed while increasing the radius of the polar intersecting profile. Once all the domain has been radially covered, the auxiliary value and the radial locations of each profile are implemented in a plot routine. This delivers a b profile along radial locations. The process is repeated at each time step and the evolution of mixing can be observed by the plot of b vs. radius at each time output.

Molecular mixing follows the same procedure with the addition of an integration step. Hence, after the profile θ (refer to equation 5.3) along the radius of the domain is extracted, then the numerical integration of equation 5.6 is performed to obtain the integral molecular mixing fraction. Finally, each Θ corresponding to a time step is stored with its time quantity and the plot subroutine is called.

A.3 Shock Tracking Space-Time Diagram

The space time diagram is generated with the same polar profiles incremented radially as described previously. Each radial profiles extracts by interpolation with the domain values of average density or pressure along each profile. All the pressure or density azimuthally-averaged values and the radius are stored in a 2-dimensional array for a later call to a surface plot routine. The final plot result shows all the discontinuities present during all the simulation. The main difference in choosing density over pressure is that density tracks the mixing layer and the waves location while pressure only tracks the latter.

A.4 POD Algorithm

The POD algorithm implements the POD equations in the FLASH-generated data. The process starts by computing time-averaged field of the primal variables composing the state vector. If dealing with a compressible flow, the average must be a Favre average or density-weighted average. Then, a Reynolds decomposition is performed to separate the fluctuating quantities to the total flow quantities. To do it so, new fields are first defined corresponding to the fluctuations of each variable composing the state vector $q\left(\mathbf{x}, t\right)$ and then inside such definitions the mean flow is subtracted to the total flow quantities. Due to a current bug in the yt API, the mean variables are defined as global variables to inherit the real size of each array. Afterwards, each variable that build the state vector is concatenated in one single array to define $\mathbf{q}$ as a function of the fluctuating quantities. The inner product $R = \mathbf{q}, \mathbf{q^T}$ is then computed in order to obtain the auto-correlation tensor R.

The inner product is an user-defined function that allows to define a customized inner product depending on the variables and the normalization. A singular value decomposition (SVD) is performed over the correlation tensor R and the left-singular vectors with the eigenvalues are obtained. The left-singular vectors are delivered as a 2×2 array which columns are the vectors and the eigenvalues in a similar fashion but it is a diagonal matrix with each eigenvalue. The left-singular vectors are called the POD modes. Each POD mode is then normalized by a subroutine to deliver a matrix with the normal POD modes ϕ.

Then, the time coefficients a are computed by a different subroutine by using the POD modes and the flow quantities. Finally, the flow is reconstructed by

using a user-defined number of POD modes and the plots are generated to compared simulation field data to POD reconstructed data. This is a very straight forward approach to perform the POD analysis; nonetheless, a Galerkin projection is necessary for estimating the mixing layer growth without requiring the use of solving numerically the governing equations.

A.5 Repository

The post-processing algorithms described above are found in the author's Github repository

`https://github.com/Erik-Proano/yt_PostProcessing_FLASH.git`

while the POD implementation is found in the Github repository

`https://github.com/Erik-Proano/POD_CompressibleFlashHDF5.git`